KIT

Karlsruhe Institute of Technology

Measurement of the positron fraction in cosmic rays from 0.5 - 350 GeV with the AMS-02 detector on the International Space Station

Zur Erlangung des akademischen Grades eines
DOKTORS DER NATURWISSENSCHAFTEN
von der Fakultät für Physik des Karlsruhe Institut für Technologie

genehmigte

DISSERTATION
von

Dipl. Phys. Melanie Heil
aus Bad Kreuznach

Zusammenfassung

Das Alpha Magnet Spektrometer (AMS-02) ist ein auf der Internationalen Raumstation montierter Teilchendetektor, der dort seit dem 19. Mai 2011 die kosmische Strahlung misst. Dabei werden durch redundanten Messungen der Teilcheneigenschaften mit den fünf Subdetektoren von AMS-02 die Teilchenidentität sowie ihre Energie bestimmt, was eine präzise Messung der Spektren bis hin zu TeV Energien erlaubt. Einer der Hauptaspekte von AMS ist die Suche nach Dunkler Materie. Schwach wechselwirkende, massive Teilchen (WIMPS), welche aktuell die vielversprechendsten Dunkle Materie Kandidaten sind, können sich in unserer Galaxie gegenseitig vernichten, wodurch unter anderem Protonen, Antiprotonen, Elektronen und Positronen erzeugt würden. Letztere eignen sich besonders für die Suche eines solchen Vernichtungssignals, da ihr regulärer kosmischer Teilchenfluss vergleichsweise gering ist.

Aufgrund der Häufigkeit von Protonen in der kosmischen Strahlung ist die Unterscheidungsfähigkeit von Protonen und Positronen durch den Detektor wichtig. Für AMS-02 wird dies durch den TRD sowie das ECAL gewährleistet. Für die in dieser Arbeit durchgeführte Analyse des Positronen Anteils im Summenfluss von Positronen und Elektronen ist die optimale Funktion beider Subdetektoren von Nöten. Im Rahmen dieser Arbeit wurde dabei im Besonderen die Arbeitsweise des TRD studiert. Die Nutzung von fehlenden Signalen im TRD, welche dann auftreten wenn ein Teilchen durch die wenige 100 μm breite Lücke zwischen zwei Proportionalkammern des TRD hindurch fliegt, für die Berechnung dessen zeitabhängigen räumlichen Ausrichtung sowie für dessen Spurrekonstruktion wird vorgestellt.

Aus den AMS-02 Daten der ersten 18 Monate Betrieb auf der ISS wurde der Positronen Anteil in der kosmischen Strahlung mit unvorangegangener Genauigkeit berechnet und der vermessene Energiebereich wurde um mehr als das zweifache auf 0.5 - 350 GeV erweitert. Die in dieser Arbeit durchgeführte Analyse bestätigt die offizielle AMS-02 Analyse durch Nutzung unterschiedlicher Kalibrierungen, rekonstruierter Variablen und einer anderen Vorgehensweise zur Untergrundbestimmung.

Das Ergebnis der Analyse zeigt, dass der Anteil der Positronen im Summenfluss bis zu 7 GeV stetig abnimmt, wie man es aus der Produktion von Positronen in der Wechselwirkung von primären kosmichen Teilchen mit dem interstellaren Gas erwarten würde. Oberhalb von 10 GeV nimmt der Anteil hingegen stetig zu, wobei die Steigung oberhalb 200 GeV im Vergleich zu 20 GeV um eine Grössenordnung abnimmt. Die Zunahme des Positronen Anteils impliziert eine zusätzliche Quelle für hochenergetische Positronen. Diese kann durch ein einfaches Potenzgesetz mit einer Abschneideenergie modelliert werden. Eine Anpassung des Modells an die Daten dieser Analyse oberhalb von 1 GeV liefert eine Abschneideenergie der Quelle von $E_s = 750^{+1024}_{-270}$ GeV mit $\chi^2/ndf = 18.23/29$. Für die Bestimmung des Positronen Anteils oberhalb 350 GeV sind mehr Daten wünschenswert um eine statistisch aussagekräftigere Messung machen zu können. Das bislang erreichte Wissen ist nicht aussreichend um eine endgültige Aussage über die für den Anstieg des Positronen Anteils ver-

antwortliche Quelle zu treffen. Sowohl Pulsare als auch Dunkle Materie Modelle können die Daten beschreiben, da beide viele unbestimmte Parameter haben. Die Änderung der Steigung zu höheren Energien lässt hoffen, dass das Maximum des Positronen Anteils innerhalb des von AMS-02 messbaren Energiebereichs liegt. Analysen der AMS-02 Daten bezüglich des Protonen-, Elektronen- und Heliumflusses sowie des Bor zu Kohlenstoff-Verhältnisses, welche in naher Zukunft veröffentlicht werden sollen, werden bessere Vorhersagen durch Transportmodelle der kosmsichen Strahlung ermöglichen. Dies in Kombination mit erweiterten Messungen des Positonenanteils wird genauere Vorhersagen über die Natur der zusätzlichen Quelle erlauben.

Contents

Contents

Space: the final frontier. This is the story of AMS-02. Its long duration mission: explore new physics, seek for dark matter and antimatter, precisely measure, like no one has measured before.

1. Introduction

After a century of great discoveries in particle physics leading to the development of a standard model, open questions remain unanswered. Why is our known universe made up only of matter? If the universe was created in a big bang, matter and antimatter would have been produced in equal amounts, so how did the antimatter vanish? The standard model does not provide a mechanism strong enough to explain this absence.

Cosmological observations tell us that all of the matter we know only makes up about 5 % of the energy in the universe. The main part of matter required to explain the observations must therefore be "dark", meaning to be interacting not electromagnetically but only gravitationally and possibly weakly. What is this mysterious Dark Matter made of? As neutrinos have too small masses to explain the observations, again the standard model of particle physics does not provide us with a good particle candidate that could represent this Dark Matter.

This clearly demonstrates that, although the standard model has been well tested and the recent discovery of the long searched for Higgs boson [1, 2] affirms it yet again, it cannot be the final answer.

Great potential to answer some of the open questions lies in the relatively new field of astroparticle physics, which interlinks astronomy, cosmology and particle physics. Cosmic rays (CRs) have led to many discoveries in the last century in particle and astroparticle physics, the positron [3], muon [4] and pion [5] were first detected by looking at cosmic rays. Still their full potential has not been exploited yet. The energy of cosmic rays spans over many orders of magnitude: from below 10^3 eV up to 10^{20} eV. The low energy part is produced by supernova explosions in our galaxy, whereas cosmic rays of the highest energies above 10^{17} eV originate from outside our galaxy, supposedly created in active galactic nuclei [6]. These high energies cannot be reached by accelerators on Earth, which makes the measurement of cosmic rays the only possibility to study particles of such energies. The flux of cosmic rays ϕ follows a power law spectrum $\phi \propto E^{-d}$ with a spectral index d~3. Therefore large detection acceptances are needed in order to measure high energy cosmic rays. As energetic cosmic rays interact with gas molecules when entering the Earth's atmosphere, the atmosphere can be used as a calorimeter for cosmic rays. Although this makes it difficult to reconstruct their energy and identity with a high precision, still ground based experiments are the only means to detect the highest energetic CRs with a reasonable rate. Space based experiments focus on the precise measurement of cosmic rays of energies up to 10^{12} eV, as they measure the primary cosmic rays flux directly, but they are limited by their possible size. They have to withstand strong vibrations and many g-forces, when launched into space and are limited in power consumption as they rely on the supply by the satellite they are mounted on. Another challenge is the automated operation of the

detector without maintenance and the requirement to be radiation-hard.

In this light the Alpha Magnetic Spectrometer, AMS-02, has been designed and built. The detector was flown to the International Space Station (ISS) with Space Shuttle Endeavour on the 16th of May 2011 and mounted on the ISS on the 19th of May. It is measuring the cosmic rays with unprecedented precision up to high energies in the TeV range for more than two years now. Taking advantage of the ISS as a unique space laboratory allows for an extraordinarily long expected operation of 17 years, which for the first time permits the investigation of long term effects in the cosmic ray fluxes with the same instrument. In addition the size of AMS-02, made possible by the location on the ISS, leads to a full detector acceptance of $\sim 420 \ cm^2 \ sr$, which exceeds the acceptance of previous space spectrometers by more than an order of magnitude.

The AMS-02 detector consists of a Transition Radiation Detector (TRD), a Time-of-Flight system, a silicon Tracker, a Ring Imaging Cherenkov detector and an Electromagnetic Calorimeter (ECAL). The subdetectors measure all particle properties redundantly like the charge of the particle as well as its velocity, momentum and energy. In order to uniquely identify the particle species the charge and mass of the particle need to be known. The precise determination of the momentum and/or energy of the particle, which allows to reconstruct the particle mass, and the redundant measurements of the particle charge by AMS-02 lead to high precision in the particle energy spectra. In the search for the missing antimatter, AMS-02 would therefore be able to reduce the upper limit of the $\bar{He}/He$-ratio by three to six orders of magnitude [7]. The high precision measurement of the cosmic ray particle fluxes will shed further light on the nature of Dark Matter. Especially the antimatter spectra with their low flux of ordinary cosmic rays will provide useful information as weakly interacting massive particles, the most promising Dark Matter particle candidates, can produce positrons and antiprotons in their self-annihilation in our galaxy [8].

The goal of this thesis is to optimize the performance of the Transition Radiation Detector and subsequently determine the positron fraction in the CR lepton flux. The TRD is one of two main constituents of AMS-02 to distinguish leptons from heavier particles. Exploiting the redundant measurements of the TRD and the ECAL, both subdetectors can be calibrated with real data recorded in space to improve their separation capabilities. The combined proton rejection is sufficient to suppress misidentified protons in the much less abundant positrons. A positron sample with a purity above 99% can be retrieved, which is needed in order to determine the positron fraction with a small uncertainty.

Measurements of the positron fraction by previous experiments have indicated a contribution by an additional source to the production of high energy positrons [9, 10], which so far is not clearly assignable. The two most common presumptions for the source of the additional positrons are the production of high energy positrons by nearby pulsars [11] and the annihilation of Dark Matter particles in our galaxy [12], having positrons among their final annihilation products. Therefore the measurement of the positron fraction with a high accuracy to high energies is of great interest. In the course of this thesis an analysis of the first 18 month of AMS-02 data has been performed. About 7 million leptons have been identified and used to determine the positron fraction from 0.5 GeV to 350 GeV.

In the first chapter of this thesis the theory and detection mechanisms of cosmic rays are introduced and the basics of Dark Matter and the antimatter asymmetry are presented. In the following chapter the AMS-02 detector is introduced. The construction and testing of the detector is outlined and its main subdetectors are described as well as the data acquisition and the operation of the detector on the International Space Station. Chapter 4 explains in detail the design and operating principle of the Transition Radiation Detector. The utilization of missing signals in the TRD, investigated as part of this thesis, are presented in chapter 5. They are used in a new alignment algorithm as well as in a refinement of the particle track reconstruction for the TRD. Chapter 6 describes the main capabilities of AMS-02 to distinguish positrons from protons and introduces the discriminating variables and their separation power. Here the TRD likelihood method, which was developed as part of this thesis and is now available in the common AMS software, is described. In chapter 7 the determination of the positron fraction is presented. First the event selection is given followed by the determination of the residual backgrounds. The background induced by wrongly identified protons is determined from data, whereas the residual contamination by electrons due to charge confusion is estimated from Monte Carlo (MC) simulations. The final result is presented followed by the conclusions in chapter 8.

2. Theory of cosmic rays, Dark Matter and baryon asymmetry

Astroparticle physics is a relatively new field of physics, which studies the abundance, origin and propagation of cosmic rays and links them to astrophysics and cosmology.

The measurements of charged particles and photons of extraterrestrial origin enabled us to get to our current understanding of the origin and the evolution of the universe. By looking at the distribution of the cosmic microwave background, a relic from the early universe, the big bang model became much more quantitative [13]. From studying the expansion rate of the universe, which can be done by using Supernovae Ia as standard candles to determine distances [14], its age has been estimated to be about 14 billion years [15]. Measurements of the same supernovae also lead to the conclusion that the expansion of our universe is accelerating [16, 17]. To explain these measurements a force counteracting gravity is needed. Since the origin of this energy is still unknown it is referred to as Dark Energy [18]. Dark Matter has been introduced in 1932 by Carl Zwicky [19] in order to explain high velocities of individual galaxies in the COMA galaxy cluster, which cannot be explained by the luminous amount of matter. The nature of Dark Matter is a mystery, although it constitutes 27 % of the total energy in our universe and therefore by far exceeds the fraction of matter, which is made up of the standard model particles. Another puzzling question today, is the reason for the asymmetry in the abundance of matter and antimatter in our universe.

The lack of knowledge of such fundamental properties of our universe is the motivation for many experimental studies. There is hope to answer some of today's open questions with cosmic ray physics.

Cosmic rays are measured by a variety of experiments based on ground, reconstructing the particle from the properties of the initiated air shower, and in space directly probing the particle properties. AMS-02 [20] is doing the latter.

In the first section of this chapter cosmic rays are described including the history of their discoveries, production mechanisms, propagation through the galaxy and the different measurement techniques used to detect them. The second section describes the phenomenon of Dark Matter and how experiments try to detect it directly or by measuring its annihilation products. Section 2.3 gives some insights on antimatter and the mystery of its absence in the known universe.

2.1. Cosmic rays

Cosmic rays were first spoken of, when Theodor Wulff tried to prove the terrestrial origin of the observed gamma radiation by measuring the ionization in air at the bottom and at the top of the Eiffel tower in 1909 [21]. The measurements contradicted his assumption, as the ionization did not decrease with height. Victor Hess was the first to hypothesize and prove in the early 1910s that the origin of the radiation was indeed extraterrestrial by executing balloon flights with higher precision electroscopes than utilized before. He measured the ionization in the air up to heights of 5 km and observed a strong increase at high altitudes [22]. He concluded that there must be radiation penetrating the Earth's atmosphere from outer space. Hess was awarded the Nobel Prize in Physics for his discovery in 1936. Millikan confirmed his measurement in 1925 and coined the term 'cosmic rays' [23]. Soon thereafter experiments started to investigate the nature and composition of these cosmic rays and discovered their deflection in the Earth's magnetic field, yielding the knowledge that at least parts of the radiation must carry an electric charge [24]. A charge asymmetry favouring the positive side was found by looking at the direction of arrival of the particles by Bruno Rossi [25] and in the following years the primary cosmic rays were found to consist mostly of protons with about $\sim 10\%$ helium nuclei and $\sim 1\%$ of heavier nuclei of elements up to lead [26]. Rossi and Pierre Auger independently observed that from time to time they measured coherent signals by detecting devices set up far apart from each other [27, 28]. Auger concluded that high energetic primary cosmic ray particles must be interacting with air nuclei in the higher layers of the atmosphere, which initiate a cascade of secondary particles producing extensive showers. Due to the short lifetime of produced pions in these nuclear interactions, mainly leptons and photons are detected at sea level.

Carl Anderson discovered the positron in 1932 as the first antimatter particle, while measuring the cosmic rays with a cloud chamber. He detected a particle with a curvature matching the energy-to-mass ratio of an electron but bending in the opposite direction and therefore having the opposite sign of charge [3]. He received the Nobel Prize in Physics for his discovery in 1936 together with Viktor Hess. It was also Anderson, who discovered the muon, the heavier version of the electron [4]. In 1936 he detected negative charged particles in the cosmic rays, whose curvature was smaller than electrons passing through a magnetic field. Assuming them to have the same magnitude of charge, he concluded that they must have a higher mass. In these times, the accelerator physics were still in a premature state, which made observations of cosmic rays the only opportunity to analyse high energetic subatomic particles. It was therefore also in cosmic rays that the first mesons, the charged pions, were discovered. In 1947 a group of physicists from the University of Bristol placed photographic emulsions at high altitude sites and detected the particle by its typical signature of a track with uncommon curvature and changing its curvature as it decays into a muon [5].

Another important particle physics discovery, the oscillation of neutrino flavour, was made by looking at cosmic rays. Measuring the solar neutrino flux with the Homestake Experiment [29], a deficit compared to the expected flux was found. Pontecorvo 1968

proposed that the deficit could be due to a change in the neutrino flavour, if neutrinos would be massive [30], but back then neutrinos were thought to be massless according to the standard model. Observations of the supernova 1987A neutrinos suggested that neutrinos might actually be massive, but the number of detected neutrinos was too small to manifest it [31]. The convincing evidence for the oscillation of solar neutrinos came from the Sudbury Neutrino Observatory, which detected all neutrino flavours coming from the Sun and could distinguish between electron neutrinos and other neutrino flavours [32].

The study of cosmic rays contributed greatly to the field of particle physics as mentioned above. Still the impacts it has on our understanding of the forming and development of our universe are even greater.

The cosmic microwave background (CMB) was discovered unintentionally by Penzias and Wilson in 1965 [33], who were assigned the Nobel Prize in Physics for their discovery in 1978. They were building a microwave receiver to be used in radio astronomy and satellite communication experiments, but could not understand the 3.5 K antenna temperature excess, they were seeing. The CMB had been predicted by Alpher and Herman [34] as an argument for the big bang theory. If the universe had formed in a big bang and has been expanding ever since, the high energetic radiation from the "time of last scattering"[1] would have cooled down to a temperature around 5 K.
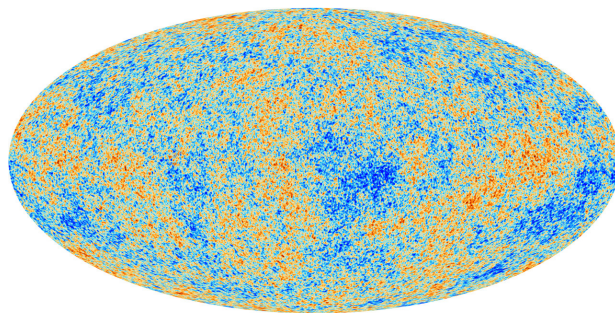

Figure 2.1.: ***The cosmic microwave background as measured with the Planck satellite.*** Temperature fluctuations around the average 2.7255 K are shown as color differences ranging from blue (-500 μK) to red (+500 μK). The background of our own galaxy was subtracted. [15]

A first precision measurement of the CMB was made by the COBE satellite [35] followed by WMAP [36]. Recently the first results of the Planck satellite were published, which measured the temperature fluctuations with an accuracy of the order 10^{-6} [15]. The

---

[1]This refers to the age of the universe, at which the formation of atoms began and the universe got transparent to radiation, 380,000 years after the big bang.

precise measurement of the cosmic microwave background, as shown in figure 2.1, allows to determine the anisotropy of the CMB. The angular power spectrum is an indicator for many cosmological phenomena; in the first place the position and height of its prominent peaks confirm the big bang theory and ruled out other competing models [37]. It also allows to predict the amount of Dark Matter in our universe as will be discussed in section 2.2.

In the following the current knowledge of mechanisms to produce and accelerate cosmic rays are presented and their propagation through the galaxy is discussed. Following this the different measurement techniques of cosmic rays with space or balloon experiments and ground based detector arrays are introduced.

2.1.1. Sources of cosmic rays

Charged particles propagating through the interstellar magnetic field are deflected in such a way that any information about the location of cosmic rays sources is washed out and the flux is isotropic. This makes it nearly impossible to identify single cosmic rays sources.

There are many possible source candidates, including supernovae (SN), active galactic nuclei (AGN), pulsars and gamma-ray bursts. Still the fractions the different production mechanisms are contributing for each particle species are unclear.

Sources of cosmic rays detected at Earth[2], at least up to particle energies of 10^{17} eV, are supposed to be located within our galaxy [38,39]. Supernovae are the most commonly accepted source of the bulk of galactic cosmic rays [40]. A process leading to a supernova explosion is a core collapse, where the nuclear fusion of a massive star suddenly becomes unable to withstand its own gravity any more. If the release of gravitational potential is sufficient the outer layers of the star are violently expelled and by this high energetic cosmic rays are produced.

The total power W_{CR} needed to account for the average energy density of $\rho_E = 1 eV\,cm^{-3}$ in our galaxy with a radius of $R \sim 15$ kpc and a disc thickness of $D \sim 0.2$ kpc[3] is:

$$W_{CR} = \rho_E \pi R^2 \frac{D}{\tau} = 2 \cdot 10^{41} Jyr^{-1}, \tag{2.1}$$

where $\tau \sim 3 \cdot 10^6$ years is the average age of a cosmic ray particle in the galaxy.

The described Type II Supernovae explosions eject material of about ten solar masses with a velocity in the order of $10^7\ ms^{-1}$. Approximately one or two of these explosions occur in our galaxy per century. From this follows that a transfer of only 1 % of their kinetic energy to relativistic particles would be sufficient to explain the energy density in the galaxy [41].

While hydrogen, helium and traces of lithium were produced during the big bang, heavier elements are only synthesized in stars and ejected by supernova explosions. This is reflected in the relative composition of cosmic rays, being $\sim 90\%$ protons, roughly 10% helium

---

[2]This refers to CRs detected in the vicinity of our planet, not to ground based experiments.
[3]1 parsec (pc) = 3.26 light years = 30.9 trillion km

and about 1% heavy nuclei [26]. Also electrons produced in the fusion processes of stars constitute primary cosmic rays. Positrons and antiprotons are not injected by supernova explosions, but are produced in interaction processes of the primary cosmic rays with the interstellar medium and therefore referred to as secondary cosmic rays.

Another source of electromagnetic cosmic rays are pulsars [42]. The first pulsar was observed in 1967 by Jocelyn Bell and Antony Hewish [43], who was awarded the Nobel Prize in physics for this observation. They are formed, when a massive core collapse results in a neutron star. The neutron star retains most of its angular momentum, while its radius is greatly reduced, which leads to a high rotational speed. Electromagnetic radiation is ascribed to the existence of a magnetic dipole inside the pulsar, which induces an electric field by the rotation of the strong magnetic field. The axis of the magnetic field of the neutron star does not necessarily coincide with its rotational axis. The presence of a tilt gave this object its name, because the radiation emitted in a beam along the magnetic axis is only seen in short pulses at each rotation of the object, when the beam actually points to the observer [41]. Pulsars are supposedly contributing to the production of electrons and positrons in the cosmic rays, where positrons were conservatively thought to be only the product of primary cosmic rays interacting with the interstellar medium. A number of pulsars detected with the Fermi Gamma-ray Space Telescope in our galaxy are displayed in figure 2.2.
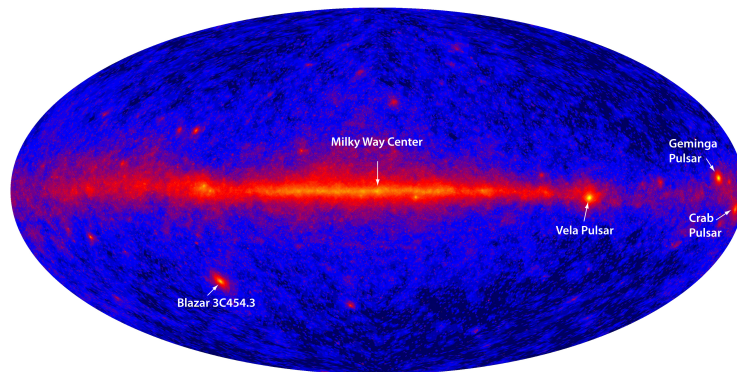

Figure 2.2.: ***Identified pulsars by the Fermi Gamma-ray Space Telescope.*** Vela, Geminga and Crab (on the right) are the brightest pulsars Fermi sees. credit: NASA/DOE/LAT Collaboration [44]

The flux of electrons and positrons produced by pulsars $\phi_{e\pm}^{\text{pulsar}}$ can be expressed as a single power law with a spectral index γ_s and a cut-off energy E_s [11]:

$$\phi_{e\pm}^{\text{pulsar}} = C_s \, E^{-\gamma_s} \, e^{-E/E_s}. \tag{2.2}$$

The age of the pulsar determines the amount and maximal energy of produced electrons and positrons [11]. The distance of the pulsar to the observer at Earth is also important for the observed energy spectrum due to energy losses during the propagation through the galaxy, as will be described in the next section.

2.1.2. Propagation of cosmic rays

Supernovae have been proposed to be the main source of the cosmic rays. In the following the propagation of cosmic rays through our galaxy is discussed, which determines the observed energy spectra of the participles.

Enrico Fermi suggested two mechanisms explaining how the cosmic ray particles could be accelerated. His first proposal was the acceleration of particles in the environment of moving magnetized gas clouds [45]. A particle would gain energy in a head-on collision with the magnetic mirror, but loose energy in a head-tail collision. In a random-motion process an effective positive acceleration statistically originates from the fact that there is a floor ($E_{kin} = 0$) but no ceiling to the possible final kinetic energy of the particle. The gain of energy at each collision is proportional to $(v/c)^2$, giving it the name of second order Fermi acceleration. The resulting acceleration due to this process, though, is quite slow and insufficient to explain the energy spectrum of CRs due to the energy losses at each stage.

Fermi proposed another acceleration mechanism near shock fronts [41]. Here the energy gain is of first order in v/c, leading to the name of first order Fermi acceleration. A particle crossing a shock-front is scattered back by the gas behind the front with a velocity component in the direction of the shock. If the particle is then scattered backwards again for example by a magnetic cloud, it can undergo the acceleration process multiple times. Possible sources of the shock fronts are supernovae shells, but also solar and galactic winds [46]. Due to the probability to escape from the acceleration zone after each reflection the resulting energy spectrum follows a power law for many particles experiencing first order Fermi acceleration:

$$\frac{dN(E)}{dE} \propto E^{-p} \tag{2.3}$$

with the spectral index p $\sim$ 2. The difference to the measured spectral index of 2.7 for protons, which make up the bulk of the cosmic rays, could be due to the energy dependent containment time of the CRs in the galactic disc.

X-ray data from the remnant of a supernova detected in 1006 by Chinese astronomers confirms the acceleration of electrons in supernova remnants [38]. Just recently also proof for the acceleration of protons in supernovae remnants has been found by identifying the pion-decay feature in the gamma spectrum of two SNRs in data of the Fermi experiment [47].

The Lorentz-force acting on charged particles in magnetic fields is deflecting their direction of propagation. Because the deflection is proportional to the energy of the particle, only with particles of the highest energy any accurate pointing can be done.

The propagation of cosmic rays through our galaxy, taking different influences into account, can be expressed with the transport equation [48]. The contributions are:

- source term, representing the production sites of cosmic rays (e.g. Supernovae)

- diffusion, which relates to the random walk of particles in the interstellar medium due to resonant scattering off magnetic field turbulences

- convection, for example by galactic winds

- diffuse reacceleration, as in supernova remnants

- energy losses, caused by radiation (e.g. Bremsstrahlung, inverse Compton scattering, synchrotron radiation) and ionisation processes

- losses in number of particles, due to fragmentation and radioactive decay.

The escape of particles out of our galaxy is taken into account by the boundary condition, when trying to solve the transport equation numerically as can be done with publicly available codes like GALPROP [48] and DRAGON [49]. The transport equation has many free parameters, which can be determined by a fit to measured data. As an example, the diffusion coefficient and halo size are sensitive to the measurements of secondary nuclei and radioactive nuclei. Therefore they are mainly determined from ratios as boron to carbon (B/C) or $^{10}Be/^{9}Be$ [48]. The retrieved model can make a prediction for the production of secondary positrons due to the interaction of protons with gas molecules N_{gas} in the interstellar medium [50]:

$$p + N_{gas} \rightarrow \pi^{\pm} \rightarrow e^{\pm} + \overset{(-)}{\nu} \tag{2.4}$$

The proton flux has been measured with high precision [51] and the proton-nuclei interaction properties are well known, as is the production of electrons and positrons in pion decays [52]. Therefore a prediction of the flux of the produced positrons can be made. This flux can be approximated by a single power law, just as the energy spectra of electrons in CRs. The production of secondary electrons and positrons is described by a lower spectral index than the production of electrons in supernovae, hence the electron flux is dominated by the latter [50]. This leads to a decrease of the positron fraction $e^{+}/(e^{+} + e^{-})$ with energy in the case of solely secondary cosmic ray positrons [53].

The results can be taken into account as a background to the production of positrons by additional sources, which relates to the topic of this thesis.

2.1.3. Cosmic ray detection

Our current knowledge of cosmic rays arises from their measurement by many different detection techniques. Cosmic rays interact with the gas of our atmosphere, as a consequence they cannot be measured directly on ground. The air shower they initiate in these interactions, though, can be detected. For this large detector arrays are needed, because the showers extend over large distances depending on the particle energy.

In order to measure the primary particles directly one needs to go to space. This is done in satellite missions, which operate in near Earth orbit and last several years, and in balloon flights, which reach heights of the stratosphere. The different measurement methods focus

on distinct energy ranges and thereby supplement each other. A compilation of available data from different experiments ([54] and references therein) over a wide energy range is shown in figure 2.3 with indication of the different measurement regimes of the methods.
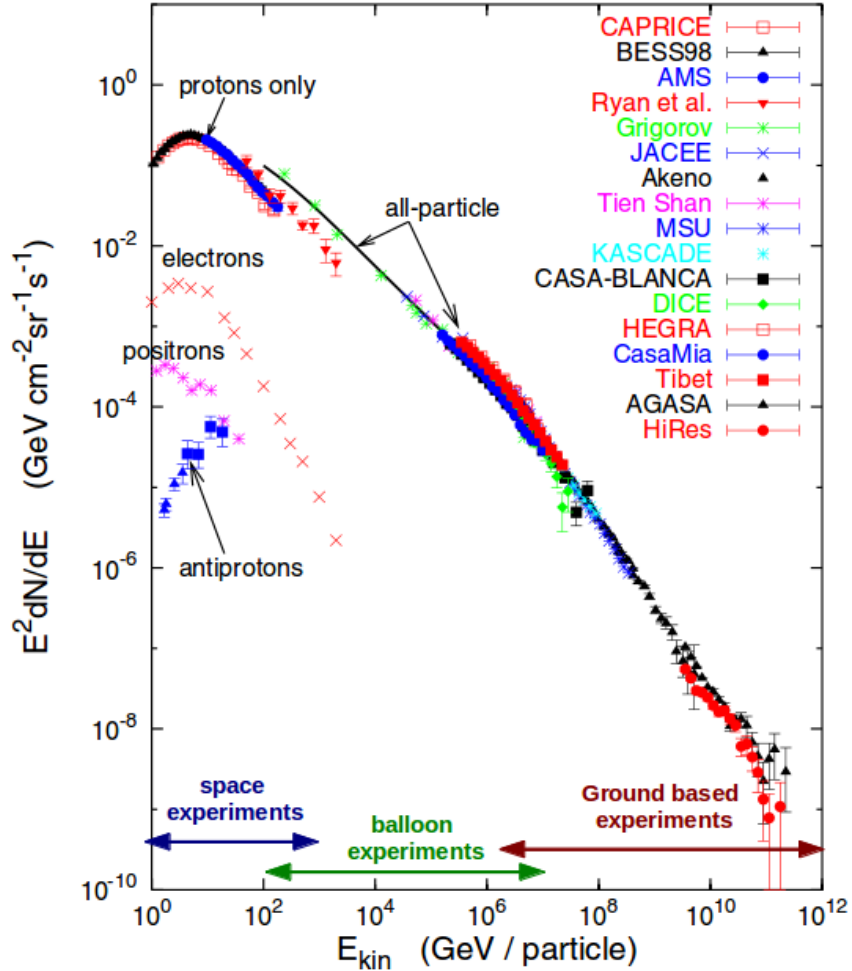

Figure 2.3.: ***Cosmic ray spectra.*** Space experiments focus on the energy range from 100 MeV to 1 TeV, balloon experiments are sensitive to the particle flux from 100 GeV to 1 PeV and ground based experiments focus on the highest energies [54].

Two breaks in the spectra of cosmic rays are visible. The first one called the knee at around 10^{16} eV is due to the beginning of the end of the contribution of galactic production mechanisms, which are widely believed to be primarily supernova remnants. The flux of light nuclei decreases, which leads to a steepening of the spectra as the primary composition of the cosmic rays becomes heavier [40]. The second one is called the ankle and shows a flattening which occurs at $\sim 10^{18}$ eV. Though little is known about the highest energy

cosmic rays due to their low abundance, there are indications that particles above the ankle could be produced in nearby active galaxies [6].

In the following the different measurement methods of cosmic rays are being introduced.

Balloon experiments

Balloon experiments have the longest history in the detection of cosmic rays, as their existence was proven with this technique by Victor Hess. Since then many series of balloon experiments have been conducted. The single missions can last up to a month with the balloons inclining to heights of 40 km. The detectors are capable of measuring the charge and energy of the particles, thereby providing precise measurements of the energy dependence of the elemental spectra. The energy range they measure lies between 10^{11} eV and 10^{16} eV. Two of the most recent experiments are CREAM [55] and TRACER [56].

Satellite experiments

Satellite experiments benefit from their long duration of multiple years and their close to 100 % sky coverage due to their near Earth orbit usually at a height of 400 km to 600 km. There are gamma ray telescopes (e.g. FERMI [57]) and spectrometers (e.g. PAMELA [58]) measuring the primary cosmic rays in the outer layers of our atmosphere up to energies in the TeV range. Exploiting the ISS as a space laboratory, AMS-02 profits of the large bandwidth using the ISS communication channels to downlink the recorded data. It also allows for the unprecedented size of a spectrometer to be operated in space, which was only limited by the dimensions of the Space Shuttle cargo bay. A detailed description of AMS-02 is given in chapter 3.

Ground based experiments

In order to study the highest part of the energy spectrum of cosmic rays, a large detector acceptance is needed due to their low abundance. Since this cannot be achieved by space experiments, these particles need to be measured on ground. Due to the interaction of the primary cosmic rays with the gas in our atmosphere, only the secondaries of these interactions can be detected. There are several detector techniques in use to reconstruct the primary cosmic ray from measuring the properties of their induced air shower. Mentioning just a few of the entirety of the methods depicted in figure 2.4, Air Cherenkov telescopes measure the Cherenkov light emitted by the particle as it traverses the atmosphere. They have a limited field of view and short active measuring time, since they can only measure during clear nights without disturbing moonshine. The efficiency of Cherenkov telescopes can be improved by using water tanks as the medium in which the radiation is produced. The secondaries of a CR entering the atmosphere can also be detected by extensive arrays of scintillation detectors. Yet another option to detect the air showers of cosmic rays is measuring the fluorescence light emitted by nitrogen molecules, which were excited by the shower particles.
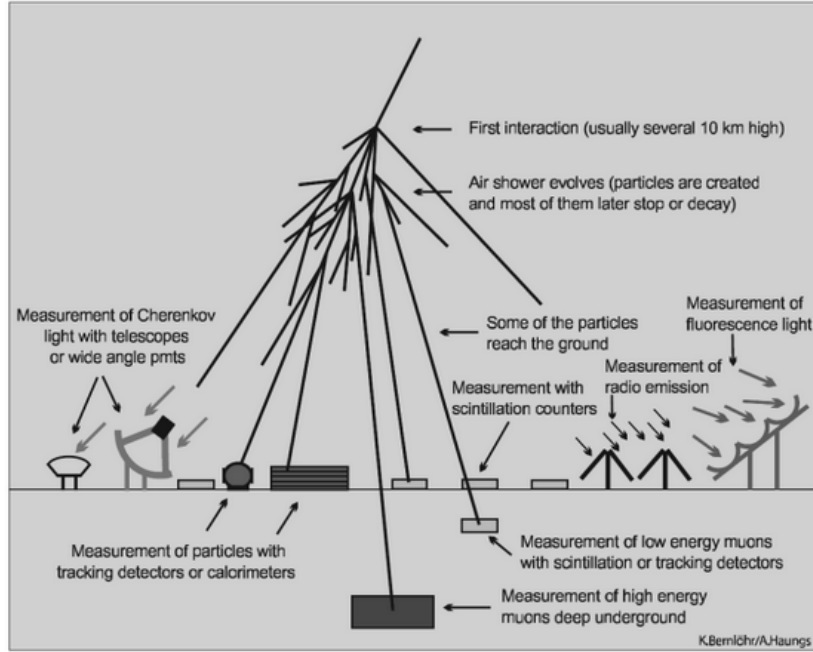
Figure 2.4.: ***Ground based measurement techniques of cosmic ray air showers.*** [59]

The best performance is obtained with hybrid measurements, i.e. when two measurement techniques are combined, for example if fluorescence detectors measure the induced air shower and Cherenkov arrays determine its footprint on Earth. Prominent experiments to be mentioned here are the Pierre Auger Observatory [60] and KASKADE-Grande [61].

2.2. Dark Matter

The existence of Dark Matter (DM), historically termed due to its absence of luminosity, has been proposed by Fritz Zwicky and Jan Oort as early as 1933 [62]. Today "dark" is referring to the inability of this kind of matter to interact electromagnetically [63]. The virial theorem states that the kinetic energy of objects should on average be half of their gravitational binding energy [19]. Observations of the velocity of stars in the Milky Way and of galaxies in the Coma cluster could not be explained by the amount of visible matter [19]. Looking at the rotation curves of stars in spiral galaxies also yields strong evidence for 'missing mass'. A star of mass m at a distance r from the galactic center moving with tangential velocity v experiences the centrifugal force, which must be balanced by the gravitational force:

$$\frac{mv^2}{r} = \frac{mM(<r)G}{r^2} \tag{2.5}$$

with $M(<r)$ referring to the mass of the objects inside radius r and G being the

Gravitational constant. For a spiral galaxy as our own, this would lead to a decrease in the velocity for stars located at large distances from the galactic center. Instead, what has been observed are quite flat rotational curves, as the one shown in figure 2.5 [64]. This has led to the suggestion that the bulk of mass in such galaxies must be accounted for by Dark Matter distributed in a halo [65].
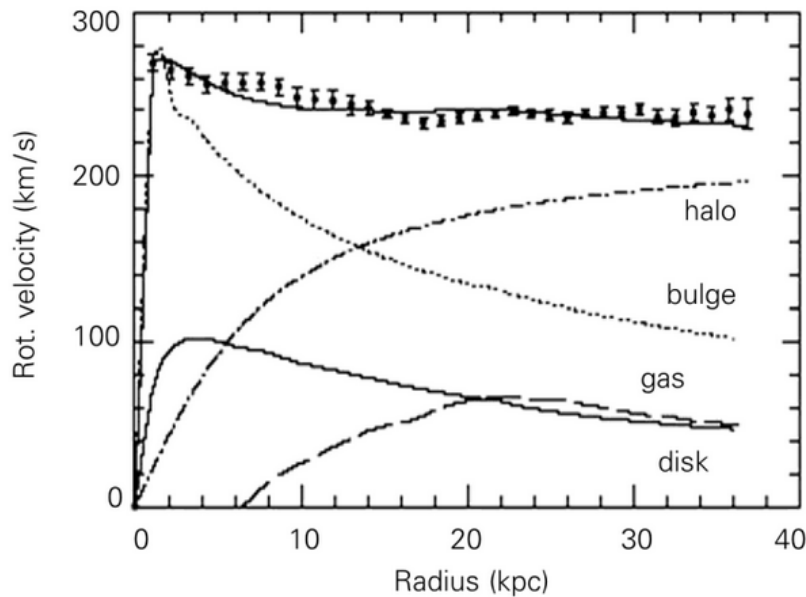

Figure 2.5.: ***Rotational curve of galaxy NGC 7331.*** Estimations of the contribution of disk (solid line), bulge (dotted line) and halo (dot-dashed line) are fitted to the observed data (points) and their combination is illustrated as the solid line through the points [66].

Vera Rubin measured the rotational curves of a large number of galaxies with a high precision to determine the fraction and distribution of Dark Matter in those galaxies. She came to the conclusion that mass density in the galaxies must be uniform even for distances well beyond the galactic bulge and that most of the galaxies contained six times more Dark Matter than luminous matter [67].

Another observation, which pointed to the existence of Dark Matter, was the survey of galaxy clusters, which showed that much of their visible mass is in the form of hot gas, which emitted X-rays. From the measured radiation, the gas temperature could be estimated. It was found that such high temperature implied velocities of gas particles by far exceeding the escape velocity determined from the visible mass [68].

An independent need for Dark Matter comes from looking at the fluctuations in the cosmic microwave background. The CMB is the relic thermal radiation from the time of last scattering approximately 380.000 years after the big bang, when the universe got transparent to radiation due to the formation of atoms. The CMB fluctuations allow to determine the absolute fraction of Dark Energy and Dark Matter in our universe. The

comparison of the height of even to odd peaks in the anisotropy spectrum, given in figure 2.6, indicates the density of baryonic matter. Baryons in equilibrium with photons shift the zero-point of the acoustic oscillation making the compressional peaks (odd) larger than the rarefractive peaks (even) [69]. The third peak just above 0.2° gives the density of Dark Matter, as it is sensitive to the total matter content of the universe. Matter in general does not lead to the enhancement of odd over even peaks, but simply to a reduction of all peaks [70]. Therefore balancing these two effects to match the data [15], the total matter content, the baryonic component and the Dark Matter contribution can be calculated. The standard model of big bang cosmology, called ΛCDM [71], has been set up as the simplest model to provide explanation for the CMB and its fluctuations as well as the accelerating expansion of the universe [16, 17]. The cosmological parameter Ω is the ratio of actual energy density ρ to the critical density[4] ρ_c:

$$\Omega = \frac{\rho}{\rho_c}. \tag{2.6}$$

Parameters of this model include Ω_T, Ω_Λ, Ω_B and Ω_D referring to the total energy density of the universe, the Dark Energy density[5], the energy density fraction of baryons and of Dark Matter, respectively. $\Omega_k = 1 - \Omega_{tot}$ indicates the topology of the universe, with $\Omega_k = 0$ representing a flat topology.

The first Planck data [72] determined the total energy density $\Omega_T = \Omega_\Lambda + \Omega_{\text{matter}}$ to be unity, which indicates a flat universe. Using the precise measurement of the acceleration of the universe $a = \Omega_\Lambda - \Omega_{\text{matter}}$ by supernovae observations [16, 17], the degeneracies in the CMB power spectrum are broken, which improves the precision of the determination of the cosmological parameters [73]. The combination of these observations yields $\Omega_\Lambda = 68.3\%$, with the Dark Energy being the accelerating force in the expansion of the universe and today being matched with a vacuum energy density, $\Omega_B = 4.9\%$ and $\Omega_D = 26.8\%$ as illustrated in figure 2.6.

Another important detection mechanism for Dark Matter is gravitational lensing. Einstein's general theory of relativity predicted gravitational deflection α of photons passing by a point mass M at a distance of closest approach b to be given by the formula [41]:

$$\alpha = \frac{4GM}{c^2 b}, \tag{2.7}$$

with G the gravitational constant and c the speed of light.

The gravitational lensing effect of this deflection was first tested and confirmed in 1919 by the solar eclipse expedition [74]. As a result of this effect a distant source of light with massive objects in the path of sight of the observer will be seen as multiple images or even a ring in the case of collinear orientation. The observed effect is the gravitational analogue to a thin lens system in optics. Even if the produced images by gravitational lensing cannot be resolved, it can be detected by an amplification of the intensity, this effect is called microlensing or weak gravitational lensing. The search for Dark Matter

---

[4]The critical density refers to the density of a topologically flat universe.

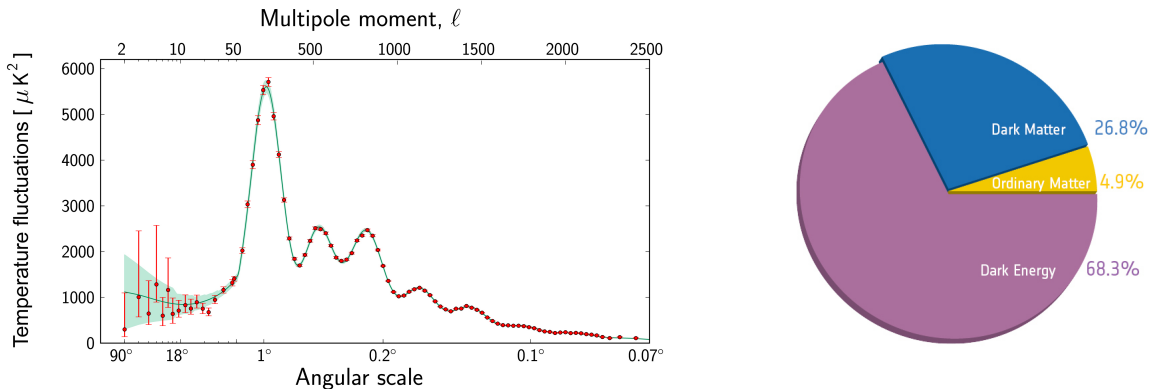[5]Dark Energy is often also referred to as the cosmological constant.

Figure 2.6.: ***Composition of the total energy density of the universe derived from the angular spectrum of the CMB.*** Left: angular power spectrum of the CMB measured from Planck data. Red: measurements, green: model fit. Right: composition of the total energy density derived from the Planck measurement. [15]

by the gravitational lensing effects is an independent way to determine its amount and distribution from the previous introduced dynamic effects. Statistical measurements in vast galaxy surveys have determined the Dark Matter distribution and come to the same conclusion on the mass-to-light ratio as the other observations have [75].

In the next sections possible Dark Matter particle candidates and experimental searches for Dark Matter are presented.

2.2.1. Particle candidates

There is a wide variety of proposed Dark Matter candidates. First we consider the baryonic fraction of it.

Massive astrophysical compact halo objects (MACHOs) have been detected with the gravitational lensing technique, but it is yet unknown, which kind of objects they are and which fraction of baryonic Dark Matter they represent [76]. Trying to explain the mass to light ratio in our galaxy or just correlating the observed MACHOs with white dwarfs, neutron stars or black holes raises multiple problems [77]. The progenitors of all these objects must have emitted infrared gamma rays. This would hinder high energetic gamma rays to be detectable at Earth, due to pair production with the infrared photons, but the HEGRA detector has measured multi-TeV gammas [78]. Another problem with baryonic MACHOs arises from looking at the energy density of their progenitors [77]. They would constitute most of the baryonic energy density derived from the CMB observations and for many models even exceed it, which would leave no room for the observed stars. Also the relative element abundances of carbon, nitrogen and helium indicate that only a small fraction of all baryons can have passed through intermediate mass stars, which are the

progenitors of the mentioned Dark Matter candidates [79]. These problems indicate that the detected mass cannot solely be explained with baryonic matter.

Since amongst other observations the CMB anisotropy data tells us that the baryonic contribution to Dark Matter is small [70], we will now focus on non-baryonic Dark Matter.

Neutrinos have always been considered as a Dark Matter candidate as they are weak interacting and need to be massive due to the observation of neutrino flavour oscillation [80]. The masses attributed to neutrinos are much smaller, though, than needed to explain all of the Dark Matter. Also Neutrinos would constitute "hot" Dark Matter, as they were relativistic at the point of decoupling [81]. In this case they would tend to wash out the density fluctuations. The possible contribution of "hot" Dark Matter to the total Dark Matter amount has been simulated to be less than 30 % to match the observed CMB and the large-scale structures at present [82].

Another proposed candidate is the axion [83], which is a hypothetical pseudoscaler particle postulated to resolve the strong CP problem in quantum chromodynamics (QCD). This refers to the fact that charge conjugation together with parity (CP) is conserved in strong interactions, although the theory would permit violations of it. The missing or very small dipole moment of the neutron [84] is a clear indicator that the CP violating phase of QCD must be small. In order to resolve the problem, a new global symmetry was introduced, which becomes spontaneously broken and thereby brings rise to a new particle called the axion. If axions should contribute the bulk of Dark Matter in our galaxy, their decay into two photons should have been observed, although their expected lifetime exceeds the age of the universe for small masses [85]. In order to reach an energy density of the order of the critical density the axion mass would be required to be in the region of $10^{-6} - 10^{-3}$ eV/c^2. Experiments to detect axions have failed so far.

The most promising candidates for Dark Matter are weakly interacting massive particles (WIMPs), which were non-relativistic at freeze-out and therefore constitute cold Dark Matter. The large scale structures in our current universe show that the bulk of Dark Matter must be cold [71], i.e. the particles must have had non-relativistic velocities when they decoupled from other matter. The current estimated relic density of Dark Matter can only be achieved, if the particle-antiparticle annihilation cross-section is not larger than the cross-section of the weak interaction processes [86]. The standard model of particle physics, though, does not provide a particle fulfilling these criteria. An extension of the standard model providing a good WIMP candidate is Supersymmetry (SUSY) [87]. In this theory every particle of the standard model has a super partner with the same particle properties, but different spin. Every fermion has a supersymmetric boson partner as every boson has a sypersymmetric fermion partner. Since supersymmetric particles have not been detected so far, it is evident that the supersymmetric particles cannot have the same masses as their standard model partners. Therefore Supersymmetry needs to be a broken symmetry, leading to much higher supersymmetric particle masses. Indeed, breaking Supersymmetry at the same time solves the hierarchy problem [88], which reflects the problem of power-law divergences of the radiative corrections to the Higgs mass. These disappear by the postulation of the additional supersymmetric particles, because the negative contributions from fermions are cancelled by their boson superpartners and vice versa. Supersymmetry

also provides solutions to other problems of the standard model. For example, including SUSY leads to a change in the energy dependence of the coupling constants α_1, α_2 and α_3, representing the electromagnetic, weak and strong interaction, respectively, in such a way that they intersect in one common point at the Grand Unified Theory (GUT) scale [89], as shown in figure 2.7.
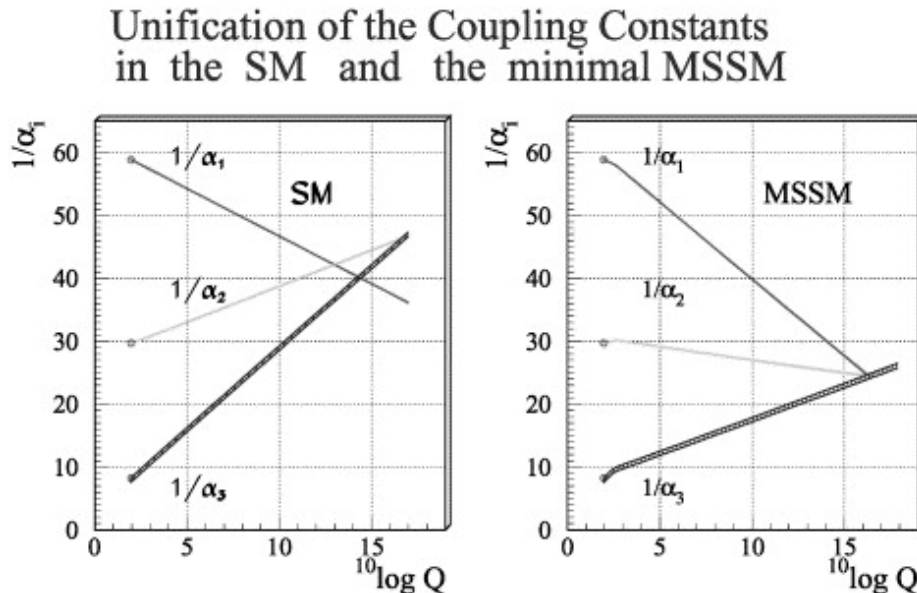

Figure 2.7.: **Impact of SUSY on the running of the coupling constants.** α_1, α_2 and α_3 are the coupling constants of the electromagnetic, weak and strong interaction, respectively. In the supersymmetric model all coupling constants meet in a common point at the so called GUT scale. The thickness of the line represents the error in the coupling constants [90].

In order to not be in conflict with the measured baryon and lepton number conservation, which have been affirmed by the measured proton lifetime [91], a new quantum number, called the R-parity, needs to be introduced. The R-parity is a multiplicative quantum number and has the value +1 for ordinary particles and -1 for supersymmetric particles. As a consequence supersymmetric particles can only be produced in pairs and cannot decay into ordinary particles. This also means that the lightest supersymmetric particle must be stable, which would make it a good WIMP candidate. In the common supersymmetric extensions of the standard model this lightest supersymmetric particle would be a neutralino χ, which is a mixed state of the superpartners of the neutral standard model bosons. Neutralinos are Majorana-particles, meaning that they are their own antiparticles. Therefore two neutralinos could annihilate with each other, illustrated in figure 2.8, and their annihilation products can be ordinary particles as the product of their R-parity is positive [92].

There are many experiments trying to find evidence for the existence of such weak interacting massive particles, which is described in the next section.
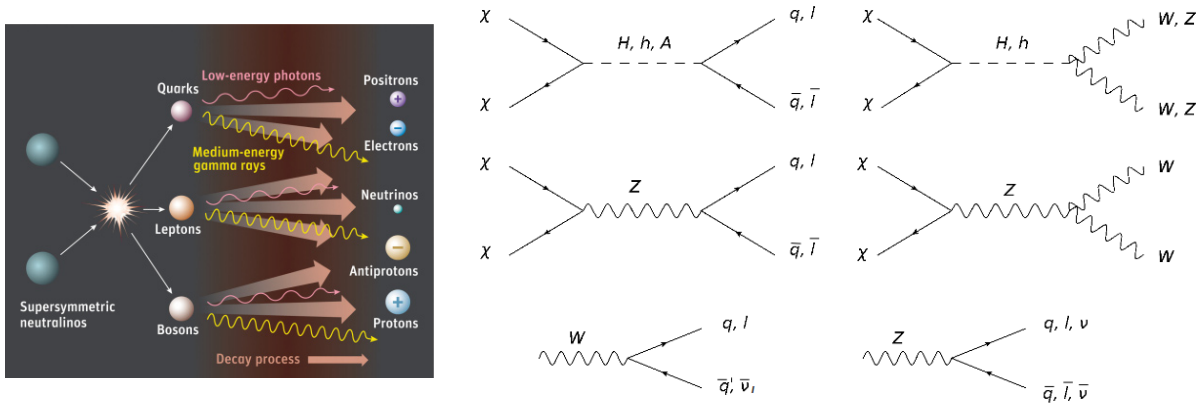
Figure 2.8.: ***Self-annihilation products of two neutralinos.*** The annihilation products can be ordinary matter due to the positive R-parity product.
Left: Illustration (Credit: Sky & Telescope / Gregg Dinderman). Right: Example Feynman diagrams of neutralino annihilation via supersymmetric scaler Higgs (h,H) or pseudoscaler Higgs (A) and Z boson into quarks and leptons and bosons. The W and Z bosons on their part decay again into quarks or leptons, as do the heavy fermions, which leads in the end to final products like protons, antiprotons, electrons, positrons, neutrinos and photons.

2.2.2. Experimental searches for WIMPs

There are two independent methods to detect WIMPs, direct detection via scattering of WIMPs on atomic nuclei [93] and indirect detection looking for the WIMP annihilation signal [94].

Direct detection is done in underground experiments trying to measure the recoil energy of nuclei from an elastic WIMP scattering. To place the experiments underground is motivated by the reduction of background induced by cosmic rays. Two main detection methods are used by different experiments. The first uses a cryogenic detector operated at temperatures below 100 mK, which measures the heat produced by the nuclear recoil. An example of an experiment using this technique is EDELWEISS [95]. The other method to measure the WIMP scattering uses liquid noble gas to detect the light produced in a particle collision in the material. For example XENON100 [96], located in the Gran Sasso National Laboratory, is using 100 kg of liquid xenon to detect Dark Matter particles. Optimal is the combination of both measurement methods in coincidence as it is currently done e.g. in the CRESST experiment [97]. The most important feature in the direct Dark Matter search is handling the background by cosmic radiation and radioactive decays, since the expected event rate is in the order of a few particles per year and kg of detection material [93]. So far none of these experiments have found statistically significant results of Dark Matter particles, but could set upper limits on the WIMP-nucleon scattering cross section [98].

Indirect detection can be done in many different experiments on ground and in space. At the Large Hadron Collider (LHC) [99] WIMPs could be produced in the decay of supersymmetric particles. They would be indicated by a large fraction of missing energy in the event [100].

The above mentioned direction detection techniques as well as the LHC have not been able to identify Dark Matter particles yet. However they can set upper limits on SUSY parameters, reducing the allowed parameter space [101].

WIMPs passing through massive objects as the sun could scatter on atoms and loose energy, which could lead to an accumulation of Dark Matter particles at their center. This would enhance the annihilation rate and high energetic neutrinos ($E_\nu \sim m_\chi/3$) , being the only particle to escape from the suns center, could be detected in contrast to the ordinary MeV solar neutrinos. This effect would be an unmistakable signature of WIMP annihilation [102]. Experiments like IceCube [103] in the Antarctica and ANTARES [104] in the Mediterranean sea might be able to detect such neutrinos in the future.

Another possibility to indirectly measure Dark Matter is to directly measure the products of DM annihilation in our galaxy by spectrometers in space.The combination of the detected signal of the annihilation products together with measurements at the LHC could be used to identify a signal of Dark Matter. A small set of possible annihilation channels of the neutralinos are shown in figure 2.8. Depending on the composition of the neutralino, which is a mixture of gauginos and higgsinos [105], different annihilation channels dominate. In the case of a large bino component, they would predominantly decay via the pseudoscaler Higgs bosons (A) of the supersymmetric extension of the standard model [87]. The final annihilation products include protons, antiprotons, electrons, positrons, neutrinos and photons. Since they are measured together with the standard CR particles, the signal should be most prominent in the e^+ and $\bar{p}$ spectra [8], as the abundance of antiparticles in the CRs is minor compared to the high abundance of protons and also less than electrons, as is shown in figure 2.3.

Gamma-ray telescopes in space and on ground are looking for features in the γ spectrum especially from directions of Dark Matter dominated dwarf galaxies (e.g. [106]).

General particle spectrometers are looking for an excess of positrons and antiprotons in the CRs compared to the expected flux from secondary production by the interactions of primary CRs with the interstellar medium [50]. PAMELA and Fermi have found an indication of an excess of high energy positrons [9, 10], as shown in figure 2.9.

The excess of high energetic positrons can have multiple explanations. The two most common ones are the production of positrons in pulsars [107, 108] or by Dark Matter annihilation [11]. To disentangle these two possible sources is rather tricky. A WIMP signal would lead to a sharp cut-off beyond the WIMP mass, but also the additional contribution by pulsars can create such a sharp drop by adjusting the pulsar parameters within their uncertainties. A more promising way to distinguish the contribution of the two hypotheses is to look at the anisotropy of the excess [109]. Dark Matter particles are supposed to be distributed homogeneously in our galaxy, as a consequence they would produce a isotropic signal. In principle pulsars, being point sources, should have a anisotropic contribution. This anisotropy is washed out, though, by the deflection of the positrons in the galactic
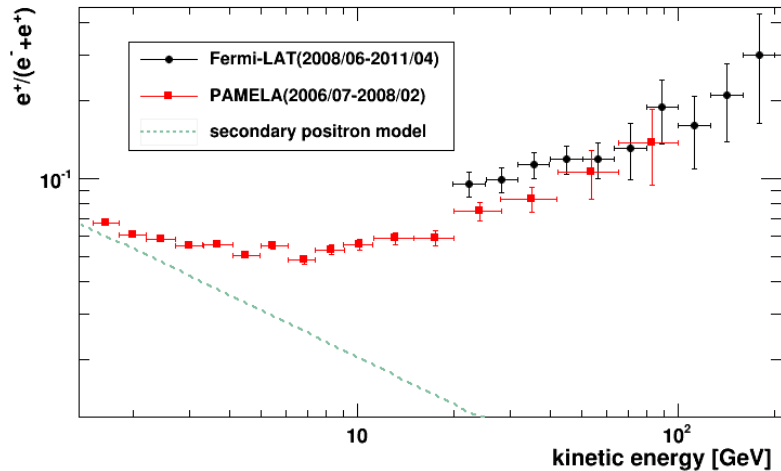
Figure 2.9.: **Measurements of the positron fraction by PAMELA [9] and Fermi [10].** From purely secondary production of positrons in interactions of primary CRs with the interstellar medium one would expect a continuous decrease of the positron fraction towards higher energies (dotted line, simple power law model determined in section 7.4). Therefore the data indicates an additional production mechanism for high energetic positrons.

magnetic field, while propagating towards Earth. Since the production mechanism inside the pulsars is still barely known, the distinction of which, and therefore how many, pulsars could contribute to the positron production is an open parameter. Including multiple pulsars in a model to mimic the observed positron data would lead to a strong reduction in observed anisotropy. Therefore the anisotropy measurement needs to be very precise in order to rule out the pulsar hypotheses and uniquely identify the positron excess with the self-annihilation of Dark Matter particles.

AMS-02 measures the cosmic ray spectra with unprecedented precision up to higher energies to narrow down the possible models. As part of this thesis the measurement of the positron fraction up to 350 GeV will be presented in chapter 7.

2.3. Antimatter asymmetry

Considering the Big Bang hypothesis, particles and their antiparticles should have been produced in same amounts [13]. So why is it that our universe seems to be made only out of matter rather than antimatter? Not that we only don't see antiparticles in our part of the universe, we also don't observe an intense emission of photons, which would follow from the annihilation of matter with antimatter in other parts of our universe.

The origin of the asymmetry is still unknown, but in order to have antimatter asymmetry Andrei Sakharov set up three necessary conditions [110] :

- C-symmetry and CP-symmetry violation

- Baryon number violation

- deviation from strict thermal equilibrium.

After finding the violation of parity transformations [111], the flip of one sign in spatial coordinates, in weak decays, CP transformations, being the combination of parity transformation followed by charge conjugation, have long believed to be conserved. In the 1960s Fitch and Cronin also proved this assumption to be wrong by finding CP violation in weak interactions of neutral kaons [112], mesons consisting of a d-type and a strange flavoured quark. They were awarded the Nobel Prize in Physics for their discovery in 1980. Later the CP violation has also been observed for b-mesons [113, 114]. The observed CP violation is explained by a CP-violating phase in the quark flavour mixing matrix of weak decays [115]. Therefore this criterion is fulfilled theoretically, but the amount of observed CP violation is not nearly sufficient to describe the observed asymmetry between matter and antimatter [116, 117].

In order to explain the mismatch of baryons to antibaryons observed, some interactions that have taken place since their production must have violated the conservation of the baryon number. There are theories beyond the standard model, including Grand Unified Theories [118, 119], in which such processes exist. Also the standard model includes non-perturbative processes [120], which violate the baryon number, but they are small today, because of a large energy barrier. Nevertheless they could have played a role at earlier times of the universe, when thermal energy could have helped particles pass the barrier.

The out-of-equilibrium request is needed, since the in nature conserved CPT symmetry, with T referring to time reversal, leads to same abundances of particles and antiparticles in thermal equilibrium. This is no problem in the Big Bang model as it predicts that particles successively leave equilibrium due to the steady temperature decrease by expansion.

With the possibility of all the criteria being fulfilled, it is not clear, which process is responsible for the evident asymmetry.

AMS-02 is measuring the antimatter spectra of light particles as well as looking for heavy antinuclei. The detection of a single anticarbon would impose the existence of antimatter galaxies in some distant part of our universe, since those particles can only be produced in antimatter stars. With its high sensitivity AMS-02 would be able to lower the limit of the $\bar{H}e/He$ ratio down to 10^{-9} [7].

3. The Alpha Magnetic Spectrometer

The Alpha Magnetic Spectrometer [20] is a general purpose high energy particle detector. It consist of a unique assembly of detector types to be operated in space and by far exceeds previous space experiments in acceptance and planned duration of operation. The detector lifted off from the Kennedy Space Center inside the Space Shuttle Endeavour on the shuttles last mission STS-134 on 16th of May 2011. It was mounted on the ISS on the 19th of May 2011 and started taking data just a few hours after installation. In its first 18 month of operation about 30 billion science events have been recorded and transferred to ground. The detector is supposed to function until the end of operation of the ISS, which might be up to 2028[1]. Therefore only 8% of the total data volume is available by now. The long duration of the experiment allows to track time dependent effects as the impact of the solar activity on the different particle fluxes.

In astrophysics the most important observation is the energy spectrum for identified particles. AMS-02 identifies particles in a redundant way with different types of subdetectors, which use different particle interactions and fundamental forces to reconstruct the particle properties. The subdetectors of AMS-02 are shown in figure 3.1, which shows from top to bottom: a Transition Radiation Detector, a Time-of-Flight system, a silicon Tracker inside a magnet, an Anti-Coincidence-Counter surrounding the Tracker, a Ring Imaging Cherenkov detector and an Electromagnetic Calorimeter.

Since the goal is to measure the cosmic ray particles, the detector is mounted on the ISS in such a way that it points away from the Earth. Only particles traversing the detector from top (TRD) to bottom (ECAL), being measured by all subdetectors, are used for analysis.

In the first section the 16 years of construction and the extensive testing phase of the detector are described. This included multiple integrations and de-integrations of the system and testing of the single constituent parts and also the full system in beam tests. In the subsequent section the subdetectors of AMS-02 are described one by one. Their design and ability to determine the different particle properties are presented. The third section describes the data acquisition chain and data processing of the detector, while the last section outlines the operation of the detector on the International Space Station.

3.1. Construction and testing

The aim to build a high acceptance particle detector for operation on board the International Space Station was accompanied by many restrictions and limitations. The transport

---

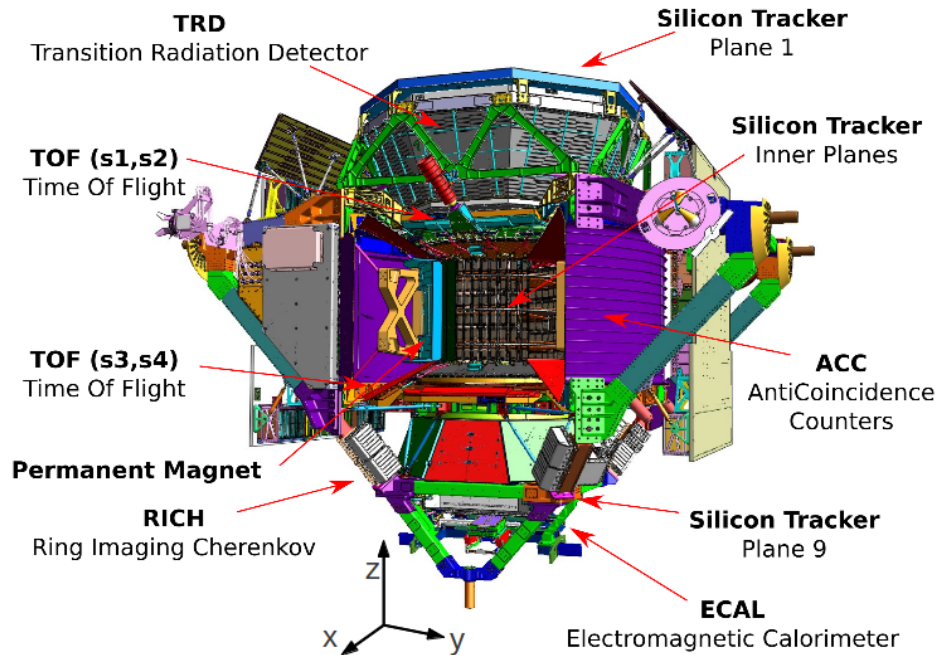[1]The operation of the ISS at the moment is confirmed until 2020.

Figure 3.1.: ***A model of the Alpha Magnetic Spectrometer with labelling of the subdetectors.*** AMS-02 measures particles traversing the detector from top (TRD) to bottom (ECAL). At the bottom the AMS coordinate system is indicated for further comparison. [20]

to the Space Station by a Space Shuttle limited the dimension and weight of the detector to its actual size of roughly 3 m in width and depth and 4 m in height and weight of 7 tons. The launch of a Space Shuttle produces forces of up to 3 g and high vibrations during lift-off, which the detector should be able to withstand.

In order to prove that the fragile silicon Tracker can survive such forces, a first version of the AMS detector, AMS-01, was taken into space as part of STS-91 mission in 1998. After the flight the detector layout underwent some changes including the addition of the Transition Radiation Detector. Being mounted on the ISS it had to be ensured beforehand that no impacts are made on the Space Station by the electronics. Therefore the complete system of AMS-02 was tested in the electromagnetic interference chamber at ESTEC[2]. The electromagnetic radiation emitted by the detector was checked as well as the impact of incoming radiation on the detector electronics. The operation of the detector in the ever changing temperature conditions of space demanded for specific electronics design and extensive testing of all components. The allowed power consumption of the system is strongly restricted, since it does not produce power itself, but obtains it from the Space Station. Therefore special low power consumption electronics needed to be designed and built for the detector. These also had to be vibration resistant to not be affected by the lift-

---

[2]ESTEC: European space research and technology center, Noordwijk, Netherlands

off in the Space Shuttle, radiation hard to withstand the impact of the cosmic radiation and to keep their full functionality after many thermal cycles. All subdetectors and electronics were tested in thermo-vacuum chambers to guarantee for proper functionality in space. The full detector was then tested at ESTEC and approved by NASA[3] for installation. In figure 3.2 AMS-02 is shown inside the Large Space Simulator at ESTEC and during a test beam at the Super-Proton-Synchrotron (SPS) at CERN[4] in 2010 [7].
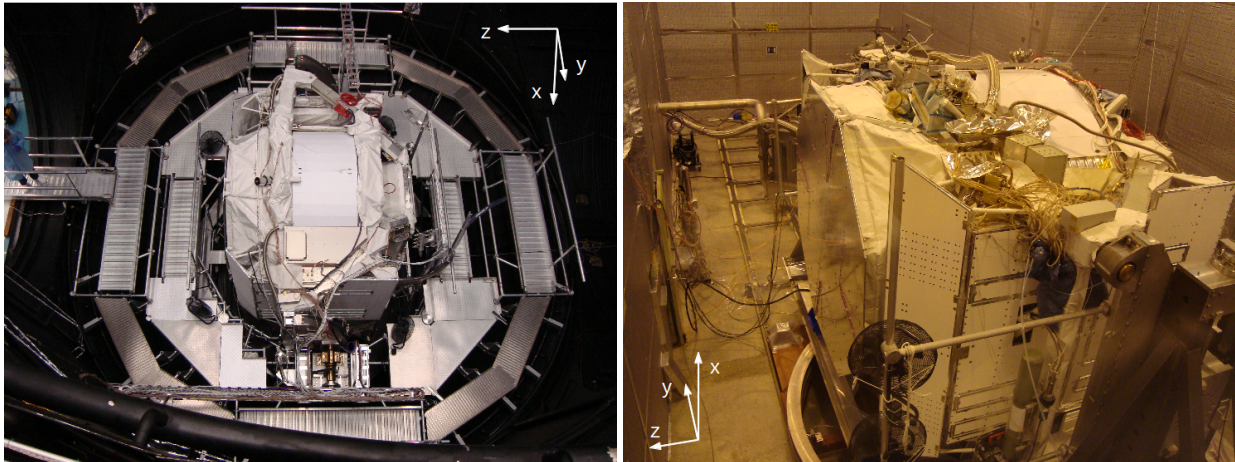
Figure 3.2.: **Testing of AMS-02.** Left: AMS-02 in the Large Space Simulator at ESTEC in March 2010, where the detector performance in vacuum under changing temperature conditions has been tested. Right: Beam Test at the Super Proton Synchrotron at CERN in February 2010. The particle beam entered the detector from the left side in this picture, passing through it along its z-axis. The AMS coordinates system is given to indicate the orientation of the detector.

After a test of its physics capabilities with the final detector assembly in a second beam test at the SPS, AMS-02 was transported to Kennedy Space Center (KSC) by the US air force inside a C5 aircraft. At KSC communications and mounting interfaces to Space Shuttle and Space Station were installed and last data acquisition tests were performed. AMS-02 finally lifted off on board Space Shuttle Endeavour as its last journey on May 16th 2011. Three days later the detector was installed on the mount point of the ISS and started taking data. AMS-02 in the cargo bay of Space Shuttle Endeavour and on its final position on the ISS can be seen in figure 3.3.

3.2. Subdetectors

Following the particles path through the detector from top to bottom, AMS-02 is build of a Transition Radiation Detector (TRD), which uses the effect of transition radiation to

---

[3]NASA: National Aeronautics and Space Administration.
[4]CERN: European center for nuclear research.

Figure 3.3.: ***AMS-02 in space.*** Left: AMS-02 in the cargo bay of Space Shuttle Endeavour on the way to the ISS, right: AMS-02 installed in its final location on the ISS. credit: NASA [121]

separate particles according to their mass. A Time-of-Flight detector (ToF) measures the velocity and direction of flight as well as the charge of the particles, in the same time serving as the trigger for the detector for charged particles. Mainly located inside the permanent magnet is the Tracker, which reconstructs the rigidity of the particles and the sign of their charge using the Lorentz force and at the same time determines their magnitude of charge. To avoid misreconstructed events and unnecessary dead-times due to recording of data that is not usable for particle identification, Anti-Coincidence-Counters (ACC) are located around the inner bore of the magnet vetoing the trigger signal if particles enter the detector from the sides. Below the magnet is a Ring Imaging CHerenkov detector (RICH), which measures the velocity and charge of the particle. Finally at the bottom of the detector is an Electromagnetic Calorimeter (ECAL), which allows to reconstruct the energy of electrons, positrons and photons from sampling their induced electromagnetic shower in the material. Protons and ions only deposit a fraction of their energy in the ECAL. Therefore their energy needs to be reconstructed from their rigidity measured in the Tracker. Having a Star Tracker also allows to identify the location of the source of the radiation using the tracking information of the particle inside the detector and the point of view of AMS-02 retrieved from the star map. From the combination of the measurements of these detectors, illustrated in figure 3.4, particle properties like sign and value of charge, energy, mass and momentum are reconstructed.

Measuring the charge of the particle multiple times along the passage through the detector enables to detect undesired fragmentation of ions into lighter nuclei, due to interactions with the detector material. It also allows to calibrate the subdetectors in a data driven way, by using the other subdetectors to tag the events. This redundancy is also exploited for tuning the discriminating variables of TRD and ECAL as explained in chapter 6. The subdetectors are described in more detail in the following sections.

Figure 3.4.: ***Particle identification with the AMS subdetectors.*** Comparison of the signals in the subdetectors originating from different particles with an energy of 300 GeV [121]. For photons the two different signatures of a photon converting in to a electron-positron pair in the TRD and a photon converting in the ECAL are shown. Explanations on the subdetector signatures are given in the corresponding subdetector sections.

3.2.1. The Transition Radiation Detector

The Transition Radiation Detector [122], shown in figure 3.5, provides the potential to distinguish particles according to their mass. Different particles with energies starting from a few GeV have similar momentum and velocities, thus to identify them correctly using these properties is complicated. The TRD uses transition radiation, where the intensity of the emitted photons depends on the Lorentz factor of the particles and therefore it depends on the different particle masses for particles of the same energy. As a result the TRD is one of the two main subdetectors responsible for the discrimination of light leptons from the highly abundant protons in the cosmic rays. The TRD is built of 20 layers, each consisting of radiator fleece and proportional chambers filled with a mixture of xenon and carbon dioxide. The gas in the straw tubes detects charged particles by ionisation, while at the same time the produced transition radiation is absorbed by using a high Z gas, in this case Xenon. The 12 central layers are rotated by 90° with respect to the upper and lower layers of the detector, which allows to use the TRD as a 3D tracking device.

In order to compensate diffusion losses of CO_2 molecules through the straw tube walls, the detector has a dynamic gas system, which allows for regular gas refills and ensures the long lifetime of the detector of about 30 years.

The data acquisition electronics of the TRD are the responsibility of the AMS KIT group, which developed and tested the electronics and set up the digital signal processing
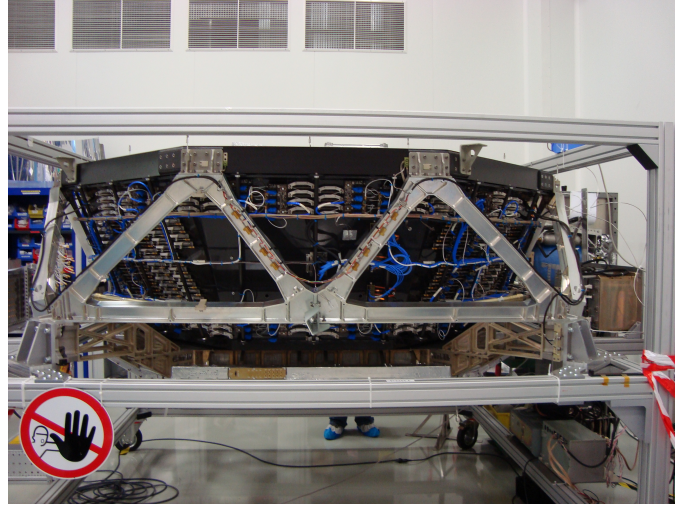
Figure 3.5.: **The Transition Radiation Detector.** The detector before the first assembly of AMS-02 in the clean room in October 2009.

(DSP) [123–126]. In the framework of this thesis the TRD has been calibrated and its particle discrimination has been improved. Therefore this subdetector is explained in detail in chapter 4.

The TRD signal in figure 3.4 is characterized by the drop in the applied voltage due to discharge caused by detection of transition radiation in the different layers. Protons of 300 GeV produce transition radiation with a low probability compared to electrons. The discrimination power, though, reduces above 300 GeV with increasing γ-factor of the proton.

3.2.2. The Time-of-Flight Detector

The Time-of-Flight detector [127], shown in figure 3.6, as its name is stating, measures the time the particles need to travel the distance between its different components. Therefore it measures their velocity and provides the information if the particles crossed the detector from top to bottom or vice versa. The detector is build of two main components, the upper ToF on top of the magnet and the lower ToF underneath the magnet. Both ToF parts consist of two layers of scintillation ladders, which are assembled 90° rotated to each other. The scintillation counters work as a stop watch using Time-to-Digital-Converters (TDC). A passing particle excites the molecules in the scintillating material, which then drop back to their ground state by fast emission ($t = 10^{-8}$ s) of characteristic fluorescent light. This light is guided by light-guides to photomultiplier (PMTs) where a electric signal is generated that starts or stops the TDCs. This way the pass-through time is measured with an accuracy of 160 ps for unitary charged particles, which allows to measure the speed of these particles with a precision of 4% of the speed of light. For charges Z>5 the hardware limit is reached at a $\Delta t \sim 50 ps$ and $\Delta\beta \sim 1\%$. The timing of the single ToF layer signals

Figure 3.6.: ***The upper and lower part of the Time-of-Flight detector before in-
tegration.*** The velocity of the particle is measured by the difference of the
time measurement of the single layers. [121]

give the direction of passage of the particle from top to bottom or vice versa. This makes
it possible to identify the sign of charge of the particles by determining the curvature of the
tracks in the magnetic field with the Tracker. The ionization in the scintillation ladders is
proportional to the magnitude of charge of the incoming particle. Hence the charge can be
reconstructed from the ToF signals. This is represented in figure 3.4 as the size of the drop
of the applied voltage induced by the particle detection, whereas photons only give a signal
in the ToF, if they converted into electrons and positrons before entering the detector.

With its sensitive measurement capabilities and its accurate time measurement the ToF
is also used as the main trigger for AMS-02 for charged particles. A trigger pulse is
initiated in case of a simultaneous signal in all 4 layers of the ToF, corresponding to a
charged particle crossing the instrument vertically.

3.2.3. The Anti-Coincidence Counter

The Anti-Coincidence-Counter [128] is a cylindrical assembly of 16 scintillating bands with
interleaving edges around the inner side of the magnet. The scintillation light is collected
in wavelength shifters and by light-guides carried to eight PMTs. The ACC bands give a
signal, if a particle crosses the walls of the magnet and therefore enters or exits the Tracker
from the side. To uniquely identify particles all detector components should be traversed,
consequently particles coming from the side are not used for analysis. In addition these
kind of particles create signals in the Tracker, which might lead to a wrong identification
of the particle giving the trigger of the event. To be able to measure particles for analysis
with a high rate and in a clean way, the signal of the ACC is used as a veto to the trigger.
There are two situations were the veto is suppressed and the event is recorded, see figure

3.7. One of them is a particle with a nuclear charge greater than one, which is recognized by a higher deposited energy in the ToF, because they emit delta electrons, which might lead to signals in the ACC. The other one is for events where also the electromagnetic trigger is issued, because high energy electrons or positrons can create back-splash electrons when entering the ECAL, which might also create signals in the ACC.
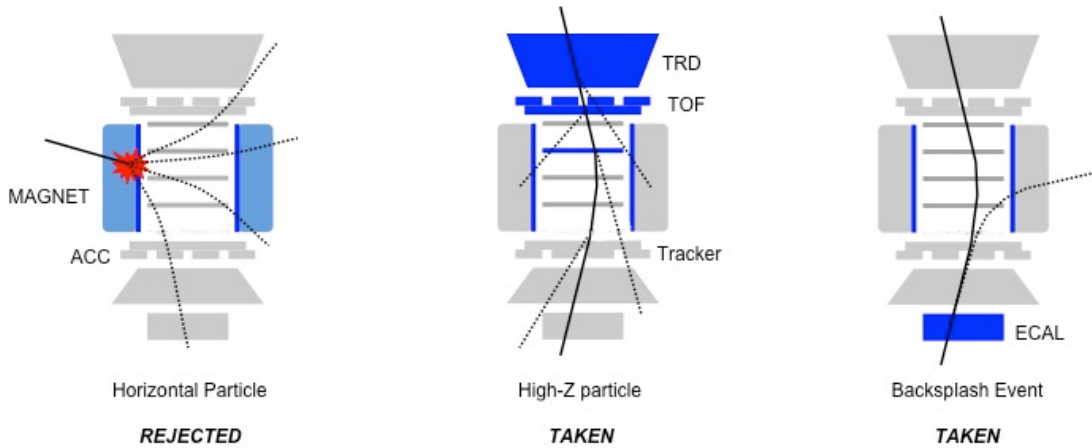
Figure 3.7.: ***Exceptions of the ACC veto to the trigger.*** For charged particles with Z>1 and particles initiating the ECAL trigger the ACC veto is suppressed. [121]

3.2.4. The Tracker

The central detector of AMS-02 is the silicon Tracker [129], shown in figure 3.8, whose inner part is located inside a permanent magnet. The magnet is made out of 64 high-grade ND-Fe-B sectors, which are assembled cylindrically having an inner shell diameter of 1.1 m, and yields a homogeneous magnetic field inside the magnet of 0.15 Tesla aligned with the x-axis of the AMS coordinate system, making the particles bend in the y-z-plane. The magnetic field outside the magnet bore is effectively zero, which had to be ensured to not exercise a torsional moment on the Space Station caused by the interplay with Earth's magnetic field. The Tracker measures the rigidity[5] and distinguishes between positive and negative charged particles. It is made out of nine layers of silicon strip sensors. Six of these are inside the magnet, with layer three and four, layer five and six, layer seven and eight mounted to the same support plane each. Layer two is mounted on a support plane just above the magnetic field. Another Tracker layer is located on the very top of the detector above the TRD called plane 1, the last one, referred to as plane 9, is situated below the main part between the RICH and the ECAL. The outer layers improve the rigidity resolution of the Tracker by enlarging the lever arm for the determination of the entry and exit angle of the particle.

---

[5]The rigidity of a particle is defined as its momentum per elementary charge.
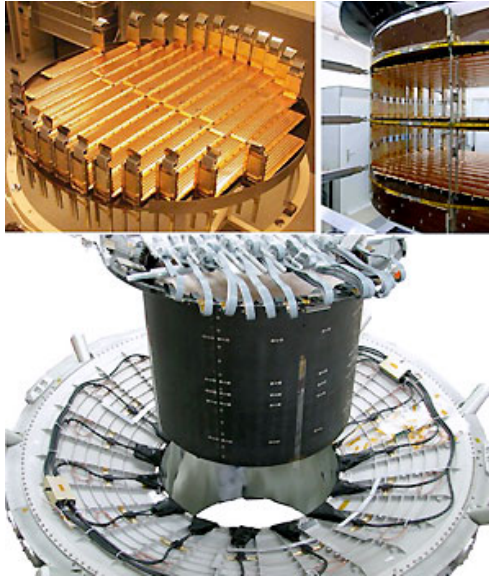
Figure 3.8.: **The Tracker.** In the top left picture one Tracker layer mounted on its support structure is shown. The top right picture shows the support structure of the inner tracker planes. In the lower figure the lowering of the inner Tracker into the magnet bore is pictured. [121]

The highly doped silicon is 300 μm thick and coated on top and bottom with fine Aluminium strips, which are arranged orthogonally to allow a measurement in both x and y coordinate. The inevitable leakage current of the Tracker sensor, which are read out by 200000 electronic channels, produces a lot of heat. In space this heat cannot be dissipated by air cooling, as a consequence the Tracker has its own special cooling system (TTCS) [130]. This system consists of a high pressure CO_2 circuit, which absorbs the heat of the Tracker by changing the state of the CO_2 from liquid to gaseous. The gas then transports the heat to the radiators, where the heat is removed and the CO_2 condenses again. By the TTCS the temperature in the inner Tracker is kept stable within 1° C.

A charged particle crossing the silicon creates electron-hole pairs, which drift in opposite directions to the respective contacts on the surface within 10 ns. The read-out strips close to the particle crossing detect a signal, using the center of gravity method a resolution of the particle path of 10 μm is achieved. The deposited energy of the particle is proportional to the square of the charge of the particle:

$$\sum I_{signal} \propto q^2 \ . \tag{3.1}$$

The Tracker therefore has a good charge resolution and can identify ions up to iron. Inside the magnetic field (B), the charged particles experience the Lorentz-force, which leads to a curvature of their path in the y-direction:

$$\vec{F} = q(\vec{v} \times \vec{B}) \ . \tag{3.2}$$

From the signal of the different layers the curvature $\rho = 1/r$ of the track is reconstructed by fitting the arc of a circle to the signals of the inner Tracker. The two outer layers with their distance to the center of the detector have a large lever arm for measuring the particles incoming and outgoing direction to the magnetic field and therefore allow the measurement of minute bending of the track. The curvature in combination with the magnetic field strength gives the rigidity R as $R = Br$, which is a measure for the momentum of the particle divided by its charge.

The direction of the bending gives the sign of the charge of the particle, as illustrated in figure 3.4, where the line thickness represents the stated sensitivity to the magnitude of the charge. The sign of the charge is one of the few particle properties which is measured by one detector only. The measurement is important because the misreconstruction of the sign of the charge of the particles introduces a background of electrons in the measurement of positrons. With increasing energy the curvature of the particle track becomes smaller and smaller, making it harder to determine it correctly. The maximum detectable rigidity (MDR) is defined as the rigidity for which the uncertainty of reconstruction is just as big as the reconstructed value itself. For AMS-02 the MDR is 2.2 TeV, which is the highest of all space spectrometers ever built.

3.2.5. The Ring Imaging Cherenkov Detector

The Ring Imaging Cherenkov detector [131] measures the velocity and magnitude of charge of the particles. It is composed of an entry layer of radiator material, a conical mirror and the measuring layer to detect the radiated photons; the components are shown in picture 3.9.

Cherenkov light is emitted by particles inside a material with a velocity greater than the speed of light in that medium. The light is emitted in a cone with an opening angle θ depending on the velocity $\beta = v/c$ of the particle and the refractive index n of the material it is produced in:

$$cos(\theta) = \frac{1}{n\beta} \ .$$
(3.3)

The outer area of the radiator is made of aerogel with a refractive index n of 1.03 to 1.05 and the central area is made of sodium fluoride ($n_{NaF} = 1,335$). The mirror is mounted on a carbon structure and has a height of 47 cm. The Cherenkov-light is detected by a layer of 680 multi-anode photomultiplier, which cover a radial area of 137 cm in diameter. The central area, under which the electromagnetic calorimeter is located, is not occupied by PMTs to not introduce any bias in the following energy measurement. The specific choice and layout of radiator material nevertheless allows to also measure particles coming into the central region, because the high refractive index of the NaF makes the light emerge with a bigger angle so that it will reach the surrounding photomultiplier, as is illustrated in the right of figure 3.9. The pattern recognition algorithm reconstructs β with an accuracy of 0.1% for unity charged particles and 0.01 % for ions. The charge of the particle can be determined from the number of produced photons with an accuracy of about 10%. The good resolution of the velocity β together with the reconstructed rigidity R given by the
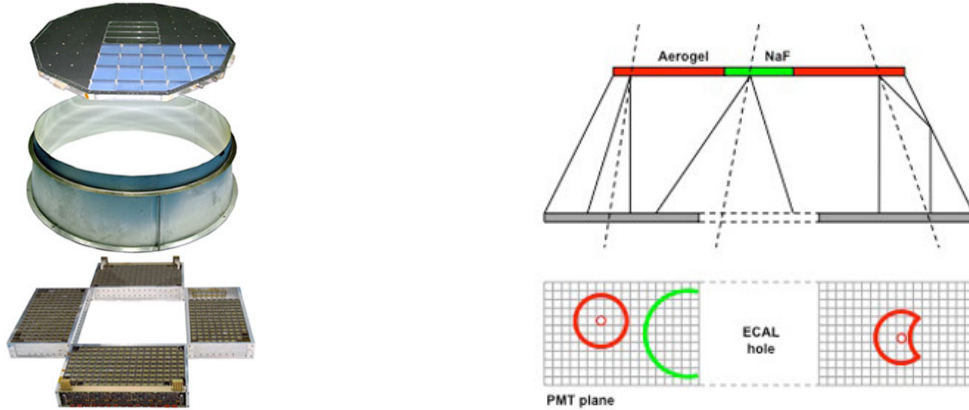
Figure 3.9.: **The AMS-02 RICH.** On the left the constituents of the RICH before assembly are shown. The top part is the radiator layer, with a change in structure in the middle, where the radiator material changes from aerogel to NaF. Beneath the radiator the conical mirror is shown, which reflects the photons that are emitted with a too large angle to reach the detection layer. At the bottom a preassembly of the PMT layer with the whole for the ECAL is shown. On the right is a demonstration of possible signals in the detector. [121]

Tracker and the redundantly determined magnitude of charge Z also allow to give the mass of the particle from the equality of centripetal and Lorentz force in the magnetic field [132]:

$$m = RZ\frac{\sqrt{1 - \beta^2}}{\beta c}. \tag{3.4}$$

The properties of the RICH signal, being the diameter of the ring indicating the velocity of the particle and the number of emitted photons being proportional to the magnitude of charge of the particle, are depicted for different particle species in figure 3.4. The difference in angle for electrons and protons of 300 GeV is largely exaggerated in this figure, as the RICH can only distinguish these particles well below 100 GeV.

3.2.6. The Electromagnetic Calorimeter

The Electromagnetic Calorimeter [133], as shown in figure 3.10, is the last detector passed by down-going particles. It distinguishes between hadrons and leptons due to their different interactions with lead. The ECAL is build of nine 18.5 mm thick superlayers, which each consist of 11 layers of 1 mm thick lead with cut-outs for scintillating fibres of equal size. The superlayers are assembled alternating in parallel orientation to x- or y-axis of the AMS coordinate system.

Photons and light leptons mainly interact based on the electromagnetic force and therefore create an electromagnetic shower dominated by bremsstrahlung and pair-production
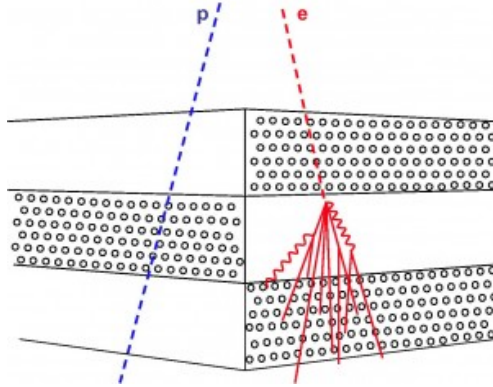
Figure 3.10.: ***A scheme of 3 superlayers of the AMS-02 calorimeter.*** The channels of the superlayers are alternating in measuring x- or y-coordinate of the energy deposit. The different behaviour of protons and electrons in the material are sketched. For simplification only 6 instead of 11 layers are depicted per superlayer. [121]

processes. The shower ends, when the secondary particles have reached the critical energy of the absorber, or by leaking out of the detection volume. For particles of this category with energies below 1 TeV and in the central part of the detector the whole shower is contained and so the measured signal is directly proportional to the energy of the primary particle.

A hadron interacts according to the strong force and therefore creates a different signal in the calorimeter. The created shower is called a hadronic shower; it is the result of interactions by secondary particles like pions or kaons. The created showers are wider spread and more irregular than electromagnetic ones. The nuclear interaction length, the mean path length required to reduce the number of relativistic charged particles by a factor of 1/e as they pass through matter, exceeds the radiation length of photons and leptons by an order of magnitude. As a consequence and taking the ECAL size into account only about every second hadron will create a hadronic shower in the calorimeter, the others traverse the ECAL only depositing energy by ionisation.

The different signatures of leptons and hadrons in the calorimeter are illustrated in figure 3.4. Electromagnetic showers are represented as a bundle of lines, while the signal of hadrons in this illustration is characterized by only ionization signals in the single ECAL layers, where the amplitude of the signal depends on the magnitude of charge of the traversing particle. The nature of the particle can be derived from the shower profile, and for leptons, the energy can be measured. The ECAL lepton energy resolution is parametrized as a function of energy [133]

$$\frac{\sigma(E)}{E} = \frac{10.4\%}{\sqrt{E(GeV)}} + 1.4\%. \tag{3.5}$$

With this high resolution the ECAL energy is the controlling energy parameter for

a lepton analysis. From the reconstruction of the shower axis also the direction of the incoming particle can be obtained. This is an important feature for gamma astronomy.

3.3. Particle identification

To unmistakeably identify particles the magnitude and sign of their charge as well as mass needs to be known. AMS-02 is measuring the magnitude of charge of the particles redundantly. TRD, Tracker, ToF and ECAL can give a charge estimation via the energy deposit due to ionisation. RICH measures the magnitude of the charge by the numbers of photons detected. Due to these multiple measurements this particle property is reconstructed well. The measurement of the magnitude of charge along the passage of the particle through the detector also allows to detect conversion of ions or interactions of the primary particle. The sign of the charge is reconstructed from the Tracker measurements, comparing the results of the reconstruction using the signals in different parts of the Tracker allows for cross-checks. Therefore a confident reconstruction of the sign of charge is possible up to TeV energies depending on the Tracker signal span, which refers to the number of layers used in the track reconstruction. The mass of the particle can be calculated from the measurement of the momentum or energy of the particle and its velocity. For unity charged particles the resolution of the velocity measurement is not good enough to reconstruct the mass well. The TRD though, is distinguishing the particles according to their gamma factor and knowing their energy this gives an estimation of their mass. In addition the shower shape in the ECAL hints at the lepton or hadron nature of the incident particle. The combination of the subdetector measurements delivers all necessary information to distinctly identify the particle and to reconstruct its energy. Consequently the desired particle spectra versus energy can be constructed.

3.4. Data acquisition

Charged particles crossing both parts of the Time-of-Flight system as well as particles producing a shower in the calorimeter initiate a trigger for the system. A signal is then send to the subdetectors to record their current measurement. The data reduction boards (xDR) of each subdetector assign event numbers to the recorded data, apply a zero suppression algorithm to reduce the amount of data and save it in their buffer, which can hold up to 4 events. The data of all associated xDRs belonging to the same event is collected by the interface boards (JINF-x) of the subdetectors and passed to the higher level interface board (JINJ) which is responsible for the communication between subdetectors and the main computer (JMDC). The JINJ collects the data of all subdetector electronics and passes the event data to the JMDC for recording. This process is illustrated in figure 3.11.

The same data flow as used for science data recording is used to collect status information of the detector and its electronics, which is called housekeeping data. This includes temperatures and check sequences of the electronics, as CR particles can lead to bit flips on
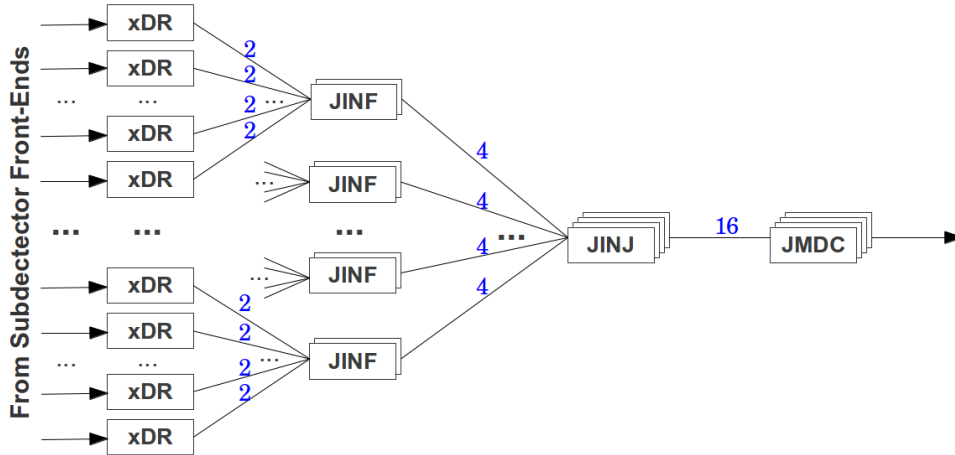
Figure 3.11.: **The AMS data acquisition system.** The different levels of the AMS-02 electronic system and their redundancy are shown. Because of its location on the ISS a repair or exchange of electronic parts is impossible. Therefore the system was designed in a maximal redundant way so that a failure of a cable or board does not impact the performance of the detector. The main computers therefore have a redundancy of four, while the subdetector level electronics are redundant by a factor of two, with exception of the Tracker xDRs and RICH xDRs, which could not be built redundantly due to the high number of electronic channels and limited amount of electronic boxes.

the electronic boards. The housekeeping data is collected in such a way that the influence on the science data taking is minimal.

The JMDC buffers all data to ensure no data gets lost during communication loss of the Space Station to ground. The data is send out via several streams; the buffer playback is divided in housekeeping and science data streams. At the same time as the housekeeping data is going into the buffer a copy is send out in a low rate link to the Payload Operations Control Center (POCC), which is located at CERN, to enable near real time monitoring of the status of the detector, whenever satellite connection is available. Whereas the data received on ground from the buffer playback of the JMDC can be several hours old due to limited downlink bandwidth or loss of satellite connection. Because of the high event rates in space between 200 Hz up to 2 kHz in regions of low Earth magnetic field and an average event size of 2 kByte a large amount of the data needs to be linked down to ground. With a data acquisition efficiency of about 86%[6] and a resulting average trigger rate of 600 Hz the downlink rate is about 10 Mbit/s on average.

---

[6]$\epsilon(DAQ) < 1$ is due to detector dead-time in high trigger rate regions, for example near the geomagnetic poles.

3.5. Operation of AMS-02

AMS-02 is installed on the ISS orbiting the earth at an altitude between 330 km to 410 km. Its orbit plane has an inclination of 51.6 degrees to the Earth's equator and completes 15.7 orbits per day. Figure 3.12 shows the frequentness of the occurrence of good[7] recorded events according to the location of the detector in geodetic coordinates as well as the average recorded rigidity of the events detected in the different locations. The empty spot in the figures is caused by the South Atlantic Anomaly (SAA). The SAA [134] is the caused by the tilt between Earth's rotational axis and its magnetic field axis. In this location the ISS orbit crosses the inner Van-Allen belt, in which low energetic particles are trapped, which leads to a high particle flux making it impossible to reconstruct single particles in the detector.
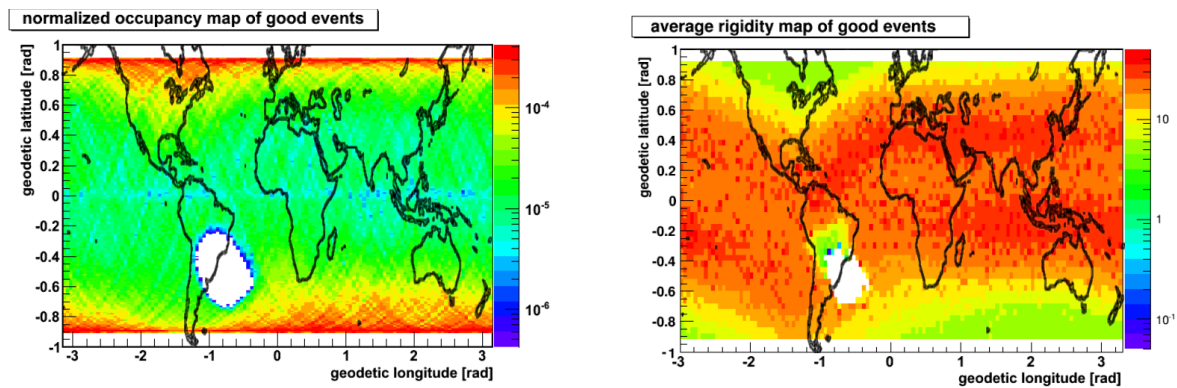
Figure 3.12.: ***Normalized occupancy and average rigidity maps.*** Left: occupancy map of recorded events according to geodetic coordinates of the detector normalized to number of all events. Right: map of the average rigidity of recorded particles fulfilling minimal quality criteria[7]. The empty spot in both figures is caused by the SAA.

On board of the ISS a laptop fully dedicated to AMS-02 has been installed. The crew can communicate via the laptop to AMS-02 in case of emergencies, for example a necessary reboot in case of communication failure to the AMS-02 main computer from ground. It is also recording the data during long losses of signal to the satellites that are responsible for communication between the ISS and ground. The nominal communication and operation of the detector is executed from the POCC. Sending commands and retrieving data from the detector is done using the NASA communication channels through Marshall Space Flight Center.

The recorded science data, which refers to the triggered events, is arranged in runs of 23 minutes each. Before every other run a calibration of the electronics is performed. This is done in coincidence with the equator crossing of the ISS, because the cosmic ray flux in this region is lower than at the poles. For the calibration the electronics signal is

---

[7]This refers to the preselection criteria further described in the analysis chapter 7.

measured without energy deposit in the detectors in order to determine the pedestal value and noise of each channel. A high particle flux might distort this procedure, if not enough measurements without particles crossing can be performed in the predefined time. More detailed information about the TRD electronics calibration can be found in section 4.4. High energy particles can have some effect on the electronic boards of AMS-02. A particle depositing its energy on one of the boards can lead to a bit flip. To ensure that the data is not corrupted, once per orbit the digital signal processing (DSP) code of the electronics is tested and in case of a detected error it is restored to normal. In addition at the beginning and end of each data run as well as at regular time intervals certain read-out commands are send to check the status of the detector electronics and to read out the temperature sensors distributed over the whole detector.

All the collected status data as well as some information of the current recorded science data are monitored at nearly real time in the POCC. The collected information is being monitored at five consoles in three eight-hour shifts per day:

- Lead: responsible for the data acquisition (DAQ) and the detector operation and commanding, in close contact to NASA

- Data: monitoring the data flow from and to the detector

- Temperature: monitoring the temperature sensors of all systems

- PMT: monitoring RICH, ToF and ECAL

- TT: monitoring TRD, Tracker and ACC

As part of this thesis a tool, which is used by the lead position to monitor the size of the recorded events in each subdetector and of the combination of them in the JINJ board, has been developed and adjusted to the latest procedures of detector operations [135]. In preparation for the flight of AMS-02 and since its operation on the ISS monitoring and operation shifts were done on regular basis as part of this thesis.

4. The Transition Radiation Detector

The Transition Radiation Detector is one of the two subdetectors of AMS-02 whose main purpose is to discriminate protons from positrons in the cosmic rays. It differentiates particles of the same energy by their γ-factor and therefore according to their rest mass. High energy particles of the same magnitude of charge, having a velocity close to the speed of light ($\beta \sim 1$) leave the same signature in the Tracker, ToF and RICH. The difference in the mass of a positron with 511 keV/c^2 and a proton with 938 Mev/c^2 is too small to be detected in a different momentum by the Tracker or different β by ToF or RICH. The ECAL distinguishes between the two particle species, but its discrimination power is not sufficient to clearly identify positrons in the cosmic rays, where the protons flux is about three orders of magnitude higher than the positron flux, see figure 2.3. Therefore it was necessary to introduce an additional detector type with a strong power to discriminate between protons and positrons to the system, in this case a Transition Radiation Detector. The TRD uses the effect of transition radiation, which only occurs for particles with a high γ-factor, by which it is able to clearly separate these two particle species up to energies of many hundreds of GeV. Above these energies its discriminating power reduces due to the increasing γ-factor of the protons.

The positron to electron ratio is one of the important measurements in the search for dark matter,. Therefore a good positron identification is of highest interest, which makes the TRD a important subsystem of AMS-02.

The physic principles of transition radiation are explained in the first section. The TRD layout will be described in the second section, followed by a description of the TRD gas system and the data acquisition electronics and data acquisition procedure of the detector in sections three and four, respectively. In section five the operation of the TRD on board the International Space Station is outlined. Finally the necessary calibrations of the detector due to its operation in the ever changing conditions in space are presented. The latter include the time dependent gas gain calibration needed for a stable detector response and a time dependent detector alignment with respect to the AMS-02 Tracker.

4.1. Transition radiation

The discrimination power of the TRD origins from the phenomena of transition radiation. Transition radiation is emitted, when a charged particle with a high γ-factor passes the interface of two materials with different dielectric constants. The solution to the Maxwell equations of a particle in the two media is different; the emitted radiation accounts for this difference. A more figurative explanation is found in the changing electric dipole that the

particle is creating by approaching its image charge in the other material [136], illustrated in figure 4.1.
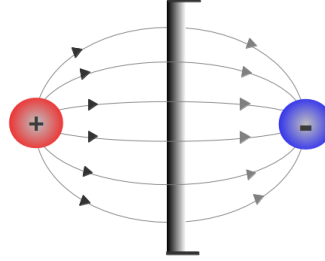
Figure 4.1.: *A dipole created by a charge and its image charge.* The charged particle approaching the interface gives rise to a change in the dipole, which leads to the emission of transition radiation.

The emitted photons typically have x-ray energies between 5 keV and 15 keV. The intensity of transition radiation of a charged particle passing the border between two media with different dielectric constants is given by [137]:

$$I = \frac{\gamma \, q^2 \, (\omega_{p_1} - \omega_{p_2})^2}{3c} \tag{4.1}$$

with

$\gamma = \frac{E}{mc^2}$: Lorentz factor of the particle
$\omega_{p_1}, \omega_{p_2}$: plasma frequencies of the media
q : charge of the particle
c : speed of light.

It is directly proportional to the particles γ-factor and therefore mass dependent for particles of the same energy, this dependency is shown in 4.2. An electron of a few GeV energy has a Lorentz-factor ~ 2000 higher than a proton of the same energy. The difference in probability for the emission of transition radiation is used to separate these two particles. The maximum of the emission is radiated under the angle $\theta = 1/\gamma$ [132]. For high energies this means emission in forward direction in coincidence with the producing particle.

The discrimination power of transition radiation reduces, when the γ-factor of protons exceeds 300, as the probability for emission of transition radiation increases rapidly from this point, as can be seen from the right plot in figure 4.2.

4.2. Design of the TRD

The TRD [138] is located at the top of the instrument. It has an octagonal pyramidal shape in order to optimize its angle of incidence versus its mass and size. It is about
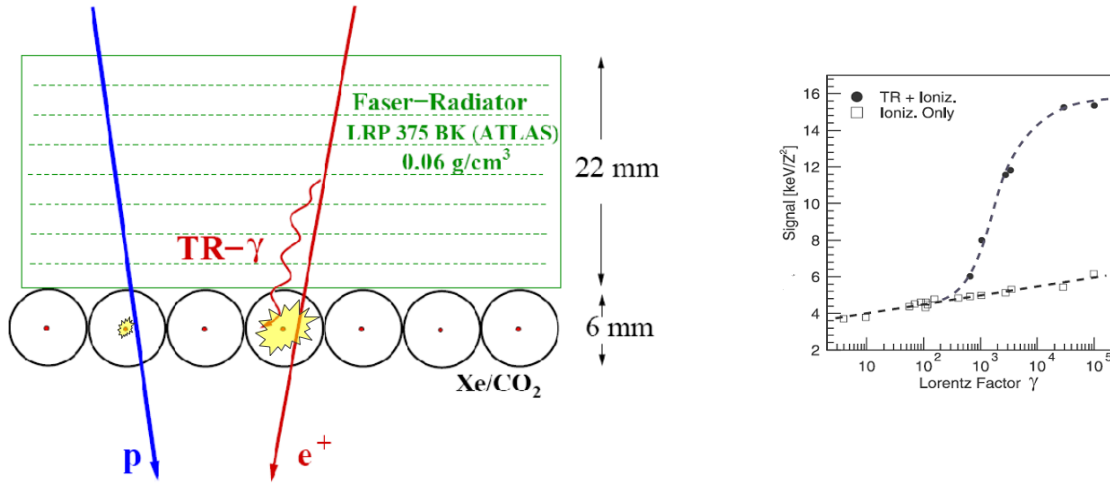
Figure 4.2.: ***The signal in the TRD with contribution of ionisation and possibly transition radiation.*** Left: a scheme of a TRD layer with fleece radiator and proportional tubes. Electrons emit transition radiation which is detected by the straw tubes together with their ionisation signal. Right: TRD signal dependence on the particles γ-factor. The contribution of transition radiation is much larger than the ionisation which ensures a good separation of the two contributions. [121]

80 cm high and spans 220 cm wide at the top layer and 150 cm wide at the bottom layer. A model can be seen in figure 4.3.

This subdetector is built up out of 5248 proportional chambers with a diameter of 6 mm and changing length according to the location in the TRD ranging from 0.8 m to 2 m. Always 16 tubes are assembled together in a module as can be seen in figure 4.4, with six stiffeners between the tubes and every 10 cm along the tubes.

The modules are arranged in 20 vertical layers with 22 mm of radiator fleece, made of polypropylene and polyethylene, between each layer. The numeration of the layers is starting with the lowest layer as layer 0 increasing to the uppermost layer labelled as layer 19. The fleece together with the vacuum in space provides a high number of material transitions in order to increase the probability of emission of transition radiation for highly relativistic particles from $\sim \alpha$ [1] per transition [132] to about 60% for emission and absorption per TRD layer [139]. A thickness of 22 mm of the radiator fleece has proven to be optimal for the emission and detection; it provides a high number of transitions while not absorbing all of the produced transition radiation again before the x-rays can reach the detection tube. The walls of the straw tubes are made of multiple layers including a graphite layer, which is grounded and functions as the cathode of the proportional chamber. The anode is a fine gold plated wire in the middle of the tube. The straws are operated

---

[1]$\alpha = 1/137$: fine structure constant.
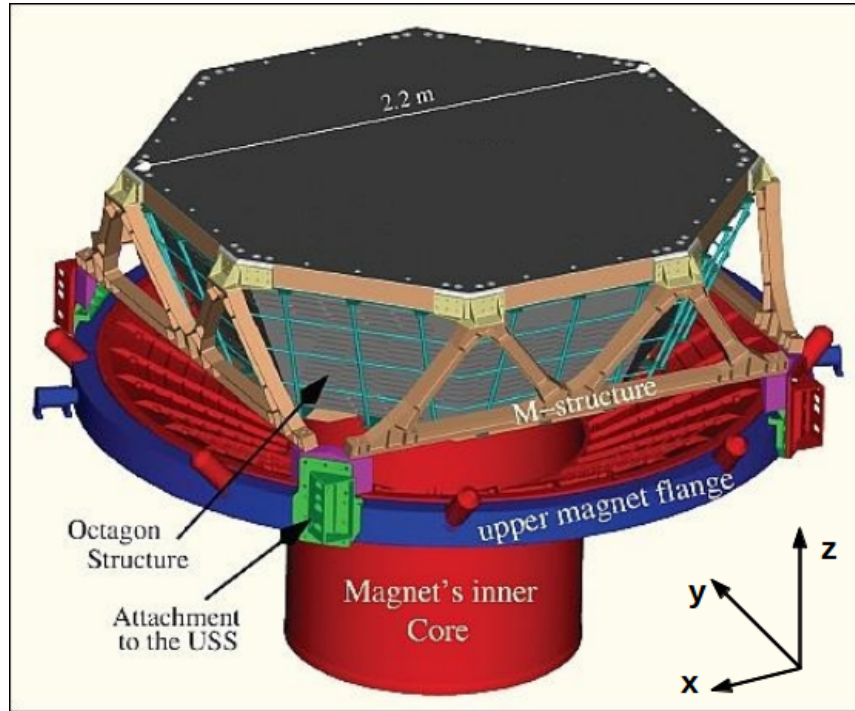
Figure 4.3.: **The AMS-02 TRD model.** In brown the so called M-structure can be seen, which is supporting the TRD and is fixed to the magnet case. In the same location the detector is attached to the unique support structure (USS), by which AMS-02 is mounted to the ISS. [20]

at a high voltage of about 1500 V. All tubes of one so called tower, built of 4 modules arranged on top of each other, are connected to the same high voltage channel.

The straw tubes in the four highest and four lowest layers of the TRD are mounted parallel to the x-axis of the AMS coordinate system, the straw tubes in the middle layers are parallel to the y-axis. This allows a three dimensional reconstruction of the particle path. The spatial resolution of the track is rather poor though with a resolution of the single points of approximately $\frac{6mm}{\sqrt{12}}$, where the factor $1/\sqrt{12}$ arises from the assumption of a flat probability distribution within the tube [140]. The efficiency of each of the 20 detector layers to detect a passing charged particle is $\sim 95\%$, which corresponds to the active material in the layer.

The straw tubes are filled with a mixture of xenon and carbon dioxide. The xenon is being ionised by charged particles traversing the straw tubes. The released electrons are accelerated towards the anode wire and close to the wire, where the electric field is stronger, they initiate a electron avalanche. The charge measured at the anode is proportional to the number of initially ionized gas atoms and independent of the distance to the wire of the particle crossing. The collected charge is stored at a capacitor and transformed into a digital signal by the front end electronics.
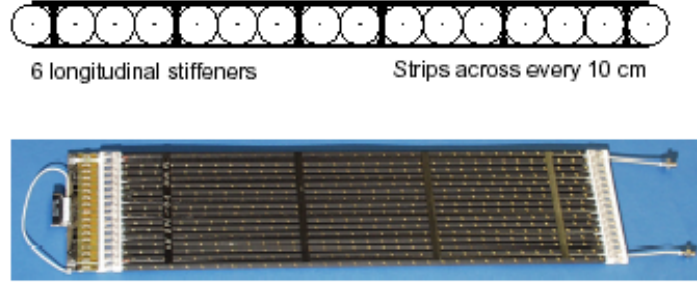
Figure 4.4.: ***The TRD straw tubes.*** A TRD test module consisting of 16 straw tubes. Top: profile showing 6 longitudinal stiffeners between the tubes, bottom: overhead shot showing support strips every 10 cm along the tubes.

The deposited energy by ionisation dE per distance dx travelled through the medium is given by the Bethe-Bloch formula [141]:

$$-\frac{dE}{dx} = \frac{N_A e^4}{8\pi m_e c^2} \cdot \frac{Z z^2}{A} \cdot \frac{\rho}{\beta^2} \cdot \left[ln \left(\frac{2 m_e \beta^2 \gamma^2 T_{max}}{I^2} - 2\beta^2 - \delta\left(\beta\right) \right) \right] \tag{4.2}$$

with:

e,m_e: charge and mass of an electron
N_A: Avogadro number
Z, A: atomic number and mass number of the detection material
z: charge of the ionizing particle
ρ: density of the detection material
$\beta = \frac{v}{c}$: relative velocity
$\gamma = \frac{E}{mc^2}$: Lorentz factor
I: mean ionisation
T_{max}: maximum energy deposit
$\delta\left(\beta\right)$: density correction.

The deposited energy by ionisation is detected for all charged particles. For high relativistic particles the additional transition radiation contributes to the signal. Due to the forward emission of the transition radiation photons it is mostly detected in the same straw.

For the decrease in intensity due to absorption of the photons in material we have:

$$I = I_0 \, exp(-\mu x) \tag{4.3}$$

with μ being the absorption coefficient and x the thickness of the material.

Transition radiation photons of keV energies are mostly absorbed by the photoelectric effect, see figure 4.5, where the photon passes all its energy to a bound electron, releasing the electron with an energy $E_{kinetic} = E_{photon} - E_{binding}$. The electron then is detected by
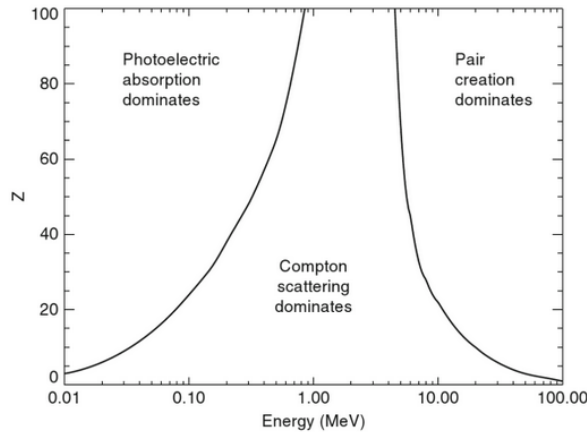
Figure 4.5.: ***Interaction process of photons with matter.*** The dominating effect in photon interactions according to photon energy and nuclear charge of the absorber is displayed. For the transition radiation photon of keV energies and xenon as absorber with $Z = 54$ the photoelectric effect dominates the photon interactions. [142]

ionisation. The cross-section α of the photoelectric effect strongly depends on the atomic number of the detection material, namely $\alpha \propto Z^5$. Xenon ($Z = 54$) has a high cross-section which leads to a high absorption probability. The absorption coefficient is the highest if the energy of the photon nearly equals the binding energy of an electron. For xenon x-ray energies correspond to binding energies of electrons in the inner shells.

4.3. Gas system

The straw tubes of the TRD are filled with about ten litres of a mixture of xenon and CO_2 at a ratio $\sim 90/10$. This corresponds to an operation of the TRD at a pressure of just below one bar. Xenon with its high atomic number and specific ionisation energies is suitable to detect the ionisation signal of crossing charged particles as well as detecting the low energy photons of the transition radiation. The carbon dioxide acts as a quenching gas for gas ionisation. It absorbs the energy of free electrons by transitioning into higher states of vibration instead of being ionized like xenon. Therefore it disrupts the charge multiplication at a certain level and ensures that the gas gets back to its initial state for the next measurement.

In the vacuum of space gas is continuously diffusing out of the straw tubes. The loss of CO_2 is larger than the loss of xenon, because the CO_2 molecules are smaller and can traverse the wall of the tubes more easily than the xenon atoms. As a result the supply of CO_2 on board AMS-02 is the limiting factor for the operational time of the transition radiation detector as long as the detector has no significant leak.

The gas system, as illustrated in figure 4.6, was equipped with a storage of 49 kg of CO_2 and 5 kg of xenon prior to the launch of the detector. It consists of a mixing system for
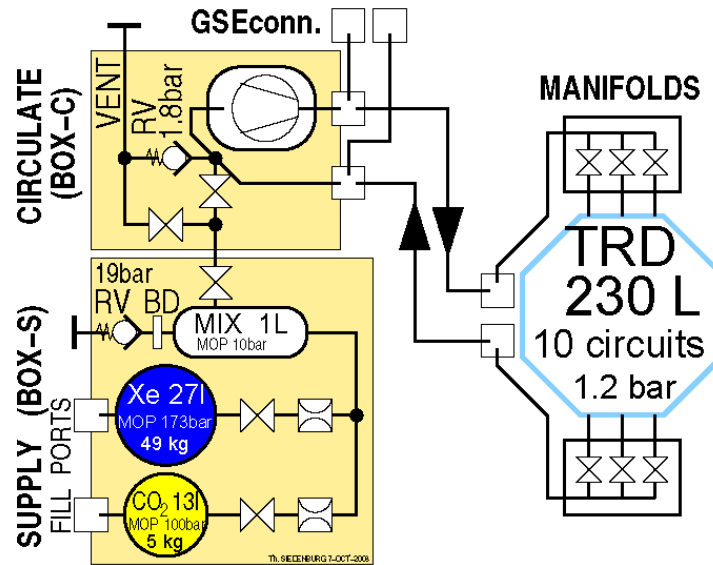
Figure 4.6.: **The TRD gas system.** The TRD gas system consists of two gas supply tanks, the Supply Box (Box-S), where the gas is transferred from the gas vessels into the mixing volume, the Circulation Box (Box-C), which is responsible for transferring the premixed gas into the detector and circulating it through the whole volume of the TRD [121].

the gas to be filled into the TRD straw tubes, a pump to circulate the gas through the detector as well as a network of pressure and temperature sensors to monitor the status of the detector and gas system. Most of the gas system is build in a redundant way, e.g. there are two pumps to have a spare one in case of failure of the primary. Assuming the current operation of the TRD to be kept the same in the future, the gas supply of the TRD would last for another 30 years of operation.

The straw tubes of the TRD are arranged in 41 gas circuits each consisting of two neighbouring towers of 64 tubes. Four or five of these circuits are connected to the same manifold, which in case of leakage by one of the connected tubes could be closed in order to not affect the rest of the detector. To keep the best performance in case one of the manifolds needs to be closed, the gas circuits connected to one manifold are spread over the volume of the detector in such a way that the acceptance of the detector is least affected. The UG-crate, an electronics box to control and monitor the TRD gas system, is responsible for commanding and read-out of the gas system. It regularly provides the pressure and temperature information of the TRD and has an automatic emergency task running. This task checks the vital information of the detector like the total pressure of the system, the differential pressure of inlet and outlet of the single manifolds and the pressure in the gas supplies. In case the task finds a serious problem, it sends predefined control commands to try to save the system. This is necessary, because communication between the detector and ground control is not always ensured.

4.4. Data acquisition electronics of the TRD

There are four electronic boxes dedicated to the TRD data acquisition, consisting of two sets of U-crates with a UPD[2]-box. One of them is located on each side of the detector, mounted behind the radiators panels displayed in figure 3.1. Because the electronics of most of the subdetectors are designed in the same way, letters have been assigned to each subdetector to distinguish between them. To the TRD a "U"[3] has been assigned. The higher levels of electronics belonging to no particular subsystem are marked with a "J".

The U-crates are responsible for the data taking with the TRD. The flow of information and power is shown in figure 4.7.
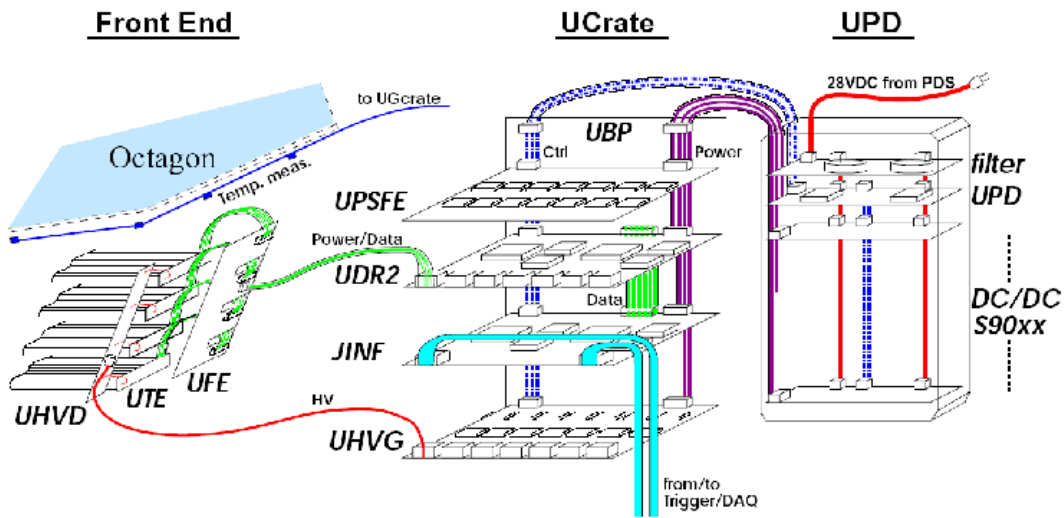
Figure 4.7.: ***The TRD data acquisition electronics.*** The UPD delivers the power for the U-crate and by that also for the front end electronics (purple lines). The high voltage for the straw tubes is generated in the UHVGs and distributed to the detector (red line). The signal of the tubes is digitized by the front end electronics (UFE), which receive the signal from the tube end electronic boards (UTE). The UDR2s collect the digital signals, apply data reduction routines and pass the relevant signals to the JINF-Us (data transfer illustrated by green lines) which bundle the information of their six associated UDR2s and pass them to the higher levels of AMS electronics (cyan lines). [121].

Every TRD module of 16 straw tubes has a tube end board (UTE), which passes the signals in the proportional chambers to the front end electronics (UFE). There two VA-chips[4] amplify the signal and flash Analogue to Digital Converters (ADCs) digitize the signals of the four connected UTEs. A range from 0 to 4096 ADC is available for this

---

[2]UPD: U power distribution.

[3]U: Übergangsstrahlung, German for transition radiation.

[4]VA-chip: Viking read out chip.

conversion. Each UDR2 collects the signals of seven UFEs and applies via the DSP a zero suppression algorithm to minimize the amount of data without loss of information. The interface board collects the data packages of the six UDR2s and assembles them to an event block. They are then read out by the higher levels of electronics. The data flow is illustrated in figure 4.8.
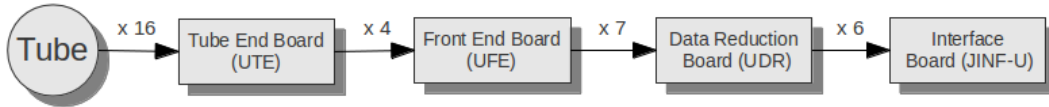
Figure 4.8.: ***TRD data flow for science data taking.*** The signals of all straw tubes of one module are recorded by the tube end electronics (UTE). The measurements of four UTEs each are digitized by the front end electronics (UFE). The UDR2s collect the digital signals from the seven connected UFEs, apply data reduction routines and pass the relevant reduced signals to the JINF-Us which bundle the information of their six associated UDR2s and pass them to the higher levels of AMS electronics.

The UDRs not only collect and reduce the science data, they are also responsible for the calibration of the read out channels and regular survey about the status of the read out electronics. The calibration, which calculates the pedestals and noise for the zero-suppression algorithm, is performed by reading out the electronic channels 1024 times with an internal trigger. From this the pedestal, being the mean of the accumulated distribution, and noise, being the width of the signal distribution, of each channel is calculated and stored for the following data processing [143]. The values of the pedestal and noise for all channels of a single calibration are shown in figure 4.9.

When reading out the straw tube signals after receiving a trigger from the system the UDR2s only consider those signals as energy depositions belonging to a particle crossing, which are at least five times the calculated noise of that channel above its pedestal. The minimal noise cut lies at 9 ADC, while the maximal applied threshold is at 15 ADC. In the current operation mode, these calibrations are performed at the start of every second data taking run, corresponding to every 46 minutes. The calibrations are arranged so that they coincide with the Earth's equator crossing, because there the particle flux is the lowest. Performing a calibration near the poles or the South Atlantic Anomaly can distort the results, due to the high particle flux. The calibration algorithm throws out a fixed amount of triggers with high amplitude due to energy depositions by particles per channel. If this number is reached, all following triggers are used for the calibration, even if they may contain energy depositions by traversing particles. The pedestal value would then be shifted to slightly higher values and the noise of the channel would be overestimated. Since this would have a negative impact on the data taking in the following run, the calibrations at the poles are skipped and the calibration results of the previous run are used.
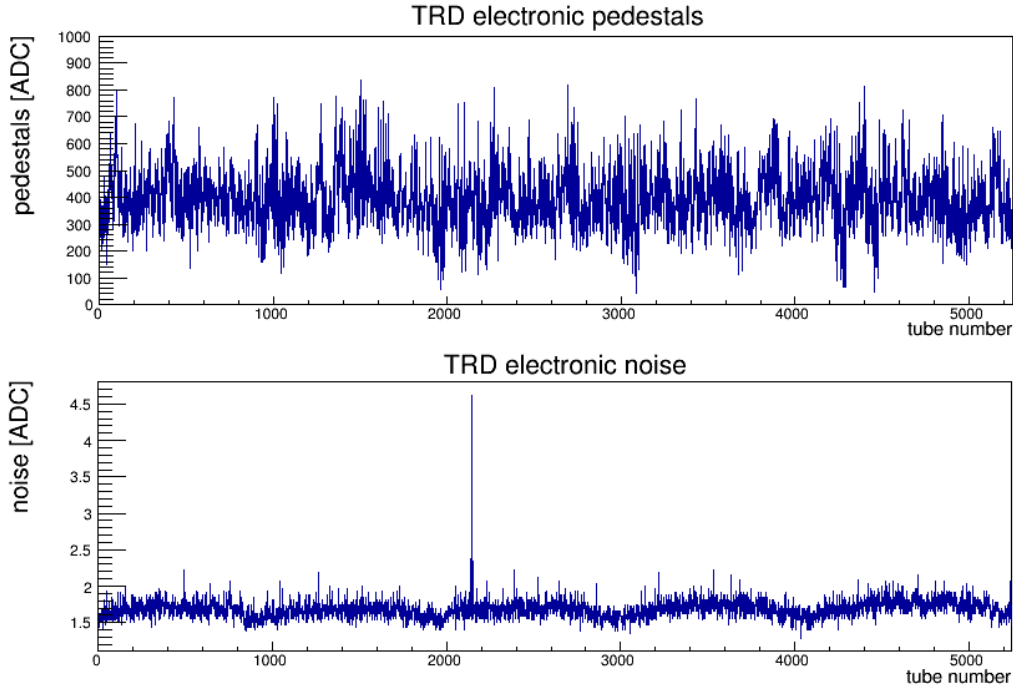
Figure 4.9.: ***Example of a calibration result.*** The pedestals vary from 100 ADC to 800 ADC between the different channels, whereas the noise is rather homogeneous at 1.8 ADC, with two neighbouring channels (2145, 2146) sticking out, which have always been known to be noisy due to cross-talk.

To ensure correct data taking, the status of the detector electronics, as well as the high voltage values of each channel are read out regularly. High energy particles in space hitting the electronic boards could lead to bit flips in the electronics or trips in the high voltage chains. This would impact the performance of the detector. Therefore the collected information of the system are displayed and monitored in the Payload Operations Control Center. In the POCC actions can be taken to correct bit flips or to restore the high voltage. Monitoring programs specifically designed for this task in preceding work were updated and optimized continuously as part of this thesis [126, 135].

4.5. Operation of the TRD

The TRD is operated at a high voltage between 1300 and 1500 V and a pressure in the straw tubes around 1000 mbar. These values were selected in order to have a stable detection of ionisation signals for particles of unity charge while still having a wide ADC range for the detection of transition radiation photons and the ionisation signal of ions up to boron without being saturated. To ensure the optimal performance of the TRD, the detector has been tuned on ground in test beams and with muons from cosmic rays [126]. One performance check conducted as part of this thesis was a scan of the additional delay

between trigger signal and detector read-out, which is left adjustable inside the digital signal processing (DSP) code of the electronics [144]. For this test the detector was operated in the high bay of the Space Shuttle Processing Facility at KSC. The signal therefore was dominated by the ionisation signal of muons. The delay needs to be chosen in a way that the actual peak of the signal is being recorded and not the rising or falling flank of it. For the scan the delay was adjusted over its full possible range from 100 ns to 5200 ns. To determine the best delay value, a data taking run was performed for each test setting. The measured signal amplitudes below 500 ADC were accumulated over the whole TRD and its mean value determined. The flux of muons on ground is homogeneous and the temperature conditions in the high bay were stable. Therefore the summing over all straw tubes does not introduce any bias in the measurements. The results are shown in figure 4.10. The highest read-out amplitude and therefore the best setting for this delay is achieved at 1560 ns, hence this value has been chosen as the current setting for data taking.
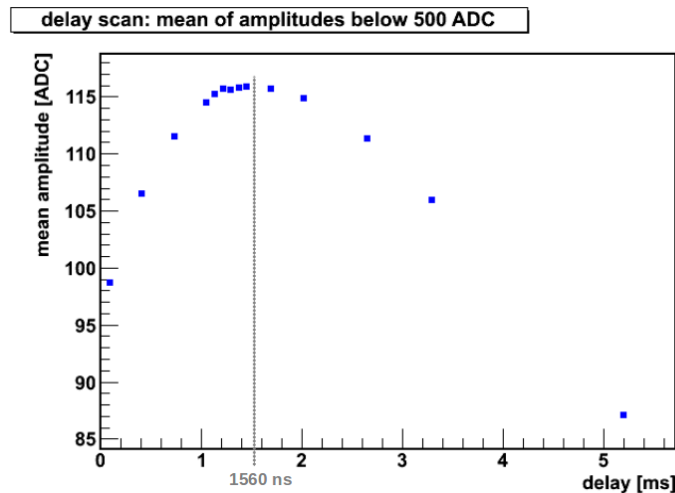
Figure 4.10.: ***Mean amplitude in the TRD for different delay settings.*** The mean of the amplitude below 500 ADC is plotted versus the adjustable delay setting parameter. A delay of 1560 ns has been chosen for further operation.

The temperature in space varies as a function of the incident angle of sunlight. Therefore it is monitored with 404 temperature sensors for the TRD. The amount of sunlight depends on multiple factors; the day and night passages of the Space Station, the orientation of the ISS as well as the position of the ISS radiators and solar arrays play a role. In case the temperature of the TRD pump would drop below 10° C, which is close to the lower threshold of its operational range, actions would be taken to stop a negative trend of the temperature. This can either be done by activating certain heater lines or by asking NASA to move the radiators or solar panels of the ISS to a more favourable position for AMS-02.

The continuous loss of gas in space leads to a change in the gas amplification of the particle signal. The major impacts on the gas amplification are:

- gas pressure

- gas composition

- high voltage

- temperature.

While lower gas pressure and the diffusion of CO_2 lead to higher signal amplitudes, lower high voltage reduces the signal again. A good range in operation pressure of the TRD, which is between 900 mbar and 1000 mbar, demands for gas refills about every four weeks. These refills impact the data taking. Therefore they are reduced to the minimum. To avoid big changes in the gas amplification during the period between two refills, the HV of the tubes is adjusted on a daily basis. In the first month of operation, this was done only once per week, but first analyses of the science data showed that a more stable signal would improve the performance of the detector. On average the high voltage is lowered by about 3 V. This value, though, again depends on the overall temperature trend of the detector. The remaining inhomogeneity in the single straw tube signals due to time dependent local variations of the gas amplification is corrected in an offline calibration, which is described in the next section.

4.6. Offline calibration of the TRD

As described in section 4.5 about the operation of the TRD, the temperature impacts the analysis of the data in two ways, on the one hand it changes the gas gain in the straw tubes and thereby the detector response to the measured particle. On the other hand it causes the support structure of the detector to move and/or deform. The movements affect the particle identification, because in order to well distinguish between protons and positrons the length of the path of the particles in the straw tube needs to be known. The distance travelled by the particle within the straw tube walls is approximated by extrapolating the Tracker track into the TRD volume. The 3-D path length is calculated as the distance between the two points of intersection of the track with the TRD straw tube walls, as depicted in 4.11.

The deposited energy of a particle is proportional to the number of initially ionized gas molecules and therefore theoretically linearly dependent on the path length in the material. The signal dependence on the travelled path length in the straw tube can be seen in the right plot of figure 4.11. The linear dependence holds true as long as a minimal distance of about a half of the most probable distance of 6 mm is crossed. For shorter path lengths the Landau distributions of the signal amplitudes is distorted, because the fluctuations to low amplitudes are cut off by the noise cut. Also small path lengths are affected stronger by small errors in the alignment of the TRD modules or the Tracker track extrapolation, which
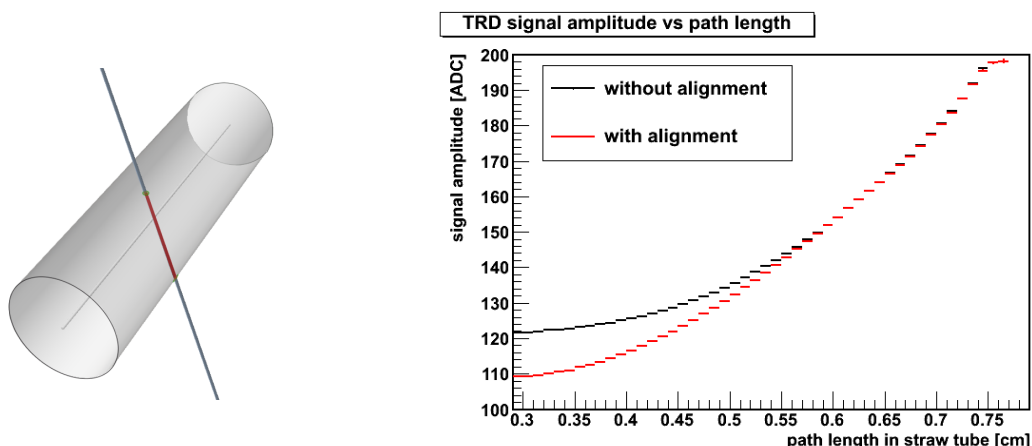
Figure 4.11.: **The path length dependency of the TRD signal.** Left: particle path inside a TRD straw tube. Right: TRD signal dependence on path length, black: without alignment, red: after alignment corrections applied. The alignment of the straw tubes improves the sensitivity of the signal amplitude on the path length inside the tubes for smaller path lengths.

is used to determine the path length, since the path length changes rapidly at the edge of the straw tubes. These two effects lead to the non-linearity in the average amplitude dependence on the path length for short distances travelled in the straw tubes.

An alignment of the straw tubes as well as a calibration of the gas gain with time are performed to optimize the performance of the detector and thereby achieve a good separation power between protons and positrons.

4.6.1. Gain calibration

Two methods for the TRD gain calibration are available, called the TrdQt method [145], set up by the RWTH Aachen group, and the TrdK method [145], developed by the MIT/Taiwan groups. As both methods are rather similar, only the TrdQt method is explained in the following.

The correction for the calibration of the gas gain are calculated using the most probable value (MPV) of the amplitude of the energy deposit in the TRD by protons. Protons qualify for this procedure due to their high abundance in cosmic rays and low probability of emission of transition radiation, which allows a calibration using the ionisation signal only. The protons of cosmic rays have an average energy around 8 GeV[5], their amplitude spectra in ADC[6] counts is shown in figure 4.12.

The deposited energy by a proton due to ionisation can be calculated by the Bethe-Bloch formula , see equation 4.2. The energy loss in thin layers fluctuates according to a Landau distribution [146]. The Landau distribution can be characterized by 3 parameters, namely

---

[5]The spectral shape can be seen in figure 2.3.
[6]ADC: analogue to digital converter.
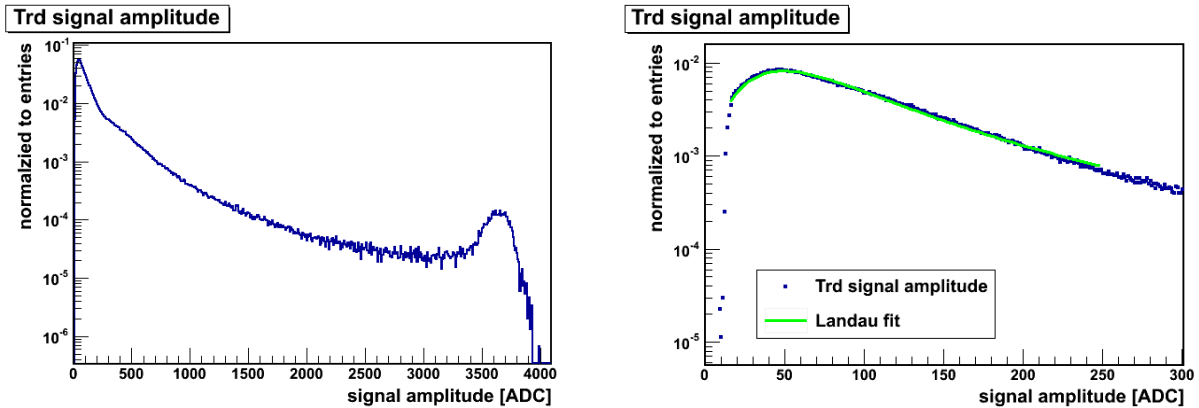
Figure 4.12.: **TRD signal amplitude spectra.** Top: all cosmic ray TRD signal spectrum over the full ADC range. The accumulation of signals above 3500 ADC is due to overflow of the finite signal range of 4095 ADC, whereof the electronic pedestals of on average 400 ADC is lost for amplitude discrimination, see figure 4.9. Bottom: Landau fit to the TRD signal amplitudes of unitary charged particles below 250 ADC to determine the MPV of the distribution, which is used for calibration.

a normalization factor, the most probable value and the width of the distribution. The proton signal in the TRD is fitted with a Landau function to determine the MPV of the distribution, which is further used as an indicator for the change in the gas amplification. The MPV, determined with the TrdQt method, is fluctuating around an average signal of 100 ADC per cm of path length in the straw tubes. For every module the MPV is determined in time intervals according to their hit occupancy. The calculated values are written to a data base and are used to normalize the data during analysis by comparing the accumulated MPV value to the standard value of 100 ADC counts per cm. The time dependence of the MPV for one module[7] is shown in figure 4.13. After the correction is applied the detector response is stable for all tubes within 2%.

4.6.2. Alignment

As mentioned the temperature in space varies as a function of the incident angle of sunlight, which depends on the solar beta angle, the day and night passages of the Space Station, the orientation of the ISS as well as the position of the ISS radiators. The solar beta angle, which is defined as the angle between the ISS orbit plane and the sun vector, has the strongest impact on the temperature of the TRD. The definition of the beta angle is illustrated on the left hand side in figure 4.14.

Although the angle between the Earth's rotational plane and the sun vector is constant at 23.5° and the inclination of the ISS orbit is fixed at 51.5° to the Earth's rotational plane, the beta angle changes. The orbit axis of the ISS precesses around the Earth's rotational

---

[7]For the numbering scheme of the TRD modules see section A.2.
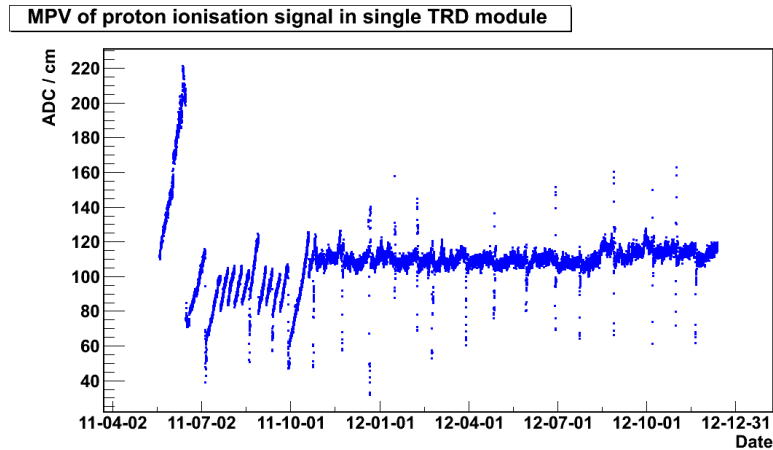
Figure 4.13.: **Gain for module 212 retrieved from the TrdQt database.** The MPV of a representative module for 18 month of data taking is shown. In the first days no HV adjustments were made, which leads to the strong rise in the MPV. In the first month weekly HV adjustments were performed, while in October 2011 the operation mode was changed to daily HV adjustments to keep the MPV more stable. The outliers are due to ongoing gas refills. After applying the gain calibration the MPV is kept stable within 2%.
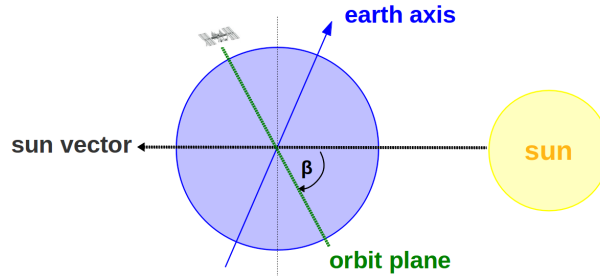
Figure 4.14.: **ISS beta angle definition.**

axis with a rotational velocity of 5.02° per day. Including the rotation of the Earth around the sun, the change of the orientation of the ISS orbit plane to the sun vector is about 6° per day leading to beta cycles of 60 days [147]. The beta angle indicates the fraction of time of one orbit the station is exposed to sunlight, with a 0° β having the smallest fraction of sunlight exposure, as the station spends the maximal amount in the shadow of the earth. A 90° β angle on the contrary implies a constant exposure to sunlight, as the orbit axis is coinciding with the sun vector and therefore no part of the orbit leads through Earth's shadow. The beta angle of the Space Station is varying between $+/-75°$, which causes variations of the average temperature of the detector. The temperature variations on their part invoke relative movements of the TRD modules to the inner Tracker, resulting in the

need for alignment corrections. The higher temperature due to the inclination of sunlight makes the part of the detector expand, which is faced towards the sun. As a consequence the TRD modules are moved by up to 1 mm. The shift of a TRD module with time, which is representative for all modules aligned with the y-axis, is shown in correlation to the beta angle in figure 4.15.
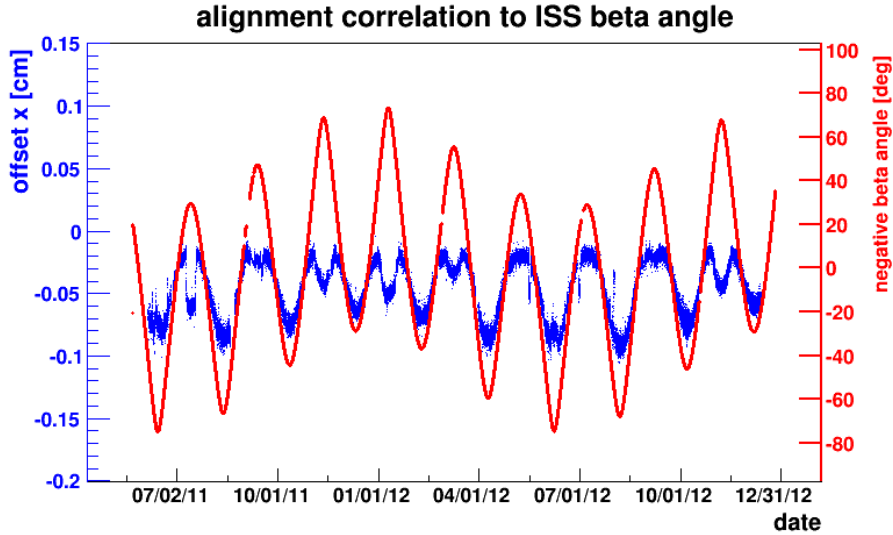
Figure 4.15.: **Alignment correlation to ISS beta angle.** Correlation of the negative of the beta angle and the horizontal alignment offset of one module measuring the x-direction. The periodic structure following the β-angle can be seen as well as sudden changes in the alignment due to changes of the orientation of the Space Station, e.g. for Space Shuttle docking/undocking in July 2011 or Soyuz docking/undocking on 15th of May 2012 and 15th of July 2012. The double-peak structures in the alignment correction, which appear for high negative beta angles, are due to a repositioning of ISS radiators, which is done for $\beta < -45°$. The beta angle data is provided by NASA [148].

In order to reduce the fast changes in temperature for the detector, it is wrapped in multi-layer insulation, by which the temperature change become below 1° C between the day and night parts of each orbit. Still the day and night impact on the detector results in a movement of the tubes of about 100 μm, as shown in the lower plot of figure 4.16. In order to be able to correct for the effect of day and night during one orbit, the time unit for which a alignment correction is calculated should be of the order of 10 minutes.

Different alignment methods are present in the official AMS software, with their results being stored in a database. Those can be accessed during analysis to correctly calculate the path length of the particle through the gas volume. The path length is used to normalize the signal to the mean path length of 6 mm. As part of this thesis a novel alignment method was developed, taking into account both TRD signals as well as so called "missing signals". These are instances, where a particle does not deposit energy in a layer of the
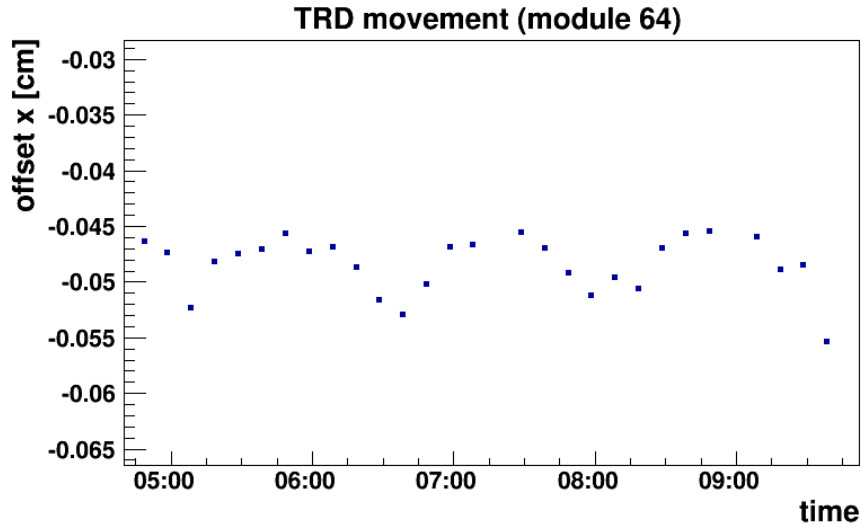
Figure 4.16.: ***Alignment corrections of one module for 18 month of data taking.***
The r-direction for this module corresponds to the x-direction of the AMS
coordinate system. The plot shows the periodical change in alignment of the
detector on the orbital time basis of 90 minutes due to the day and night
passages.

TRD due to single layer inefficiency. Details on this method as well as earlier alignment
methods are presented in chapter 5.

5. Missing signals in the TRD

A particle crossing the TRD within its full acceptance should deposit energy in every of the 20 TRD layers, but on average only 19 energy depositions are detected. One explanation of these missing signals are statistical fluctuations of the ionisation signal down to low amplitudes which are dropped by the noise cut as explained in chapter 3. Another reason for less than 20 signals in the TRD is the geometrical efficiency of a single layer; about 95% of each layer is active material, taking the dependence on the inclination of the particle track into account this efficiency of a single layer is at 94.5%, as can be seen from figure 5.1.
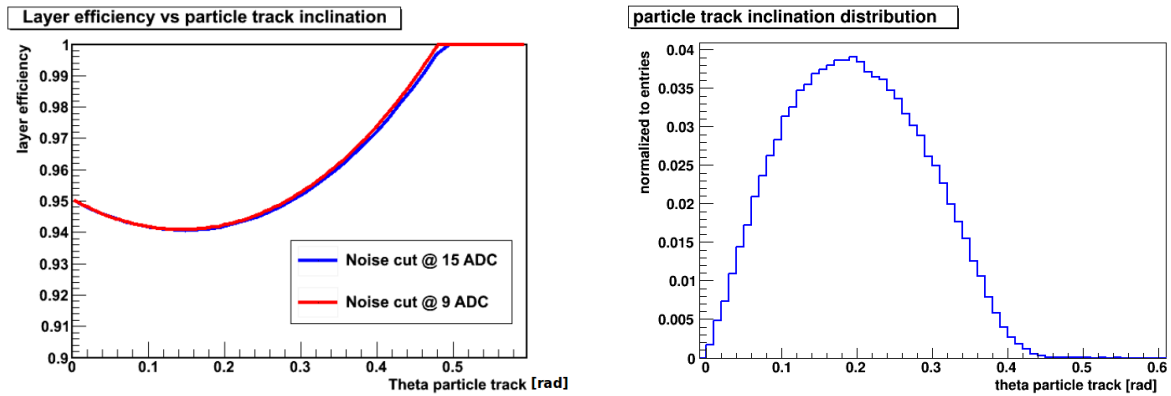
Figure 5.1.: ***Single TRD layer efficiency dependence on the particle track inclination.*** Left: dependence on particle track inclination of single layer efficiency based on geometrical calculations for a noise cut of the amplitude at 9 ADC (red) or 15 ADC (blue). Right: distribution of the particle track inclination in space data.

As a consequence of the single layer inefficiency there is a 68% chance that a particle passes between two tubes in one of the 20 traversed layers. An illustration of this is shown in figure 5.2.

The straw tubes of the TRD have an inner diameter of 6 mm, which yields a single point resolution of 1.7 mm. The gap between two tubes is either 60 μm or 360 μm wide depending on the presence of a support stringer between the tubes. Compared to the width of a straw tube, a missing signal gives a high resolution point of passage of the particle. The missing signals can be used for the alignment of the TRD as well as for improving the tracking in the TRD and thereby refining the calculation of the path length inside the straw tubes.
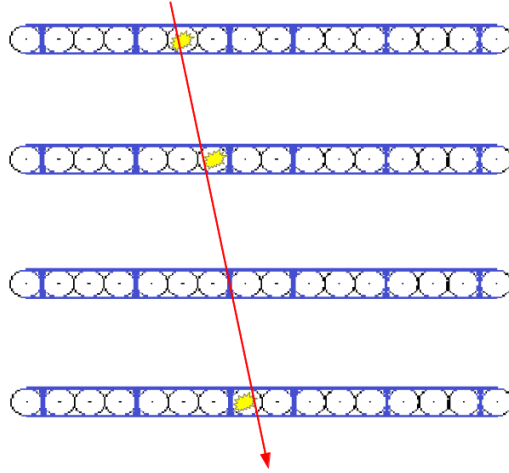
Figure 5.2.: ***A missing signal in the TRD due to single layer inefficiency.*** With a probability of 68% a particle, passing all 20 layers of the TRD, passes between two straw tubes in one of the layers.

In the first section of this chapter the definition and resolution of missing signals are given. Section 5.2 describes the alignment of the TRD, including the information of missing signals and in section 5.3 the track refit method using these additional points of passage is presented.

5.1. Definition and resolution

In order to profit from the higher resolution of missing signals in the TRD, the first task is to set up an identification routine. The definition of a missing signal is done in the following way: a TRD layer without an energy deposit in a 1 cm cone around the particle track is considered as a missing signal candidate. A quality selection is applied by requesting signals on the particle track in the two neighbouring layers[1] and by checking that the track extrapolation points to a gap inside a TRD module rather than between two modules. The latter is done since gaps between modules have a worse spatial resolution due to the staggered assembly of the modules. In order to determine the exact location of a missing signal the Tracker track is extrapolated to the TRD candidate layer. The two straw tube wires closest to the extrapolation are identified in order to define the gap through which the particle must have passed. Since a TRD signal has only a 2-dimensional resolution, the same is true for a missing signal. The r- and z-coordinates of the missing signal[2] are defined as the average of the two neighbouring straw tube coordinates each. The third coordinate can be defined by the track extrapolation, but it is not used in the applications of missing signals that are presented in the later sections of this chapter.

---

[1]For layer 0 and layer 19 only a signal on track in layer 1 or layer 18, respectively, is needed.
[2]The r-coordinate corresponds to x for layers 4 to 16 and y for all other layers.

The resolution of a missing signal is given by the inactive region between the two closest straw tubes. This region is given by three different contributions:

- the distance between the tubes

- the walls of the straw tubes

- the noise cut of the data reduction algorithm

The gap between two tubes is in principle 60 μm wide[3], for straw tubes with a support stringer located between them[4] an additional 300 μm have to be added to the the gap width. The wall of a straw tube is 72 μm thick, which leads to a contribution of 144 μm to the inactive region between two straws tubes. The last contribution is due to the noise cut of the data reduction routine. As described in section 4.4, the TRD signal amplitude is proportional to the path length of the particle track inside the straw tube. Therefore path lengths below 1.5 mm might result in a rejection of the signal. In order to exceed this path length, the particle must cross the straw tube in a distance of at least 40 μm from the tube wall. The resolution of a missing signal according to:

$$\sigma = \frac{d}{\sqrt{12}} \tag{5.1}$$

with d being the gap width, is therefore either 80 μm or 160 μm [140].

Figure 5.3 shows the projection of the Tracker track extrapolation to missing signals on the y-axis of a TRD module. The frequency of occurrence of having a missing signal clearly corresponds to the width of the gaps.

As mentioned before, gaps between two modules are not considered as missing signals, as a result the single module efficiency, given in figure 5.4, is determining the probability of having a missing signal on the track rather than the single layer efficiency. Taking the most probable track inclination into account, which is shown in figure 5.1, a missing signal occurs in about 55 % of the events. This reconstructed point of passage of the particle with a good resolution can be used to improve the alignment of the TRD as described in the next sections. In addition to the alignment, this information of the particle path can be used to improve the tracking in the TRD volume as described in section 5.3.

5.2. TRD alignment with missing signals

So far there were two different versions of alignment of the TRD implemented in the AMS software. The standard procedure to determine the change in the position of the TRD straw tubes is to use the Tracker track, since this is the best known estimation of the

---

[3]This is correct for gaps between tubes 2 and 3, 3 and 4, 5 and 6, 6 and 7, 8 and 9, 10 and 11, 11 and 12, 13 and 14, 14 and 15, compare to figure 4.4.

[4]This applies to gaps between tubes 1 and 2, 4 and 5, 7 and 8, 9 and 10, 12 and 13, 15 and 16, see figure 4.4.
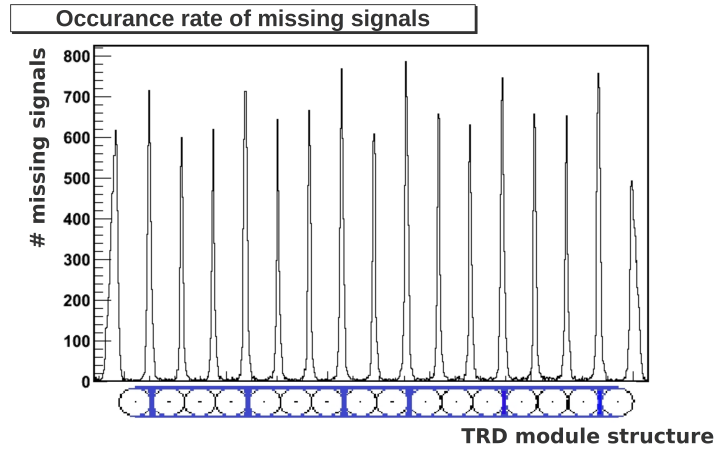
Figure 5.3.: **Missing signals in a module of the TRD in comparison to the module structure.** Gaps with a module support stringer (blue structure) between the straw tubes show a higher occupancy of missing signals due to their larger width.
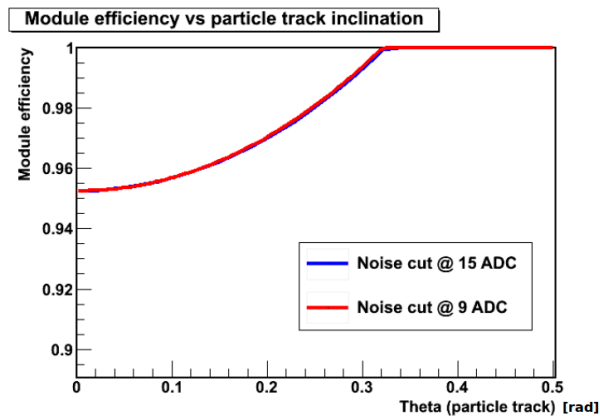
Figure 5.4.: **TRD single module efficiency dependence on the particle track inclination.** The single module efficiency dependence on the particle track inclination, retrieved from geometrical considerations, for a noise cut of the amplitude at 9 ADC (red) or 15 ADC (blue). The noise cut results in a minimal detectable path length, which effectively reduces the active volume of the straw tubes.

particle track. The Tracker track is extrapolated to each responding TRD tube, where the track position is compared to the default position of the straw tube wire[5]. In this way the full active region of the TRD tube is sampled, which can be compared to the nominal

---

[5]In fact, the track is interpolated in case of a Tracker plane 1 hit belonging to the track, but further it is anyway referred to as extrapolation.

position of the tube.

The differences between the alignment methods are given by the detector element for which they calculate the correction, the dimensions in which they correct and the time intervals. The TrdQt [145] alignment calculates one time based offset in the horizontal direction for each of the 328 modules. The time intervals for the correction vary per module ranging from 40 minutes to 8 hours depending on the hit frequency of each module. The TrdK [145] alignment provides six correction parameters for each of the 20 layers of the TRD in time intervals of twelve hours. These six parameters are offsets along and rotations around the x-, y- and z-axis in the AMS coordinate system. This of course assumes that the modules in each layer move coherently. In addition to the calculation of the layer alignment, the TrdK method also calculates these six parameters for the whole detector on small time scales to be able to correct for the orbital movement. A sliding window of five minutes is used to calculate the alignment parameters every ten seconds. The TrdQt alignment with its big time intervals swallows the orbital movement, which is in the order of 100 μm as can be seen in figure 4.16. The TrdK assumes that the TRD or the TRD layers move as a rigid body, which is only true to a certain extend. Modules within one layer show different misalignment, which can be seen in figure 5.5. Looking at the counts of single straw tubes giving a signal, but being just missed by the Tracker track extrapolation, it is clearly visible that certain modules have a higher frequency of these off-track signals. This can be fixed by applying a module based alignment correction.
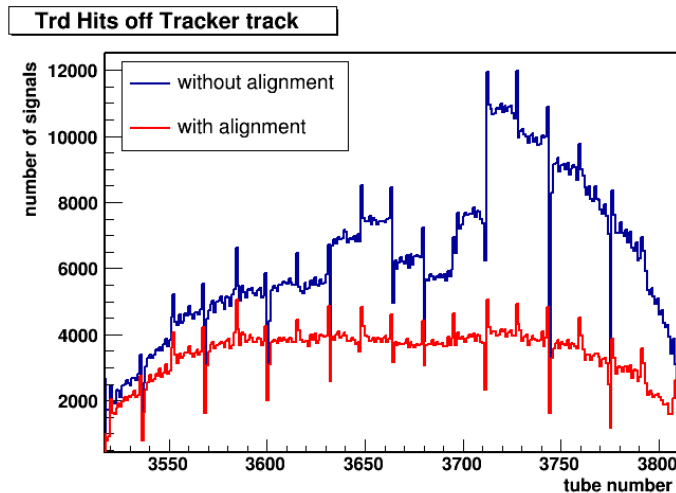
Figure 5.5.: ***Number of TRD signals just off the Tracker track extrapolation for each straw tube of one TRD layer.*** The number of occurrences of missing a tube signal with the Tracker track extrapolation is shown in blue without any alignment corrections applied and in red after applying the alignment produced in this thesis. The lower occurrence rate on the edges of the layer is simply due to acceptance.

5. Missing signals in the TRD

A new method, called TrdM[6], has been developed as part of this thesis. This alignment method not only uses the information of the responding straw tubes in the TRD of each event, but also the missing signals as introduced in the last section. The missing signals add measurements with high resolution to the calculation and therefore have the potential to improve the determination of the alignment parameters. The impact of the missing signals though is reduced by their low abundance compared to the TRD signals.

The element on which this alignment procedure is performed is a TRD module. Due to statistical limitations for the calculation and considering the material properties of the module structure, the straw tubes within a module can safely be assumed to be rigid. Hence for each TRD module, the information of the 16 tubes can be used to calculate corrections to its nominal position. The TrdM alignment calculates four alignment parameters per module:

- shift along the x/y-axis[7]

- shift along the z-axis

- rotation around the x/y-axis[7]

- rotation around the z-axis.

In order to determine the alignment corrections, the Tracker track is extrapolated into the TRD volume. The set of tracks, which deposit energy in the straw tube, sample its active volume and thereby they can indicate the shift of the straw tube with respect to its nominal position. This is illustrated in figure 5.6. The individual track offsets in x/y- and z-direction, being the distances between the point of closest approach between the track and the nominal position of the straw tube wire are calculated and filled into histograms for x/y and z for each module separately. Missing TRD signals in the event are treated equally to the regular signals, so that the distance between the track extrapolation and the given gap is determined.

As a compromise between statistics and intrinsic resolution the calculation is done on time intervals of ten minutes. This ensures that the orbital movement of the modules is still traced, while the number of measurements is reasonable. Since the number of particles crossing each module in a certain time window varies according to the location of the module in the detector, a sliding window approach based on the number of measurements is being used. As a consequence measurements in the outer modules of the detector, which have a lower hit frequency, are used in more consecutive calculations than in modules in the central part of the TRD. In order to determine the correction parameters, always four histograms are filled with the information of the last 7500 measurements in each module. One-dimensional histograms are used for the shifts in r- and z-direction. They

---

[6] The TrdM method includes the new alignment and track refit using missing signals, which are described in this chapter, and provides an electron likelihood estimator as presented in chapter 6.

[7] According to the orientation of the TRD modules, they are only sensitive to the location of a signal in either x- or y-direction. For TRD layers 0-3 and 16-19 the correction is calculated in the x-direction while for layers 4-15 this is done in the x-direction.
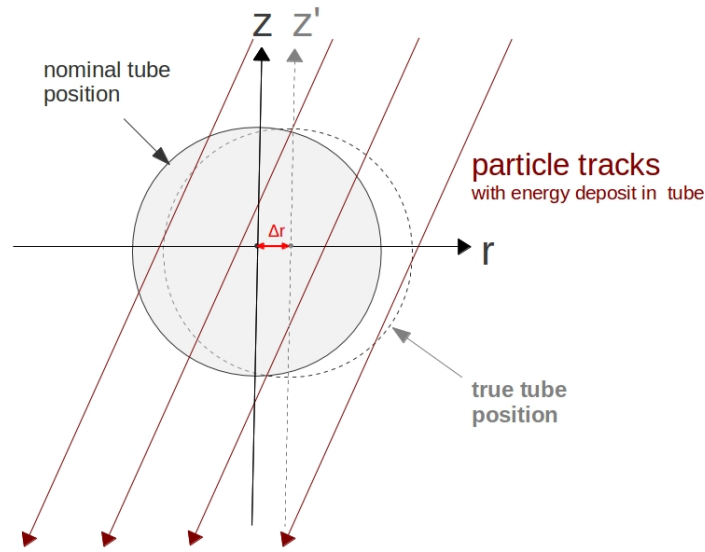
Figure 5.6.: ***Calculation of the offsets for the alignment.*** The set of tracks, which deposit energy in the straw tube sample its active volume and thereby they can indicate a shift of the straw tube with respect to its nominal position. Here a simplified example for only a horizontal shift is illustrated.

are fitted with Gauss functions from which the shift corrections are then retrieved as the peak position of the Gaussians. For the rotation correction around the z-axis the shifts in the x/y-direction are plotted in the x-y-plane, where the non measuring direction is given by the track extrapolation. An example is shown in figure 5.7. Similarly for the rotation around the x/y-axis the shifts in the z-direction are plotted along the tubes. The two dimensional histograms are fitted with a straight line; the rotation of the module is given as the inclination of the fit result.

The corrections in horizontal and vertical direction are calculated at the same time. Due to the rather small θ angles of the tracks that are within the Tracker acceptance, the points of closest approach tend to have a larger offset in the horizontal than in the vertical direction. Therefore the precision of the alignment correction is higher for the x/y-shifts and the retrieved corrections in z are small. The calculated rotational corrections are minor, especially for modules located in the central part of each layer. They do not show any trend but only a certain spread, which corresponds to changes on short time scales. Modules located at the edges of the detector show a small trend on long time scales in the order of 5 $\mu m/cm$, which does not have an effect for particles crossing the central region of the straw tubes, but can lead to corrections of 500 μm in the outer parts.

As an example, the obtained horizontal alignment corrections of one module aligned with x and y, respectively, for the first 18 month data period are shown in figure 5.8.

Modules located in the same layer move rather coherently, but they have time independent offsets as mentioned before. To illustrate this the horizontal movements for one
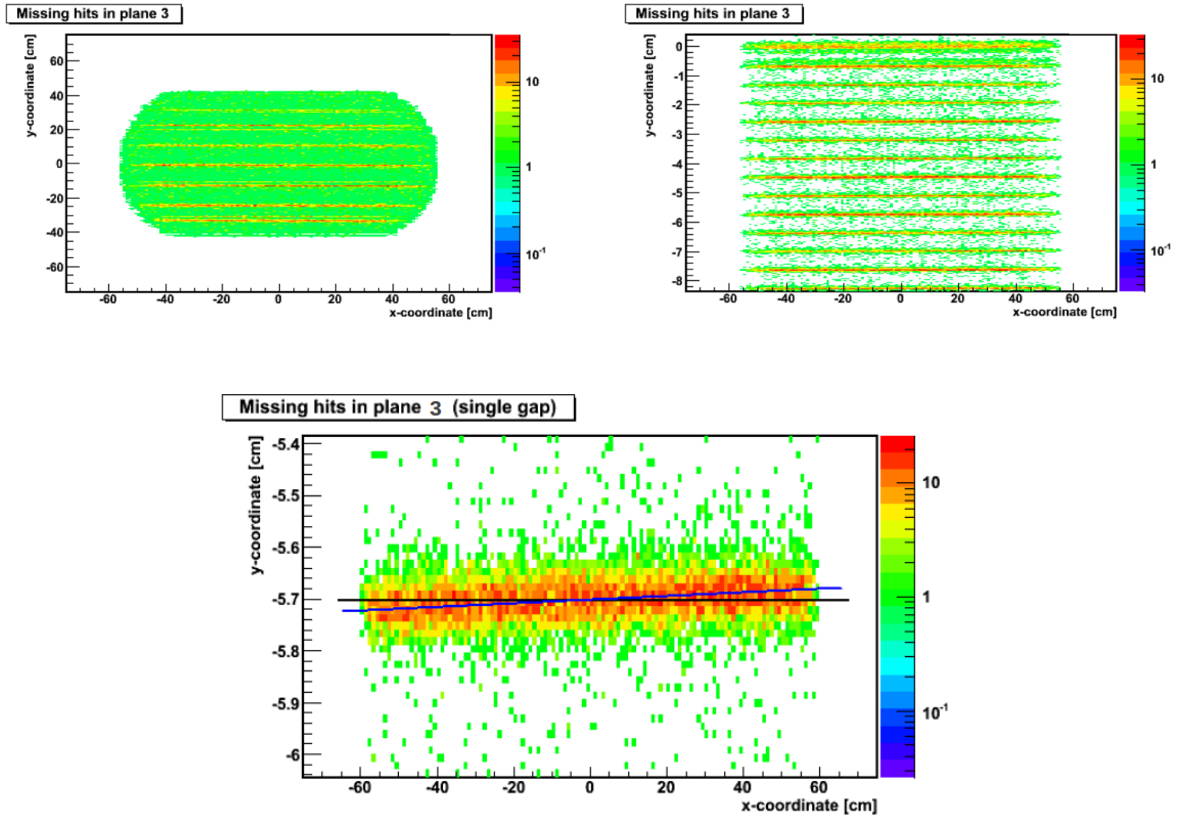
Figure 5.7.: **Locations of missing signals found in TRD layer three.** Track extrapolation to missing signals in all of TRD layer three, a zoom where single gaps can clearly be distinguished and a closure on a single gap. The black line indicates the nominal gap position, wherein the blue line represents the determined position and orientation.

module located in the middle and one located at either side of TRD layer 7, are presented in figure 5.9.

The horizontal shift residuals for two modules before and after the alignment are shown in figure 5.10. For this comparison the alignment has been calculated for a downscaled set of data[8] using only half of the events and it has been tested on the other half. This worsens the resolution of the alignment, because the statistics for the determination of the alignment corrections are reduced, while the time basis is kept the same. The residual resolution for a single module considering the horizontal shift, which is affected the most by the temperature induced movements as can be seen in figure 5.8, is on average 48 μm.

The impact of using missing signals in addition to the regular TRD signals in the alignment calculation can be seen from figure 5.11. Here the alignment has been calculated with TRD signals only following the same approach of calculating the alignment parameters on

---

[8]The alignment impact has been calculated on a downscaled sample of approximately 20% of the data.
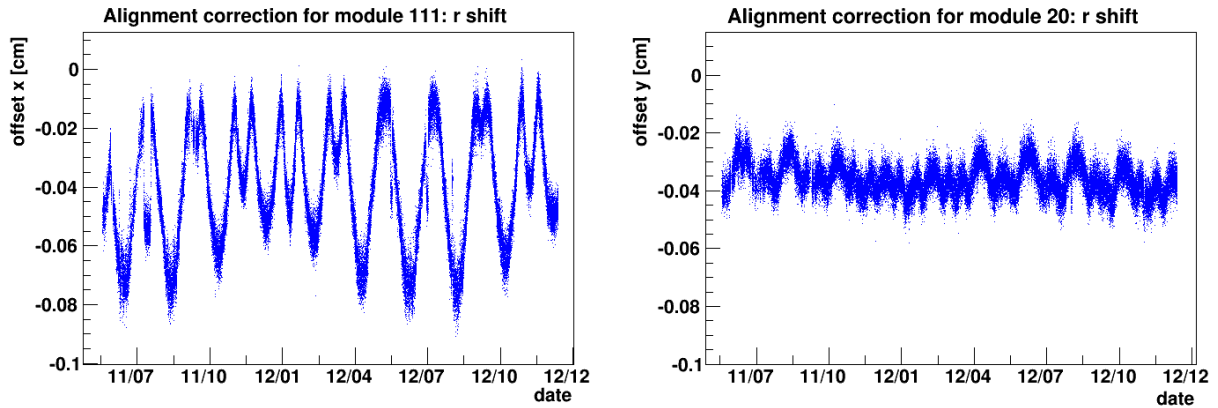
Figure 5.8.: ***Time dependent horizontal alignment parameters of modules 111 and 20.*** Top plots: shift in r(=x for module 111 (left), =y for module 20 (right)).
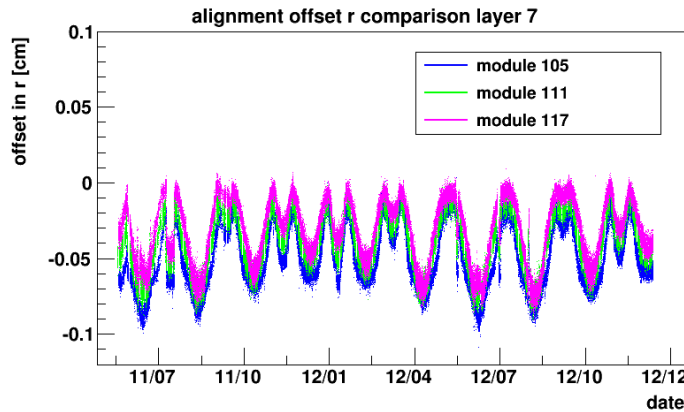
Figure 5.9.: ***Alignment shift comparison of modules of the same layer.*** The horizontal movements of different modules in the same TRD layer show a well correlated behaviour, but also a time-independent offset between the different modules.

one half of the events and applying it to the other half of the events to check the impact. The spread of the residual shifts is larger compared to the alignment method including the missing signals by ∼10 %.

The goal of the alignment is to improve the calculation of the path length of the particle in the TRD straw tubes. The determination of the path length is only possible if the extrapolated Tracker track actually crosses the volume of the tube. Therefore the number of TRD signals along the extrapolated track is a good estimate for the impact of the alignment. A comparison of this value before and after application of the alignment corrections is shown in figure 5.12. The gain of the alignment is in the order of one additional hit on track for every second particle. As it will be shown in section 6.1 that the TRD particle
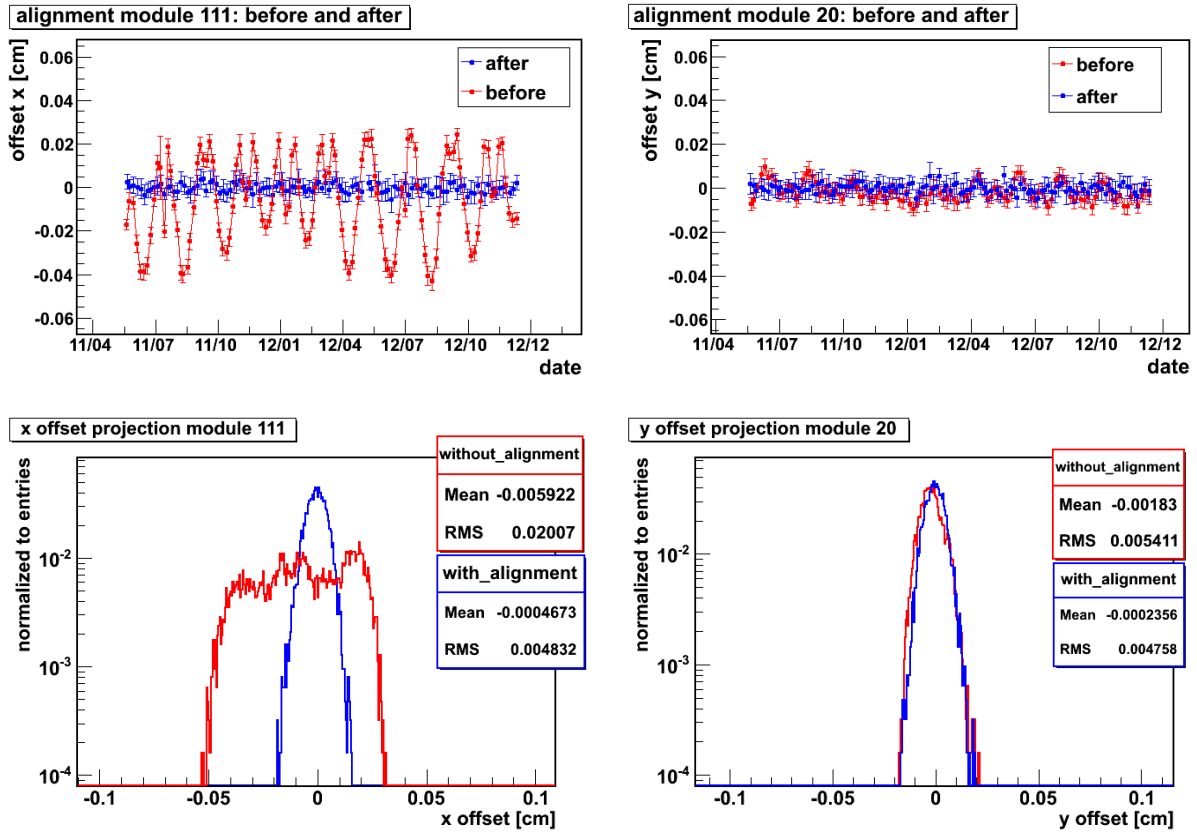
Figure 5.10.: **Spread of x/y residuals before and after the alignment for module 111 and module 20.** Top plots: time dependent offset before and after alignment. For better comparison the unaligned curve has been centred around zero by applying a time-independent correction. Left: module 111 measuring the x-direction, right: module 20 measuring the y-direction; red: before alignment, blue: after alignment. Lower plots: projection on the y-axis of the top plots. The width decreases strongly for modules in the x-direction, where the movement is more prominent.

discrimination power depends exponentially on the number of signals on track, this gain improves the TRD performance by ~ 40 %.

A comparison to the other available TRD alignments (TrdK, TrdQt) is difficult, as a comparison of the residual resolution is not fair, due to the different time scales and TRD components, for which the corrections are calculated. As the different TRD methods not only use different alignments, but also different track reconstructions, which impact the number of TRD signals on the track, a comparison of this would also not show the quality of the different alignments. Therefore only the final particle discrimination power of the different methods can be compared, as will be done in section 6.1.

The alignment has been incorporated into the AMS software and is further on applied within the TrdM method without additional notice.
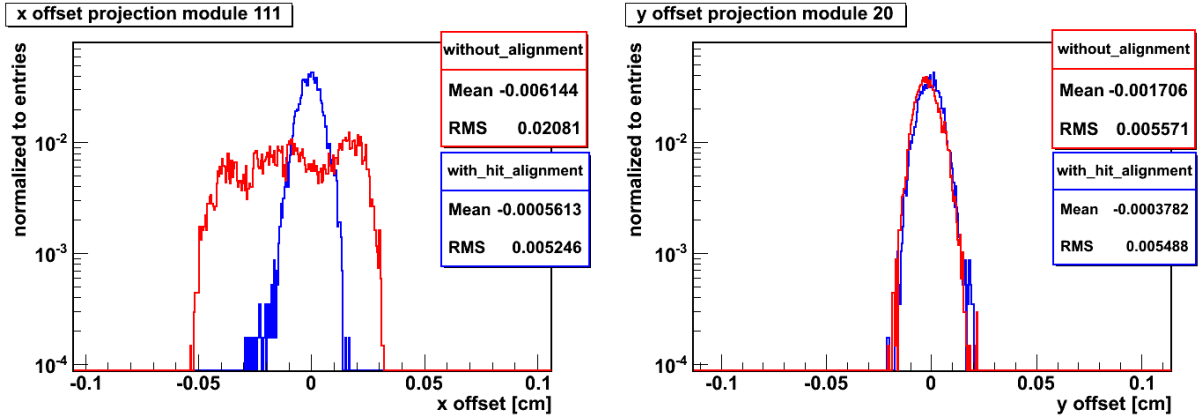
Figure 5.11.: ***Spread of x/y residuals before and after 'signal-only' alignment of module 111 and module 20.*** Red: before alignment, blue: after alignment. On the left the residuals for module 111, measuring the x-direction, and on the right the residuals for module 20, which measures the y-direction, are shown. The spread of the residuals is ~ 10 % larger compared to the alignment including missing signals.

5.3. Tracker track refit with TRD missing signals

The standard procedure to determine the TRD signals usable for the particle identification is to extrapolate the Tracker track into the TRD volume. Only those straw tubes with an energy deposit are considered, which are crossed by the Tracker track. For those signals a gain correction, according to the procedure described in chapter 4, and a path length normalization are applied. They are then used to calculate the electron likelihood of the particle, as described in the next chapter. The particle separation power of the detector strongly depends on the goodness of the path length determination and the number of signals used for the likelihood calculation. Therefore a good track extrapolation to the TRD signals is important. On the TRD side the alignment ensures a good knowledge of the actual position of the straw tubes, for the Tracker track, though, there are some effects that can result in a bad track extrapolation. One of these effects is multiple scattering [149]. The width of the central angular distribution covering 98% of the scattering angles approximated with a Gaussian is given by

$$\theta_0 = \frac{13.6 MeV}{\beta cp} z \sqrt{x/X_0} [1 + 0.038 \, ln(x/X_0)], \qquad (5.2)$$

where βc is the velocity, p the momentum and z the magnitude of the charge of the incident particle, and x/X_0 is the thickness of the scattering medium in radiation lengths [52]. Due to the inverse proportional dependence on momentum and velocity of the particle the scattering width is larger for lower energetic particles. This scattering of the incident
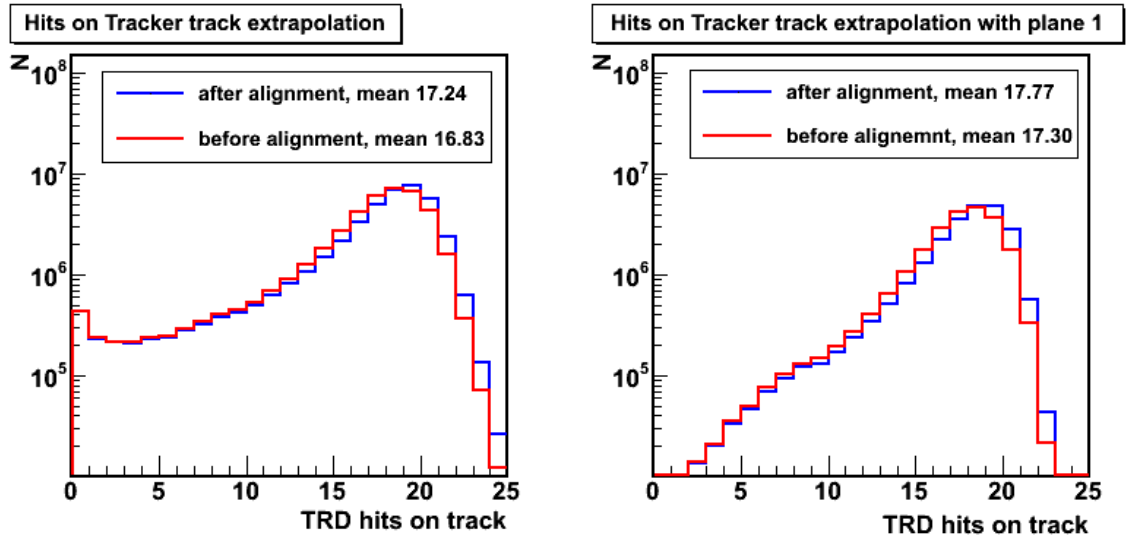
Figure 5.12.: ***Comparison of the number of TRD hits on the track extrapolation before and after the alignment.*** Left: hits on track without a Tracker plane 1 hit associated to the track, right: tracks with a Tracker plane 1 signal. Black: before alignment, red: after alignment. The gain of the alignment correction is in the order of one additional hit on track for every second particle. Since the particle discrimination power of the TRD depends exponentially on the number of signals per track, as will be shown in section 6.1, the gain of the alignment improves the TRD performance significantly.

particle might lead to a mismatch between the extrapolated Tracker track and the true particle path. The same mismatch occurs in case the incident particle undergoes an interaction in one of the upper ToF layers between the TRD and the inner Tracker, giving a kink to the true particle path. The default Tracker track reconstruction algorithm is not capable of reconstructing such a kink. Therefore the extrapolation of the track will follow the direction of the particle path after the interaction in the ToF and thereby might miss the TRD straw tubes in which the particle deposited energy. An example of such a particle track is shown in the AMS event display in figure 5.13.

Both effects have a much stronger impact on the extrapolation of the Tracker track, if there is no signal in the Tracker layer one detected, which is located on top of the TRD. Presence of this signal allows to interpolate instead to extrapolate the Tracker track and therefore takes a position of the particle passage before interaction or multiple scattering into account. Since the Tracker layer one only covers the central 35% of the uppermost TRD layer, about every second good event[9] does not have such a signal. A missing signal in the TRD with its high spatial precision can make up for the absence of a Tracker signal in plane one, because it adds a point of passage of the particle inside the TRD volume. Testing the incorporation of missing signals to the Tracker fit, it was also found that slight

---

[9]For the selection criteria of a good event see chapter 7.
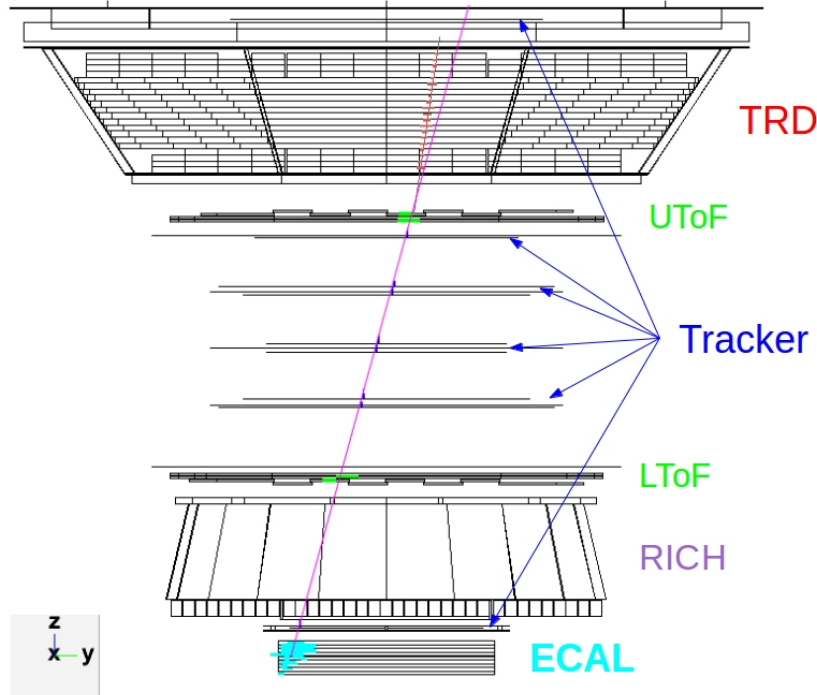
Figure 5.13.: ***AMS-02 event display: a Tracker track extrapolation that misses the TRD signals.*** Due to an interaction in the upper ToF, the particle does not leave the ToF in the same angle as it entered it. Therefore the Tracker track extrapolation into the TRD does not match the TRD signals. Shown is the projection of the particle path through the detector onto the y-z-plane of the AMS coordinate system.

modifications to the default track reconstruction method improve the extrapolation of the Tracker track into the TRD volume. The default method takes the Tracker signals of all nine layers (if present) into account. It applies different errors for each layer during the fitting process, where the signals in the two outer layers are assigned larger errors due to the residual resolution of their alignment. A track reconstruction developed in the framework of this thesis improves the matching of the track extrapolation to TRD signals and therefore improves the particle identification with the Transition Radiation Detector. In this method the same reconstruction algorithm is used as in the default Tracker method, but a possible signal in layer nine of the Tracker is ignored, since it does not add information about the particle track above the inner Tracker. In addition to the negligence of the layer nine hit, all Tracker signals are considered with the same error in the fitting algorithm. This increases the significance of a layer one measurement. If a missing signal in the TRD has been identified for the event, the reconstructed point is also added to the assortment of measurements used for the fit. As a missing signal in the TRD only has a measurement in the r- and z-coordinate by the TRD itself the third coordinate is by default determined from the Tracker track extrapolation. Therefore this third coordinate is associated with

an error sufficiently large that it does not have any impact on the fit.

Figure 5.14 shows a comparison of the number of TRD signals on the track extrapolation between the default track, a refit of the track as described in the last paragraph with only Tracker information and the refit also including TRD missing signals. For events without a Tracker plane one signal associated to the particle the gain of the new fitting method averages to about one signal more on track for every fourth event. The gain in the number of TRD signals on the track extrapolation for tracks with a plane 1 signal is about 1 additional signal per event. Adding a missing TRD signal in this case has only a minor effect, because of its worse resolution compared to the Tracker signal. Therefore the improvement in this case is largely due to the different weights in the fit compared to the default fit.

Despite the fact that the improvements in the number of hits are rather small, the TRD proton rejection shows an exponential dependence on the number of signals used for the calculation of the electron likelihood as will be shown in section 6.1. Therefore the gain achieved by the new fitting method has a strong positive impact on the TRD performance. The TRD particle separation power with this new developed method and comparisons to other available classes in the AMS software, using different alignment and tracking methods, are shown in the next chapter.
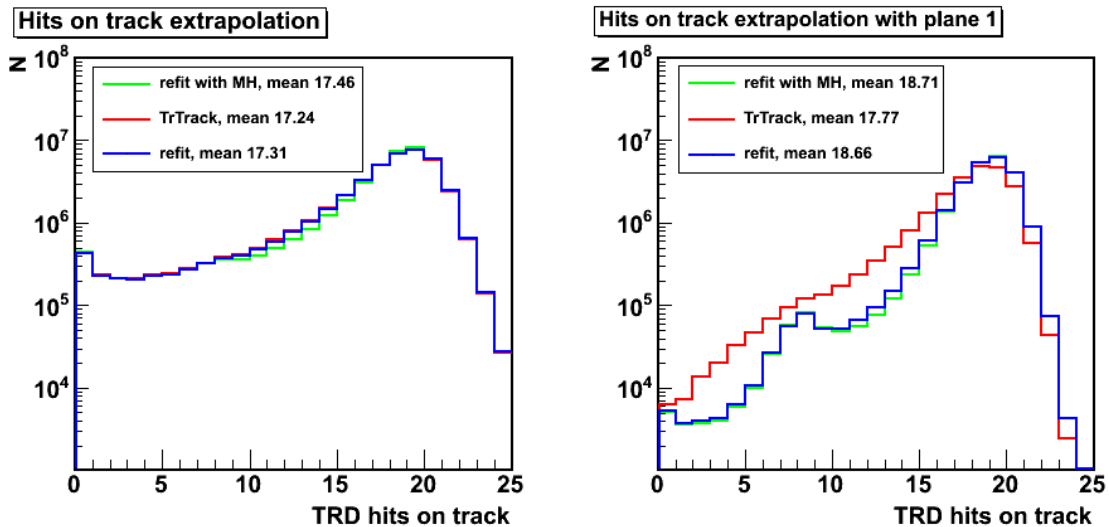
Figure 5.14.: ***Comparison of the number of TRD hits on the extrapolation of the default Tracker track, the track refit and the track refit with missing signals.*** Red: default Tracker track, blue: track fit with same weights and without plane nine, green: track refit with TRD missing hits (MH) and track hits. Left: events without a Tracker plane 1 signal, right: events with a Tracker plane 1 signal. The increase in the mean of number of TRD signals found on the track extrapolation ranges from 1 hit every fourth event for events without a Tracker plane 1 signal to 1 hit per event for tracks with a plane 1 signal.

6. Positron Proton separation

The most abundant particles in cosmic rays are protons with a rate up to 1000 times that of the positrons. As a consequence it is most important for a cosmic ray particle detector to be able to distinguish between these two particle species.

The most powerful subdetectors of AMS-02 to separate positrons from protons are the Transition Radiation Detector and the Electromagnetic Calorimeter. The TRD separates positrons from protons by the virtue of the transition radiation, as discussed in chapter 4.1.The calorimeter distinguishes the two particles by their interaction with lead as will be discussed in section 6.2. Electrons and positrons interact based on the electromagnetic force and therefore produce electromagnetic showers with a well predicted shape. Protons on the contrary interact also according to the strong force so they produce irregular hadronic showers. Another discriminating variable for the separation of positrons from protons is the comparison of the measured rigidity in the Tracker to the energy of the particle reconstructed in the ECAL.

The design goal of AMS-02 was to be able to reject protons in the positron measurement with a rate of 10^6, which would result in a purity of the positron sample of more than 99.9%. The proton rejection R_p is defined as the inverse of the misidentified proton efficiency, which is the total number of protons over the number of mistakenly identified protons as positrons:

$$R_p = \frac{N_{p^+}}{N_{p^+ \to e^+}} \tag{6.1}$$

where N_{p^+} is the total number of protons measured and $N_{p^+ \to e^+}$ is the number of protons identified as positrons.

Another way to express the cleanliness of the selection is the purity of the positron sample, which is defined as:

$$P_{e^+} = \frac{N_{e^+}}{N_{e^+} + N_{p^+ \to e^+}} \tag{6.2}$$

with N_{e^+} being the number of correctly identified positrons. An additional factor to be taken into account in the purity of the positrons is the number of electrons falsely identified as positrons due to charge confusion in the Tracker. Therefore a more correct formula for the purity of the positrons would be:

$$P_{e^+} = \frac{N_{e^+}}{N_{e^+} + N_{p^+ \to e^+} + N_{e^- \to e^+}} \tag{6.3}$$

with $N_{e^- \to e^+}$ being the number of electrons identified as positrons. Charge confusion will be taken into account for the measurement and explained in more detail in chapter 7.

In the following abundant electrons will be used to set up and evaluate the discriminating variables in the TRD and ECAL. This can be done since the intensity of transition radiation emission and energy deposit by ionisation do not depend on the sign of the charge of the particle and neither do the energy deposit and shower shape in the calorimeter.

Due to the redundant measurement capabilities of AMS-02 the proton rejection and positron purity can be obtained from data, but the retrieved proton rejection and positron purity depends on the applied event selection, e.g. on the number of TRD hits on the Tracker track extrapolation. The applied event selection is the same as used for the positron fraction analysis, which will be presented in chapter 7.

First a detailed description of the likelihood method is given, which is used to discriminate positrons from protons with the TRD. Here the performance of the TrdM likelihood is presented, which was developed in the course of this thesis and is available in the common AMS software. In section 6.2 follows the boosted decision tree (BDT), which is used to separate the particle species with the ECAL and section 6.3 describes the particle separation power of the comparison of the Tracker rigidity measurement to the reconstructed energy in the calorimeter.

6.1. Likelihood calculation with the TRD

The Transition Radiation Detector is sensitive to the Lorentz γ-factor of the particle. Since γ only depends on the mass of the particle at a fixed energy, the TRD can distinguish between particles of different mass. The probability for emission of transition radiation strongly increases at a γ-factor of the particle of more than 300 and reaches a plateau for $\gamma > 10^4$, as can be seen in figure 4.2. Naturally, this means that the TRD looses rejection power, when protons get highly relativistic so that they start to emit transition radiation as well.

The single layer energy deposits in the TRD can be seen as independent measurements of the same particle. The assumption that the single measurements are not correlated is only true to a certain extend, since the probability to detect a transition radiation photon slightly depends on the detection in above layers. The likelihood approaches used by the TrdK and TrdQt method, though, give the same quality of proton rejection as a much more complicated Neural Network, which is able to determine the correlations between the single measurements [122, 150]. From this it can be concluded that the correlations must be minor.

The likelihood of an observation is defined as:

$$\mathcal{L}(\theta|x) = P(x|\theta) \tag{6.4}$$

with x being a set of measurements and θ being a set of parameters [151]. The likelihood is a measure for the probability of a set of measurements to occur for a given set of parameters. In our case the set of measurements are the energy deposits in the TRD and the parameter is the identity of the particle. So the electron likelihood gives us an estimate how likely it is that our measurements belong to an electron. Equally the proton likelihood gives a

probability of the measured particle being a proton. We define our event electron likelihood now as the fraction of the electron likelihood compared to the sum of both likelihoods:

$$\mathcal{L}_e = \frac{P_e}{P_e + P_p} \quad \text{with} \quad P_e = \sqrt[n]{\prod_i^n P_e^i} \quad \text{and} \quad P_p = \sqrt[n]{\prod_i^n P_p^i} \,. \tag{6.5}$$

P_e^i and P_p^i are the probability densities of the individual signal amplitudes in the TRD. The geometric mean of the single straw tube measurements is built to combine the measurements of each layer to a prediction for the detected particle. Using the logarithm of the likelihood rather than the likelihood value itself does not change the maximum of the distribution, since the logarithm is a monotonically rising function, but improves the handling. Therefore the so called log-likelihood is used as the discriminating variable of the TRD. In the following the log-likelihood will be referred to as likelihood for the sake of convenience.

The single tube probabilities for being electron- and proton-like are retrieved by comparing the signal amplitude in the straw tube after gain correction to the typical amplitude distributions, the so-called probability density functions (PDFs), for both particle hypotheses. The signal in the TRD depends on the following quantities:

- xenon partial pressure

- length of the particle path in the straw tube

- rigidity of the particle

- layer of the TRD.

The PDFs either need to be parametrized as functions of these parameters, as they are in the TrdK method, or sets of PDFs are needed that cover the possible parameter range. The latter approach is used in the TrdQt method, with 6 sets of PDFs for different xenon pressures, 30 sets of proton PDFs for different rigidities and 20 sets of electron PDFs for the different TRD layers. The PDFs of the TrdQt class are set up as functions of energy deposit per distance travelled through the straw tube, because the signal is proportional to the particle path length as explained in section 4.6. Therefore the TRD signals need to be normalized in path length before compared to the PDFs. The dependency of the PDFs on the signal layer of the TRD take into account the small correlations of emission and detection of transition radiation in the different layers.

In the likelihood method called the TrdM method, which was set up as part of this thesis and is available in the common AMS software, the PDF parametrization of the TrdK class has been incorporated. The difference between the TrdK and TrdM method are the different alignments and track reconstructions used. In figure 6.1 the electron and proton PDFs are shown for a TRD signal in the bottom detector layer by a particle of 100 GV rigidity, traversing the tube with a path length of 0.6 cm, and the TRD being operated at a xenon partial pressure of 0.95 bar.
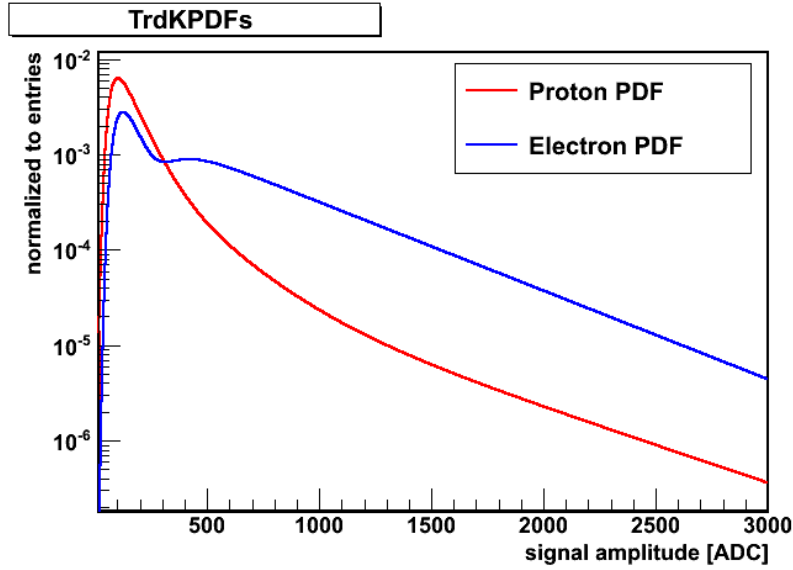
Figure 6.1.: ***Example of TrdK PDFs for electrons and protons.*** Red: protons, blue: electrons. The PDF has been set up for a TRD signal in the bottom layer by a particle of 100 GV rigidity, having a path length of 0.6 cm, and the TRD having a xenon partial pressure of 0.95 bar.

The path length of the particle in each straw tube is calculated as the 3D intersection of the track refit extrapolation, which was introduced in the last chapter, and the 3 mm radius cylinder around the aligned straw tubes wires. The time dependent gain correction is also taken from the TrdK method, which is done similar to the described method in chapter 4 based on the MPV of the proton signal distribution, but also taking the tails of the distribution into account. The xenon pressure is taken from a database, which is filled with the time dependent partial xenon pressures. The partial pressure is not measured in the TRD but it is reconstructed based on the amounts of gas transferred into the detector during the refills and the measured total gas losses with time. The gain corrected amplitude together with the parametrization factors are passed to functions, which return the single hit electron and proton probability. The electron likelihood of the particle is then calculated according to equation 6.5. The different distributions of $-log(\mathcal{L}_e)$ for protons and electrons of energy 31 GeV to 38.36 GeV are shown in figure 6.2.

A cut-off point in the likelihood can be defined by demanding a certain signal efficiency, which here corresponds to the positron efficiency ϵ_{e+}, which is defined as:

$$\epsilon_{e+} = \frac{N_{e+}^{L_e < \text{cut}}}{N_{e+}}.$$ (6.6)

The rejection is then calculated according to equation 6.1, with falsely identified protons being protons having $L_e < \text{cut}$.

As already mentioned in chapters 4 and 5 the rejection power of the TRD strongly
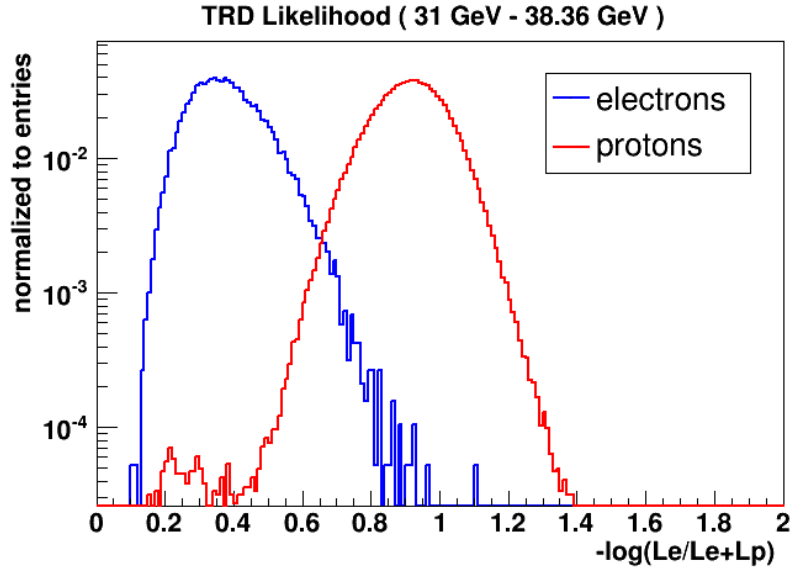
Figure 6.2.: ***Distribution of log-likelihood for electrons and protons with an energy between 30 GeV and 38.36 GeV.*** Red: protons, blue: electrons. In the proton likelihood distribution a contamination at low likelihood values is visible. Nuclei fragmenting in the upper part of the detector may be reconstructed as particles with unity charge by ToF and inner Tracker and defined as protons by the calorimeter, while the higher ionisation signal in the TRD, which consequently leads to a low likelihood value, clearly identifies them as particles with $Z > 1$ or multiple particles in coincidence.

depends on the number of hits used for the calculation of the electron likelihood. This dependency is presented in figure 6.3.

The particle separation with the TRD is based on the emission of transition radiation. The probability of emission depends on the particles γ-factor as does the ionisation signal due to its dependency on $\beta = v/c$. Both effects lead to a decrease of the discrimination power with increasing proton energy, the higher γ-factor of the protons dominating the decrease though. The proton rejection as aa function of energy for all three available likelihood methods in the AMS software for a 90 % signal efficiency are shown in 6.4.

The TRD proton rejection decreases for high energies, since protons start to emit transition radiation, while electrons have long reached the plateau, shown in figure 4.2 and therefore do not emit additional transition radiation photons. The decrease in discrimination power for small particle energies is due to worse track extrapolation for low rigidity particles. They undergo multiple scattering with larger scattering angles, see equation 5.2, which results in smaller number of found TRD hits on the track and poorer path length determination.
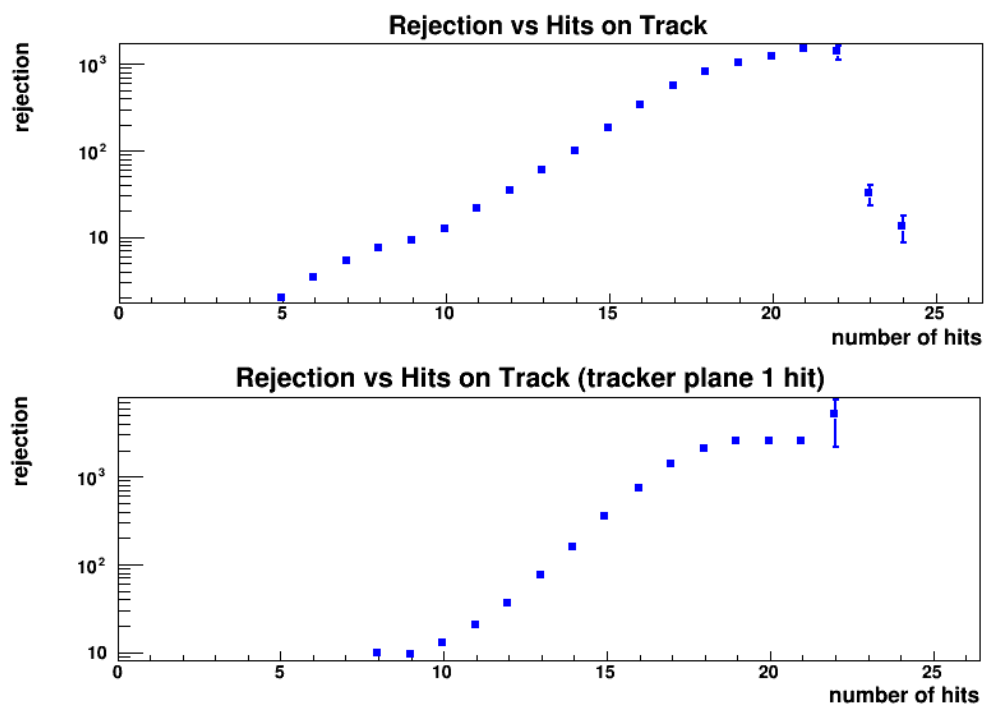
Figure 6.3.: ***Dependency of the TRD proton rejection on the number of signals used for the calculation.*** In the top plot the dependency is shown for events without a Tracker plane 1 signal and in the bottom histogram for events with a Tracker plane 1 signal. Tracks with more than 20 signals have a larger θ-angle, which leads to a higher rejection due to more traversed radiator material.
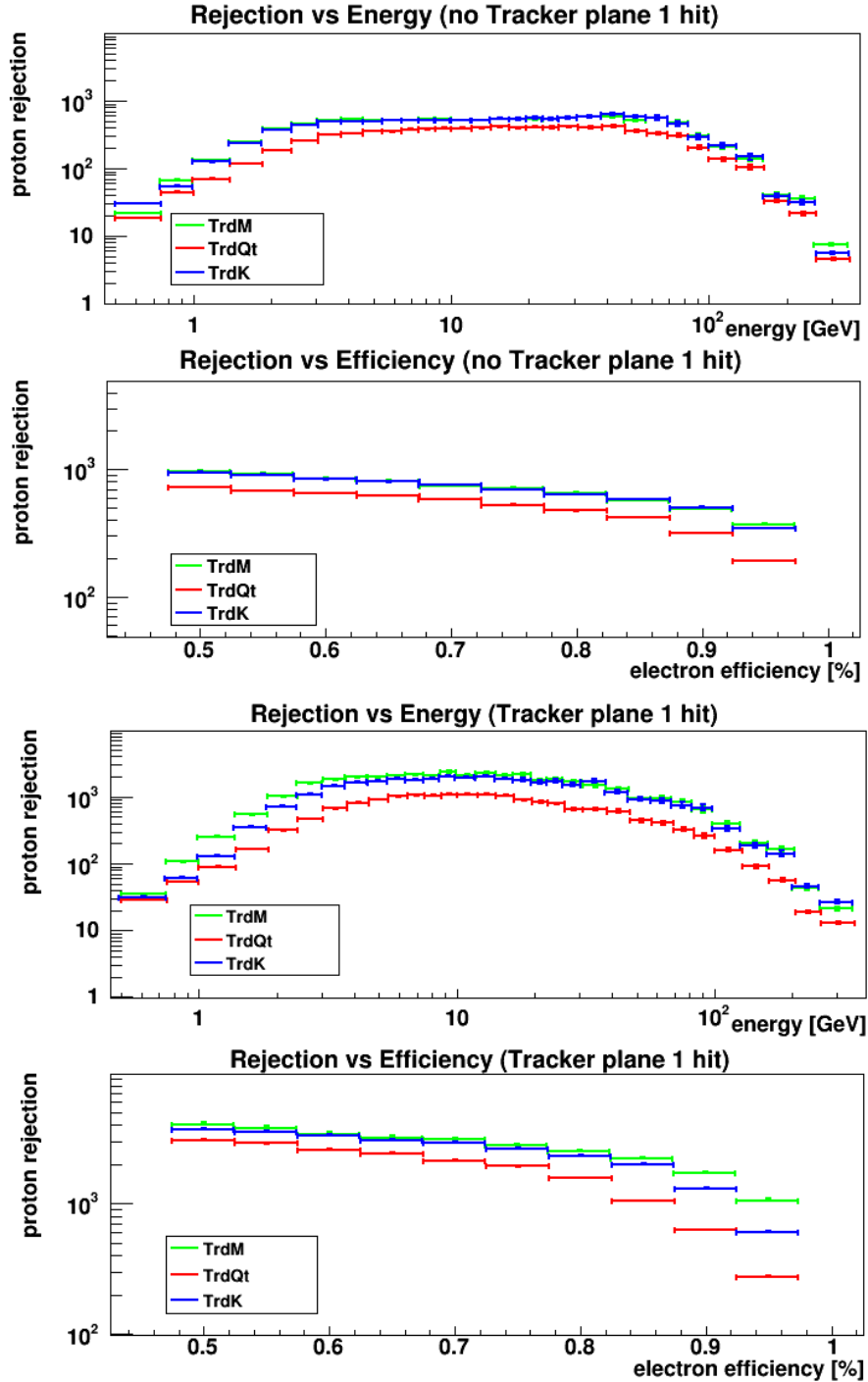
Figure 6.4.: ***Dependency of the proton rejection on the energy of the particle and the signal efficiency.*** In the two top plots the different proton rejections for particles having a Tracker track with no signal on Tracker plane 1 and on in the two bottom plots the particles with a signal in the Tracker plane 1 are shown. The upper plots show the proton rejection as a function of particle energy at 90 % signal efficiency, while the lower plots show the proton rejection as a function of signal efficiency averaged over the whole rigidity range. TrdM: green, TrdQt: red, TrdK: blue.

6. Positron Proton separation

The relative deviation of both the TrdK and TrdQt method compared to the TrdM method are shown in figure 6.5.
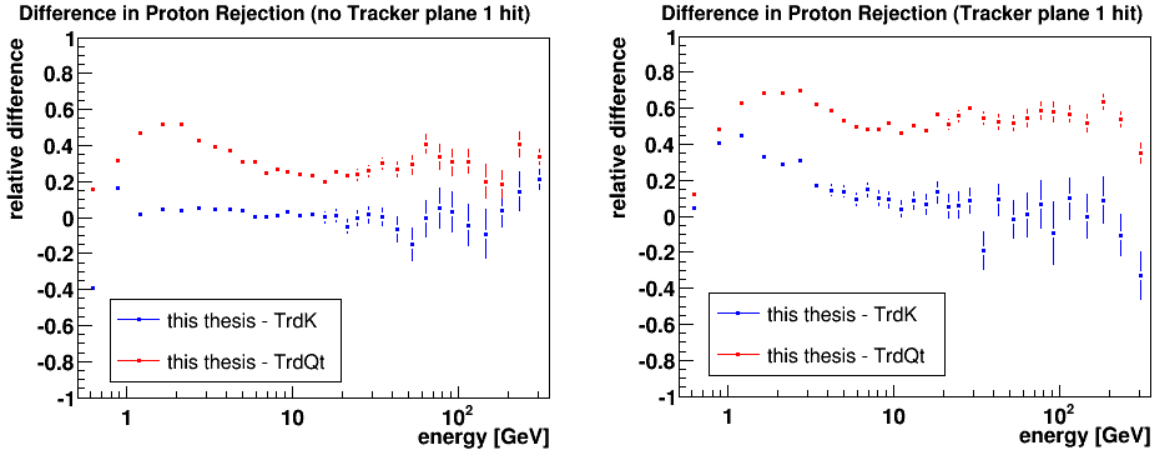
Figure 6.5.: **Relative comparison between the different TRD likelihood methods.** On the left the proton rejection for events without a Tracker plane 1 signal retrieved by the TrdK and TrdQt method is set in relation to the likelihood of the TrdM method as $\Delta R = \frac{R_{TrdM} - R_{Trdx}}{R_{TrdM}}$. The right plot shows the same comparison for events with a Tracker plane 1 signal.

Only events for which all three methods used more than 12 TRD signals for the calculation of the likelihood were used in order to have a fair comparison. The proton rejection of the TrdM method exceeds the one of the TrdQt method by 30-70%, which is traceable to the different ways the PDFs of the methods have been defined. The parametrization of the TrdK PDFs, which is also used within the TrdM method, seems to give better probability estimates, than the set of PDFs used in the TrdQt method. The TrdM method shows an improvement of up to 40% compared to the TrdK method for low energies, if the Tracker track includes a signal on the Tracker plane 1, which occurs roughly for every other track mainly due to the size of the Tracker plane 1. Integrating over the full energy range the improvement is also in the order of 40%, as low energies dominate the particle fluxes. The track refitting, as described in the last chapter, increases the number of hits on the track extrapolation and leads to better path length determinations, which results in a better discrimination of the different particle types.

The positron purity retrieved by the TrdM likelihood method with a 90% electron efficiency can be seen in figure 6.6.

The purity has been evaluated by a template fit of the distribution of the EcalBDT, which will be described in the next section, while the particles have been defined by a cut on the TRD likelihood. The templates for the fit are defined from data. The EcalBDT distribution of selected electrons defines the signal template and the protons built the background template. Both contributions are fitted to the positron distribution and as a result the positron purity is obtained. The template fitting method will be explained in
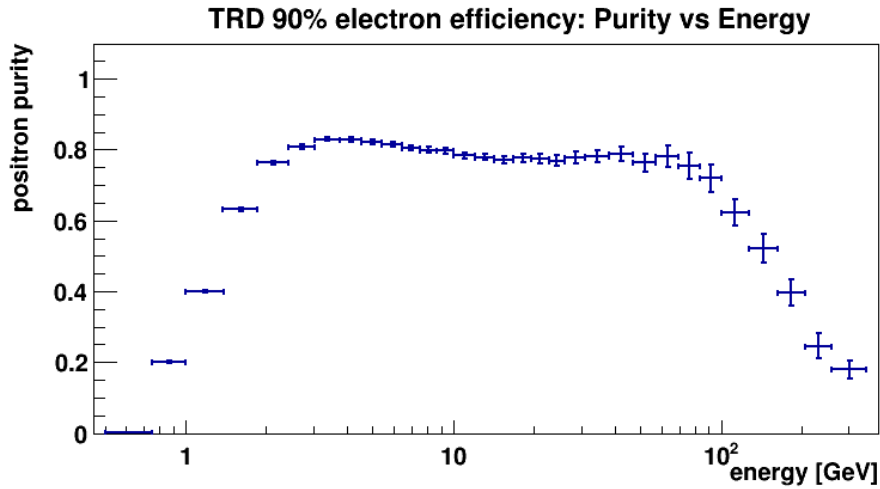
Figure 6.6.: ***Positron purity achieved with the TrdM likelihood at 90 % electron efficiency.*** The purity has been determined by a template fit of the EcalBDT distribution of positrons, which were selected with the TRD ass shown in figure 6.7.

detail in section 7.2, where a template fit of the TRD likelihood is used to determine the proton background for the positron fraction analysis. The fit result for the energy bin from 31 Gev to 38.36 GeV is shown in figure 6.7.
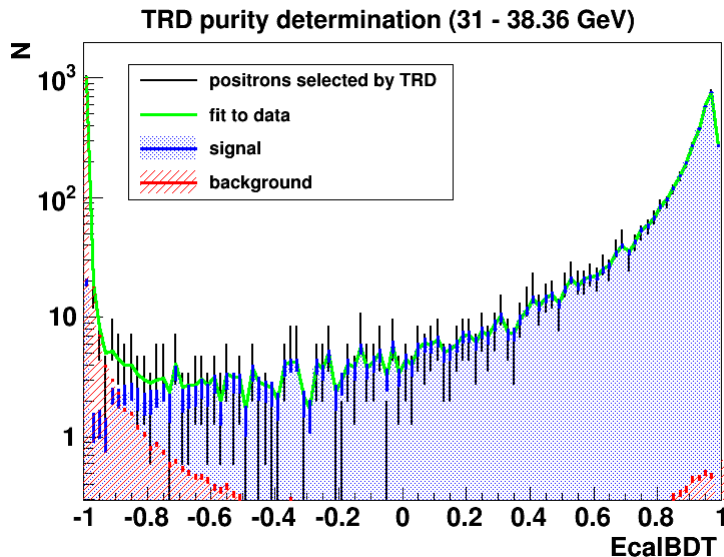
Figure 6.7.: ***Template fit to determine the positron purity of the TRD selection*** The EcalBDT distribution of the identified positrons is fitted with templates for signal (electrons) and background (protons) defined by the TRD.

The proton rejection and positron purity achieved with the TRD are stated in terms of particle energy reconstructed by ECAL rather than particle rigidity, although the TRD likelihood is only depending on the particle rigidity. The following analysis of leptons, though, is based on an ECAL and TRD approach, which makes the ECAL energy the proper variable. For a proton interacting in the ECAL, the reconstructed energy represents on average half of the proton rigidity. From this follows that the TRD proton rejection already decreases at energies around 100 GeV, as protons with rigidity > 200 GV fall into this energy bin, which already start to emit transition radiation in considerable amounts.

6.2. Boosted decision tree for the ECAL

The AMS-02 Electromagnetic Calorimeter, already introduced in section 3.2, is a lead block interlaced with scintillating fibres, which resembles 17 radiation lengths. It consists of 9 superlayers which are stacked alternating with parallel orientation to the x- and y-axis. This allows a 3-D reconstruction of the induced interactions by the incident particle. For positrons these interactions are mainly pair production and bremsstrahlung until the energy of the secondary particles reaches the critical energy of $\sim$7 MeV in lead and they are absorbed by ionisation. The critical energy is defined as the point at which energy losses from ionisation and excitation equal the energy losses from bremsstrahlung [140]. Protons always leave a trail by ionisation in the calorimeter. With a probability of about 50 %, a proton also induces a hadronic shower by nuclear interaction. Such showers have an electromagnetic component from the decay of created neutral pions to photons and a hadronic component. In a hadronic shower a large component of the energy of the primary particle is passed to secondary particles, which results in a wide spread of the shower and an irregular shape. The typical shape of an electromagnetic and a hadronic shower can be seen in figure 6.8 [152].
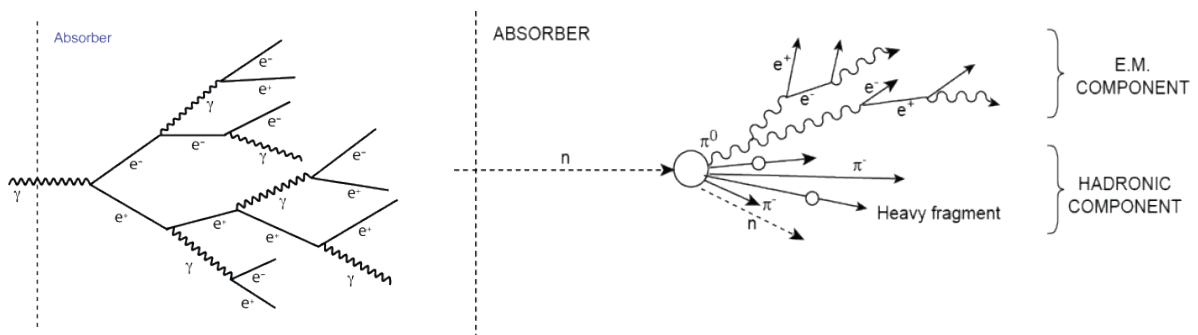
Figure 6.8.: ***Typical shower development of electromagnetic and hadronic showers.***
Left: electromagnetic shower, right: hadronic shower [152].

To unite the different shower parameters to a single discriminating variable for the calorimeter a multi-variant-analysis in form of a boosted decision tree (BDT) has been

set up by the INFN PISA group of AMS. The logic of a BDT is displayed in figure 6.9.
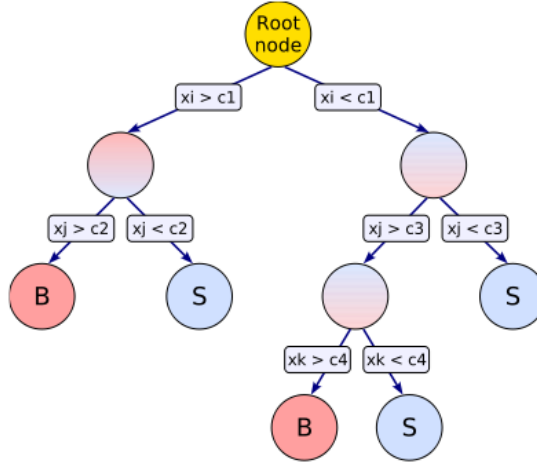
Figure 6.9.: ***Scheme of a decision tree for signal and background identification.*** The layout of the branches of the BDT is set up in the training of the BDT, as are the cut values c1, c2, c3, c4. The $x_{i,j,k}$ represent the input variables. [153]

A boosted decision tree needs to be trained on a clean sample of signal and background events, to learn the typical differences in the variable distributions of both topologies. The training defines the layout and associated cut criteria of each branch. To ensure that the BDT is not over-trained, which means that the decision tree learns specific characteristics of the used training sample rather than just the typical distributions of the variables for signal and background, a test sample is left out of the training, on which the performance is tested afterwards.

In order to be able to use real data for the training of the BDT rather than Monte Carlo events, the redundancy of the particle identification with AMS-02 is exploited. The samples for signal and background, being electrons and protons in this case, were selected using the TRD. To improve the performance of the BDT, multiple trainings were done in nine different intervals of deposited energy. Due to small statistics in the high energy region also data accumulated during the test beam at the Super-Proton-Synchrotron were used.

The variables used to built the EcalBDT include:

- fraction of total deposited energy in the first 2 layers

- energy deposited in the first 2 layers

- fraction of total deposited energy in the last 2 layers

- layer number in which the center of gravity of the shower is contained

- σ(energy deposit per layer)

- fraction of total deposited energy in 3 cm radius around shower axis

- fraction of total deposited energy in 5 cm radius around shower axis.

The EcalBDT classifier distributions for electrons and protons in the energy interval between 31 GeV to 38.36 GeV are shown in figure 6.10.
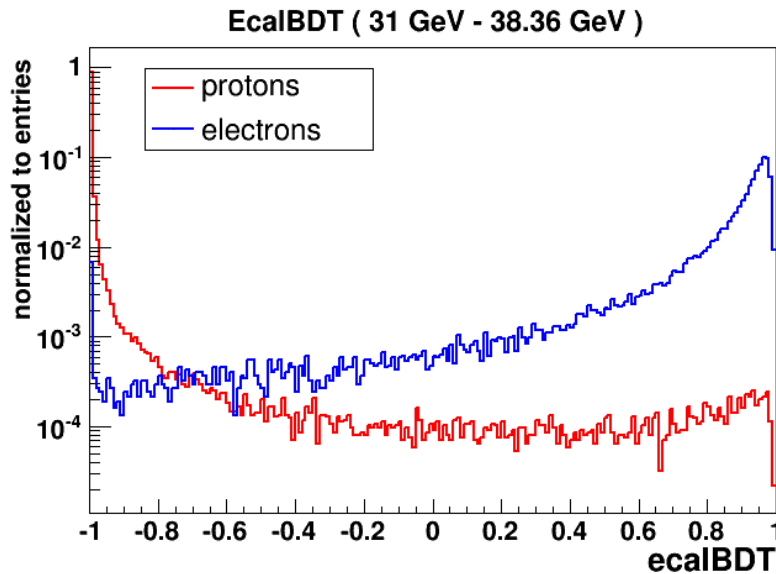
Figure 6.10.: ***EcalBDT classifier distributions for electrons and positrons.*** Red: protons, blue: electrons. The electron and proton samples were selected with the TRD. The peak in the signal distribution at -1 is due to wrong particle identification with the TRD or interactions in the detector, which were also visible for the TRD likelihood in figure 6.2.

The background in the electron sample, of which the majority falls into the dominant lowest BDT bin, is partly due to the finite proton rejection of the TRD used for the particle identification in this case. Although the proton rejection is good enough for rejecting the abundant antiprotons in the negative sample, protons reconstructed with the wrong charge sign dominate over the antiprotons and lead to a small residual contamination.

The proton rejection of the EcalBDT as function of energy can be seen in figure 6.11.

The proton rejection with the EcalBDT shows a feature around 70 GeV, which might be due to the energy intervals of the training of the boosted decision tree, since at this energy the transition between two trainings occurs. The BDT performs worse on the upper edges of a training bin, than on the lower edge, because the lower edge has a higher significance in the training as it dominates the statistics in the bin.
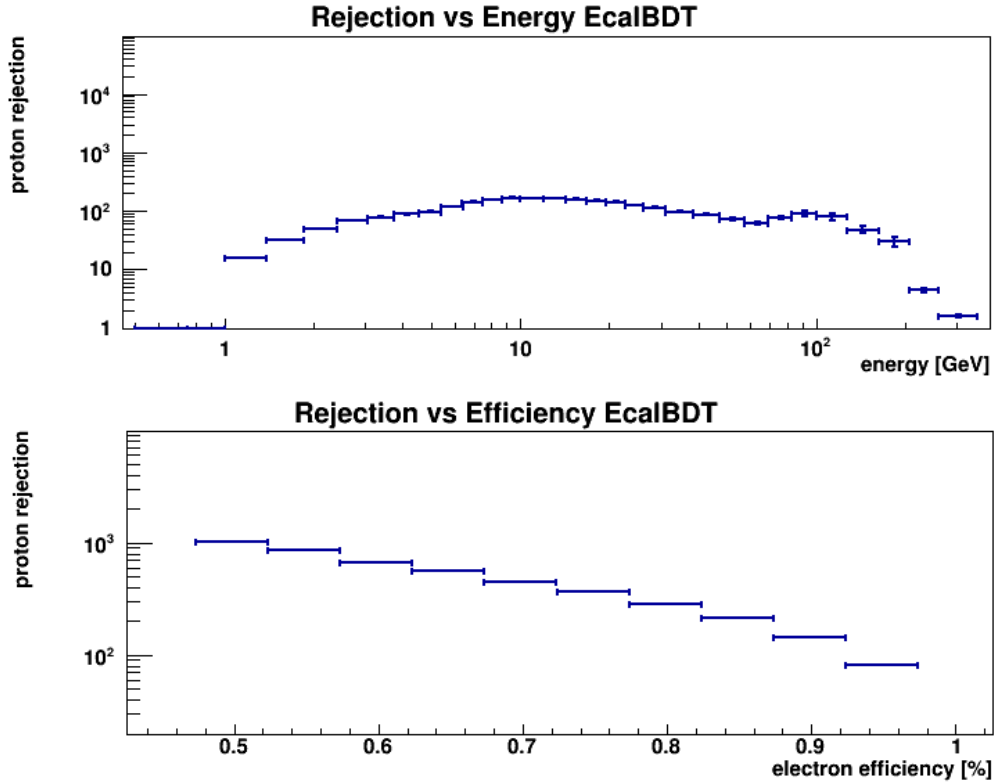
Figure 6.11.: **Proton rejection achieved with the EcalBDT at 90% electron efficiency.** In the top plot the proton rejection according to energy for a 90% electron efficiency cut is shown. The lower plot illustrates the ECAL proton rejection for different selection efficiencies summing over the whole energy range, which leads to an average electron energy around 8 GeV.

6.3. Energy to rigidity ratio

Another way to exploit the proton rejection power of the calorimeter is comparing its energy measurement with the rigidity measurement of the Tracker. Electrons, positrons and photons usually deposit their total energy in the calorimeter, so one expects $E/R \sim 1$. Even in case that the electromagnetic shower leaks out of the detector, energy corrections can be calculated given their continuous shape. Protons only deposit small amounts of energy by ionisation if they do not undergo a nuclear interaction. If they initiate a hadronic shower, the shower starts on average deeper in the calorimeter than electromagnetic showers and since also the mean free path of the secondary particle is large, the showers tend to have large leakages out of the detector. In this case the leakage corrections do not reconstruct the correct energy of the incident particle, as they were optimized for electromagnetic shower shapes. Therefore $E/R \ll 1$ for most hadrons.

Distributions of E/R for both particle species selected with the TRD, at energies between 31 GeV and 38.36 GeV are shown in figure 6.12.
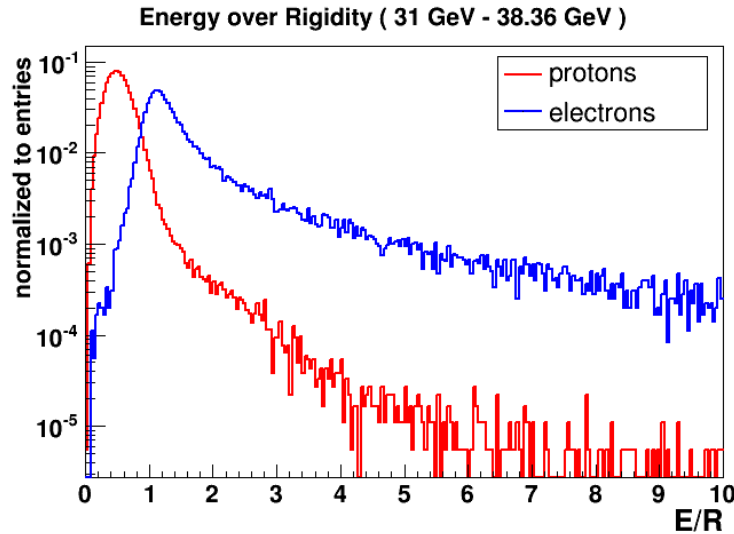
Figure 6.12.: **Energy to rigidity ratio distributions for electrons and positrons.** Red: protons, blue: electrons. The samples were selected with the TRD.

Combining the rejection power of the EcalBDT with the one achieved by the E/R ratio, by applying sequential cuts on both variables, a proton rejection of $\sim 5 \cdot 10^3$ and positron purity of $\sim 85\%$, as displayed in figures 6.13 and 6.14, are obtained for a 90% electron efficiency.

As the TRD purity has been checked by a fit to the EcalBDT, the ECAL and Tracker purity presented in figure 6.14 has likewise been determined by a template fit of the TRD likelihood with particle samples defined by a cut on EcalBDT and E/R.

The result of the fit for the energy bin from 31 GeV to 38.38 GeV is shown in figure 6.15.

TRD and ECAL have their best positron-proton discrimination powers in slightly different energy regions, as can be seen from figures 6.6 and 6.14. For an analysis of high energetic positrons the combined rejection power of both detectors is needed. In order to achieve a positron purity above 99%, or alternatively determine the residual proton contamination with a high accuracy, all three discriminating variables need to be used.

The determination of the proton rejection from data might lead to an underestimation of the discrimination power. Depending on the energy there are residual backgrounds in the samples selected by only TRD or only ECAL. These naturally lead to a lower rejection value of the single detectors in comparison to clean samples. Therefore the quoted numbers are only lower limits. In order to get a flat rejection over the full energy range, the proton rejection at low and high energies can be increased by reducing the electron efficiency, as can be seen in figures 6.4 and 6.13.

The overall AMS proton rejection is the product of the TRD and ECAL proton rejection, since both detectors can be assumed to be independent from one another. The resulting proton rejection of AMS-02, obtained by sequential buts on all three discriminating variables, for 80% electron efficiency of in the order of $10^5 - 10^6$ for intermediate energies, which
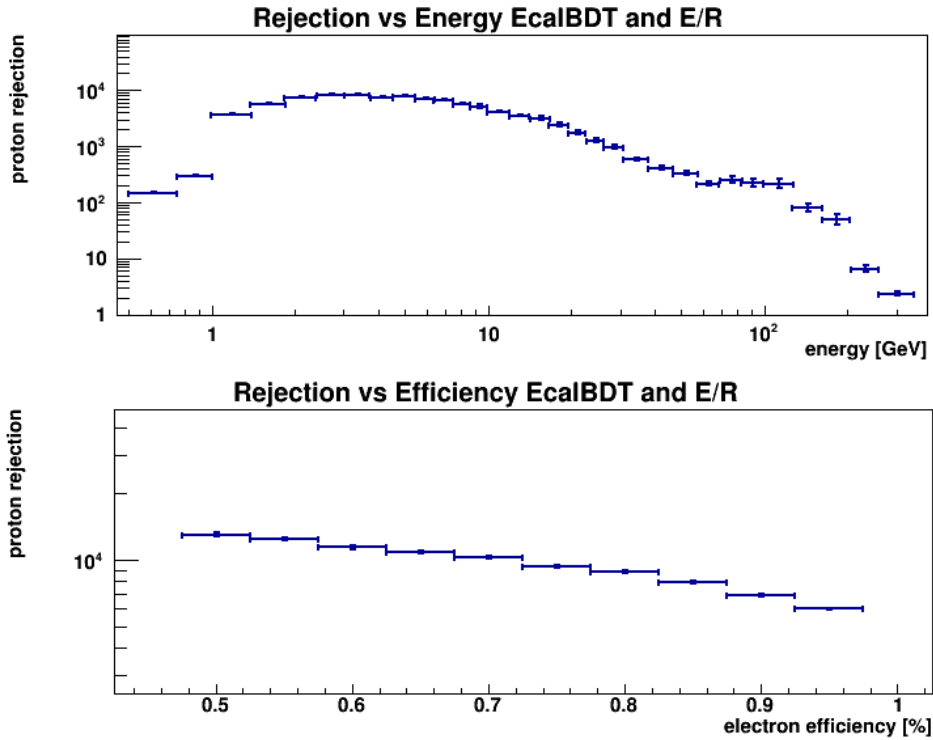
Figure 6.13.: ***Proton rejection achieved with ECAL and Tracker.*** The proton rejection of the combination of the EcalBDT and the matching of ECAL energy to Tracker rigidity according to energy or signal efficiency are shown. For the dependency of the proton rejection on the energy a signal efficiency of 90% was chosen, for the dependency on the signal efficiency a summation of all energies is done.

is sufficient to suppress the highly abundant protons in the positron fraction analysis. At high and low energies the electron efficiency can be reduced to obtain such rejections. However, a too high rejection is not always beneficial, e.g. if one wants to determine the background from template fits, as discussed in the next chapter.
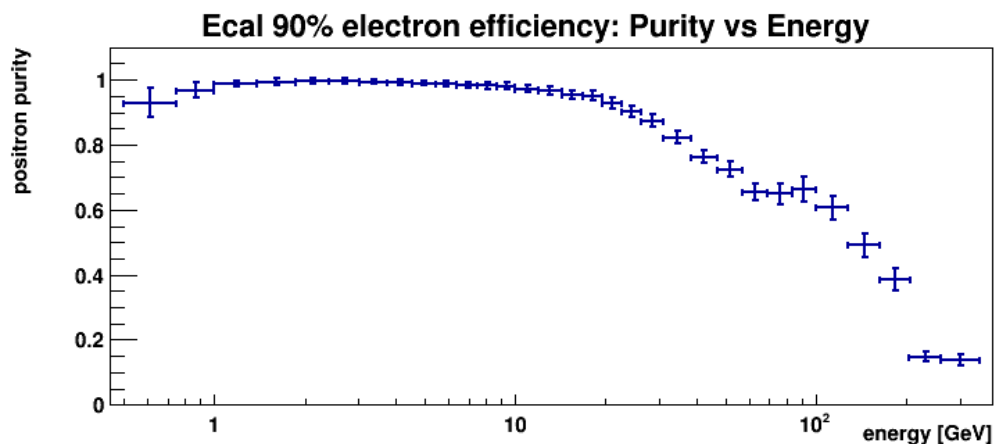
Figure 6.14.: **Positron purity achieved with ECAL and Tracker at 90% electron efficiency.** The purity is determined by a template fit of the positron TRD likelihood distribution, with templates and positrons selected with ECAL.
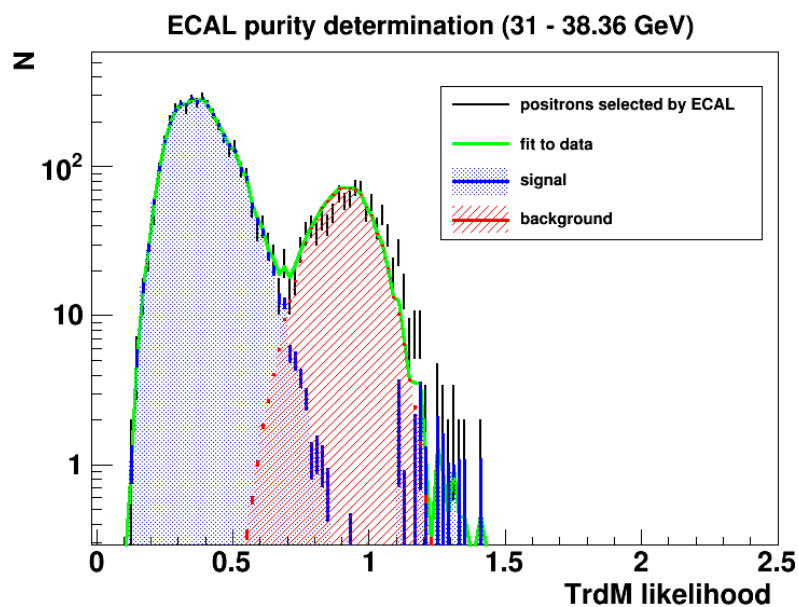
Figure 6.15.: **Template fit to determine the positron purity of the ECAL selection.** The TrdM likelihood distribution of the identified positrons is fitted with templates for signal (electrons) and background (protons) defined by ECAL.

7. Positron fraction

The flux of high energy positrons, assuming them to be purely secondaries, should fall more steeply than the flux of electrons [50]. This would lead to a falling slope of the positron fraction towards high energies. What has been observed by previous experiments, for example by PAMELA as shown in 2.9, is indeed a rise in the positron fraction towards higher energies, suggesting that there must be other processes producing positrons than just interaction of primaries with the cosmic interstellar medium.

As discussed in section 2.2, Pulsars or WIMP annihilation could give rise to an increasing positron fraction. In the following a method is presented to determine the positron fraction with AMS-02 from 0.5 GeV up to energies of 350 GeV.

The results obtained by this method agree with the officially published result [154]. Unlike the official AMS-02 analysis, though, this method does not rely heavily on Monte Carlo. In the published analysis a two dimensional template fit in the TRD likelihood - E/R plane is performed to simultaneously estimate the residual background of protons and charge confused electrons in the positron sample, preselected with the EcalBDT. This is possible, since the E/R-ratio is sensitive to charge confusion as will be discussed in section 7.2. The templates for this fit are obtained from MC, as the true charge sign needs to be known.

The analysis presented in the following instead follows a more data driven approach. A one dimensional fit in the TRD likelihood distribution is used to determine the proton background in the positron sample, which is selected with energy dependent cuts on EcalBDT and E/R. The templates for this fit can be obtained from data. The selected electrons are used to set up the signal template, while the background template is produced from selected protons. The cut on E/R together with additional quality cuts is applied to strongly reduce the amount of charge confused electrons in the positron sample. The residual contamination is then evaluated with electron MC. The only detector simulation coming into play in this analysis is the Tracker MC, whereas the official analysis also relies on the simulation of TRD and ECAL. As the correct simulation of transition radiation is difficult, a fine-tuning of the TRD MC is needed. Therefore the use of TRD MC was avoided in this analysis. The independent identification mechanisms in TRD and ECAL allow a robust data driven analysis, which can be extended to even higher energies than presented in the following, when sufficient statistics become available.

First the event selection is established, for which it is crucial to ensure equal efficiencies and acceptances for positrons and electrons. In the second step the estimation and elimination of the different backgrounds coming from charge confused electrons and wrong identified protons is performed. In addition to the error on the measurement due to statis-

tics in the event sample and the background elimination, the systematic error due to the applied particle identification cuts is described before finally the results of the positron fraction of this analysis are presented.

7.1. Event selection and particle identification

The event selection can be split into three parts. The first set of requirements concerns the good reconstruction of the event, while the second set of cuts is applied on the reconstructed particles. The third set of cuts optimizes the event selection for the lepton identification. Any applied selection must be chosen in such a way that it does not affect positrons and electrons differently. The benefits of calculating the positron fraction, instead of separate fluxes of the leptons, are: no need to correct for acceptance, exposure time and efficiencies. But this only holds true as long as the applied cuts are independent of the charge sign of the particle. The preselection is common to most AMS-02 lepton analyses and has in large parts been developed in the framework of this thesis.

The selection criteria applied on the event basis are the following:

- check no error flag set during event assembly on board

- check no error flag set during event reconstruction

- check for existence of reconstructed elements:
    - level 1 trigger, containing all information about the trigger to the event
    - DAQ event, containing information about the data acquisition chain
    - event header, containing general information about the data taking run and the current position of AMS-02

The first two checks are naturally independent of the detected particle species and necessary to be able to trust in the reconstructed values. The demanded reconstructed elements are always present as long as no error occurred during the reconstruction algorithm or the data recording. Therefore they just reinforce the check on the usability of the event. The second set of preselection criteria addresses the usability of the reconstructed particles for a lepton analysis and are applied sequentially, namely:

- demand for existence of reconstructed elements belonging to a particle:
    - ToF beta
    - Tracker track
    - ECAL shower

    These cuts represent a cut on the geometrical acceptance of the detectors as well as on the reconstruction of the corresponding event element.

- reconstructed particle path does not point at the ISS solar arrays
  This requirement is set to avoid analysing secondaries produced in an interaction of a primary cosmic ray particle with the material of the solar arrays. In addition the applied function removes particles traversing the detector from bottom to top.

- ToF β between $+0.8$ and $+1.2$
  This cut selects only particles, which have a reasonable velocity reconstructed for electrons and positrons. The distribution of the reconstructed β by the Time-of-Flight detector is displayed in figure 7.1.
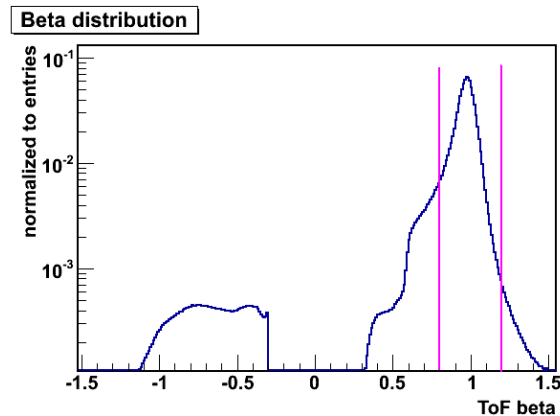
Figure 7.1.: **ToF reconstructed β distribution.** Only particles with $0.8 < \beta < 1.2$ are selected for further analysis. The peak at negative beta values corresponds to particles traversing the detector from bottom to top.

- Tracker track extrapolation is fully contained in the calorimeter and does not enter and exit the calorimeter in the boarder cell
  A particle leaving or entering the calorimeter from the side as well as particles passing the calorimeter from top to bottom all in the bordering cell of the detector, would have too large energy leakage out of the side of the calorimeter, which is not corrected properly and therefore those particles are rejected. The distribution of the extrapolation of the tracks that fulfil the previous mentioned cuts, to the ECAL top and bottom layer are shown in figure 7.2.

- Tracker track extrapolation to center of gravity of calorimeter shower is less than one cell away from the shower axis in the non-bending direction and less than two cells away in the bending direction
  This ensures the correct association of shower and track to the same particle. The allowance in the bending direction is larger than in the non-bending direction, because bremsstrahlung-photons emitted by electrons and positrons in the Tracker can enlarge the electromagnetic shower and slightly distort its shape. The loss of energy along the passage of the particle through the detector can also worsen the track extrapolation accuracy. For equal impacts on electrons and positrons the cut is symmetric, since
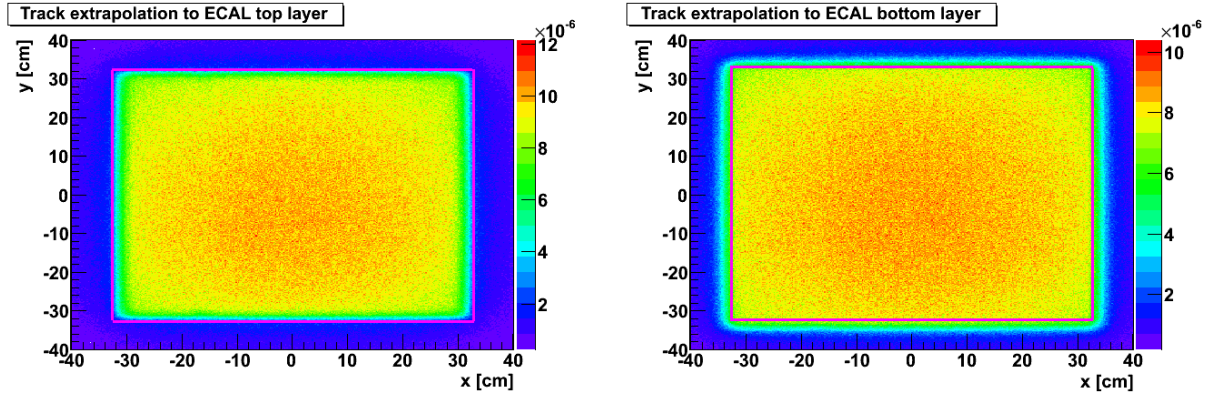
Figure 7.2.: **Track extrapolation distribution to ECAL top and bottom layers.** Left: ECAL top layer, right: ECAL bottom layer. Particles with a track passing through ECAL all the way in a border cell are disregarded.

electrons and positrons are deflected in opposite directions in the Magnet than and therefore have the tail in the distribution of the difference between track extrapolation and shower axis in opposite directions. The distribution is shown in figure 7.3.
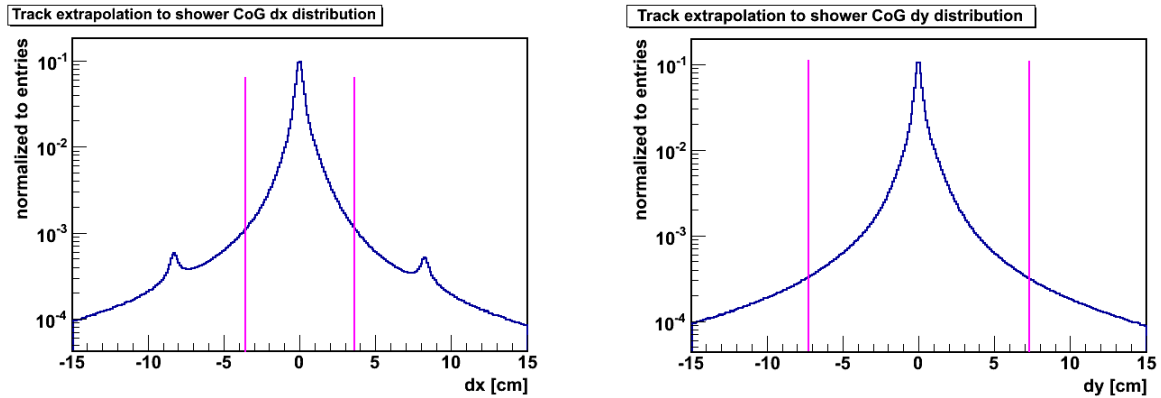
Figure 7.3.: **Distribution of the matching between Tracker track extrapolation and ECAL shower at ECAL shower center of gravity.** Left: non-bending direction, right: bending direction. Only particles with a difference less than one cell in the non-bending and less than two cells in the bending direction are further considered.

- more than six TRD signals reconstructed
  The demand for more than 6 reconstructed TRD signals increases the probability of the particle traversing a reasonable amount of TRD layers, while keeping a high efficiency in the preselection.

For an event to fulfil the preselection, being the combination of the first two selection steps, the basic reconstruction cuts have to be passed and it must contain exactly one
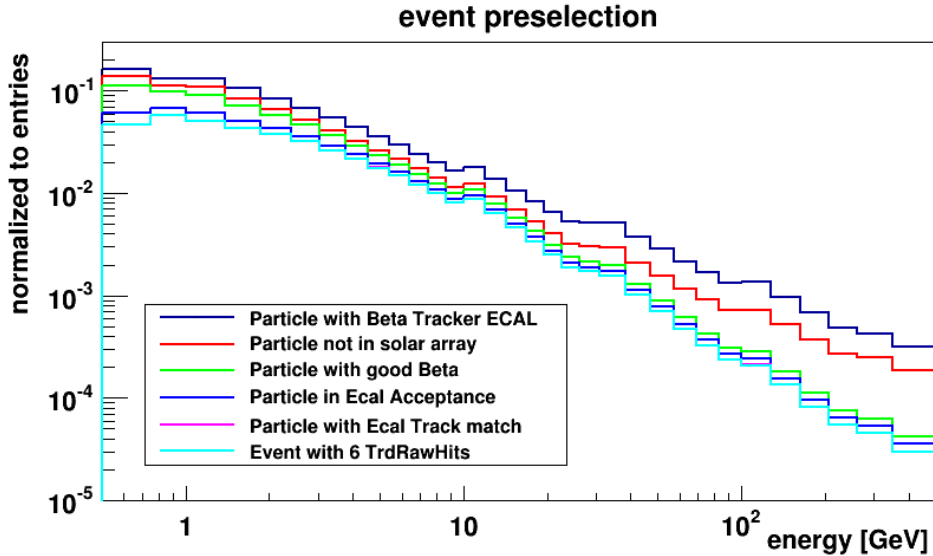
Figure 7.4.: ***Energy dependent preselection efficiency.*** The TRD raw hit cut has an efficiency close to 1, as aa consequence it overlays the Tracker ECAL matching curve. The overall preselection efficiency is 41 %.

reconstructed particle passing all quality cuts above. The energy dependent effects of the above mentioned selection cuts on the number of selected particles are shown in figure 7.4 starting from particles having all needed elements reconstructed, so that their energy can be determined.

For an optimal reconstruction of the particle properties and in order to filter out particle types that are not considered in this analysis further selection cuts are applied as follows:

- ECAL reconstructed particle energy > maximal geomagnetic cut-off[1]
  The maximal geomagnetic cut-off is defined as the maximum of the positive and negative geomagnetic cut-off calculated for the whole field of view of the detector. It is considered with a safety factor of 1.25 with respect to the nominal value and shown as a function of the geodetic longitude and latitude of the detector in figure 7.5.

- Tracker reconstructed magnitude of charge between 0.8 and 1.4
  This cut selects only particles with a charge reconstructed by the Tracker compatible with one. The distribution of the Tracker reconstructed charge is shown in figure 7.6.

- ToF reconstructed magnitude of charge between 0.8 and 1.4
  The ToF charge reconstruction algorithm is more sensitive to multiple particle events.

---

[1]The geomagnetic cut-off is determined by the strength of Earth's magnetic field in such a way that only particles above the cut-off are energetic enough to penetrate the magnetic field and reach the detector [155].
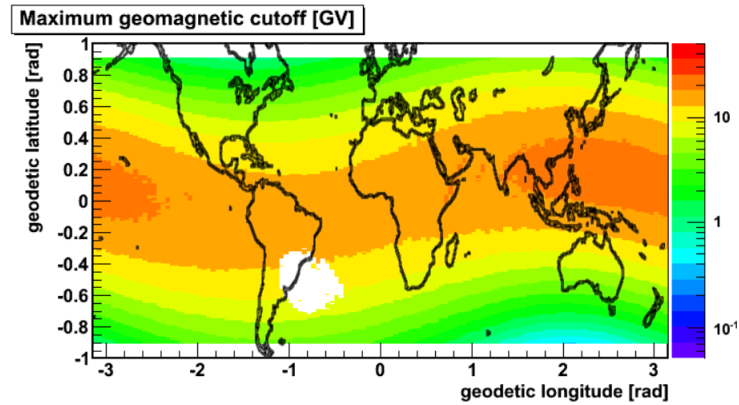
Figure 7.5.: **Geomagnetic cut-off according to geodetic coordinates.** To be confident to only analyse primary particles, a safety margin of 25% is used on top of the given cut-off value.
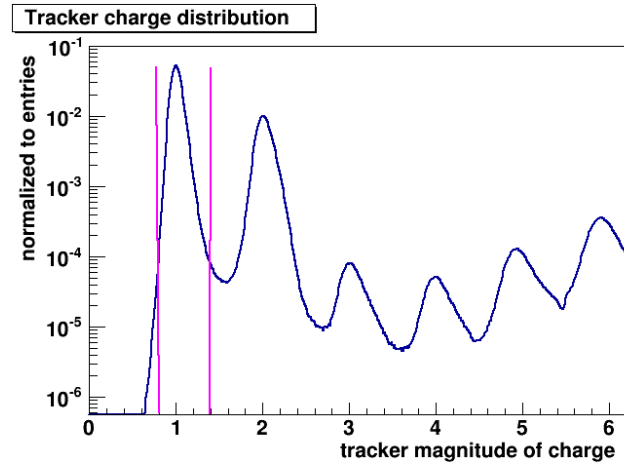
Figure 7.6.: **Tracker reconstructed magnitude of charge for preselected events.** Reconstructed values between 0.8 and 1.4 are considered to be compatible with unitary charged particles.

Therefore this cut removes undesired interactions and reinforces the Tracker charge cut. The distribution of the ToF reconstructed charge after the Tracker charge cut has been applied is shown in figure 7.7.

- Tracker track normalized χ^2 in the bending direction < 10
  By demanding the above, events with wrong hits associated to the Tracker track, which increase the χ^2 of the fit, are thrown out. This cut therefore increases the trustworthiness of the reconstructed Tracker track and its track attributes. The distribution is given in figure 7.8.

- Tracker track normalized χ^2 in the non-bending direction < 15
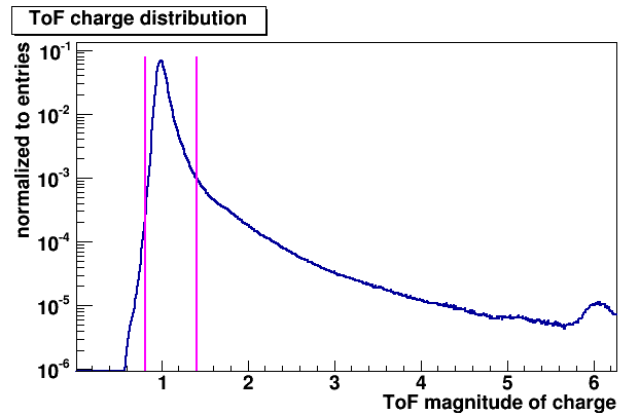
Figure 7.7.: ***Time of Flight detector reconstructed magnitude of charge for pres-
elected events.*** Reconstructed values between 0.8 and 1.4 are considered to
be compatible with unitary charged particles.

Cutting on the χ^2 of the non-bending direction is also needed, to clean out the sample
of wrong hit association and to be able to trust in the extrapolation of the Tracker
track, which relies on a good reconstruction in x- and y-direction. Figure 7.9 shows
the distribution of the normalized χ^2 in x-direction (non bending direction).

- The error on the rigidity measurement must be smaller than 50% of the reconstructed
  rigidity value
  This cut ensures that only events with a Tracker pattern suitable for detecting par-
  ticles of the given rigidity are used, since the different Tracker spans correspond to
  different maximum detectable rigidities. The distribution of the relative error of the
  rigidity depending on the rigidity can be seen in figure 7.10.
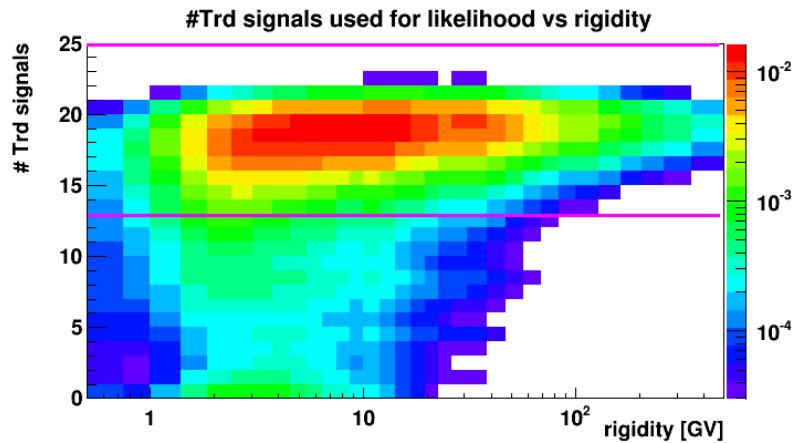
- More than twelve TRD signals used for the TrdM likelihood calculation
  The demand on a minimum number of TRD signals used for the likelihood determi-
  nation of the particle ensures a certain proton rejection power as described in chapter
  6, the distribution is given in figure 7.11.

The impacts on the selection by above criteria are shown in figure 7.12.

As the last step of selection the particle identification is applied, selecting protons,
electrons and positrons with the EcalBDT variable, the E/R-ratio and the sign of the
charge reconstructed by the Tracker. The EcalBDT and E/R-ratio distributions integrated
over the analysed energy range are shown in figure 7.13.

For the positron fraction measurement ~ 7 million leptons remain after all selection
criteria have been applied.

Since protons from data are used for the background determination in this analysis,
only protons are considered, which fulfil the same E/R-cut as the selected electrons and
positrons. This ensures a similar rigidity distribution of the selected protons and the pro-
tons mistakenly identified as positrons by the ECAL. The latter is necessary, since the TRD
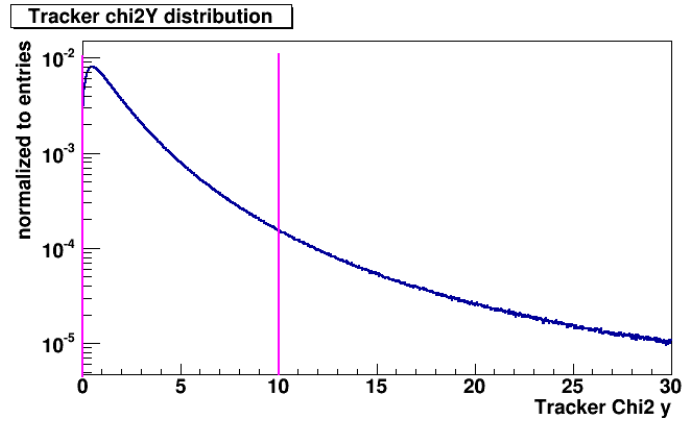
Figure 7.8.: ***Tracker normalized*** χ^2 ***in the bending direction.*** By demanding the χ^2 value to be below 10, events with wrong reconstruction due to interactions and noise are thrown out.
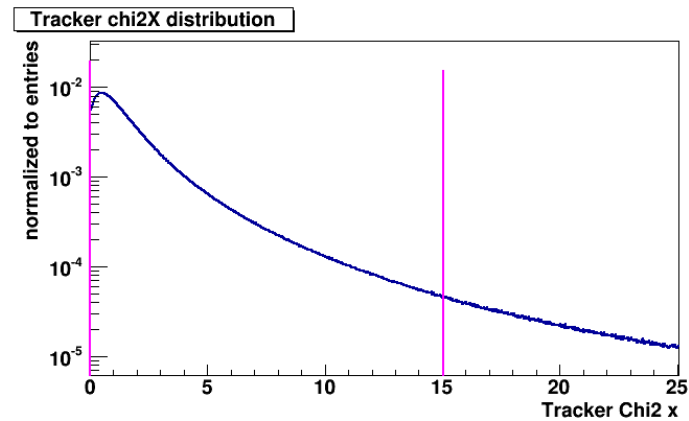
Figure 7.9.: ***Tracker normalized*** χ^2 ***in x-direction.*** By demanding the χ^2 value of the non bending direction to be below 15, badly reconstructed events are thrown out and the extrapolation of the track in both x- and y-direction can be trusted.

likelihood, which will be used in the following to determine and eliminate the residual proton background inside the positron sample, depends on the rigidity measurement. Protons are therefore selected by the same E/R-ratio cut and an inverse cut on the EcalBDT compared to positrons and electrons. The applied cut values are energy dependent and have been optimized to yield the smallest error on the positron fraction as will be explained in section 7.3.
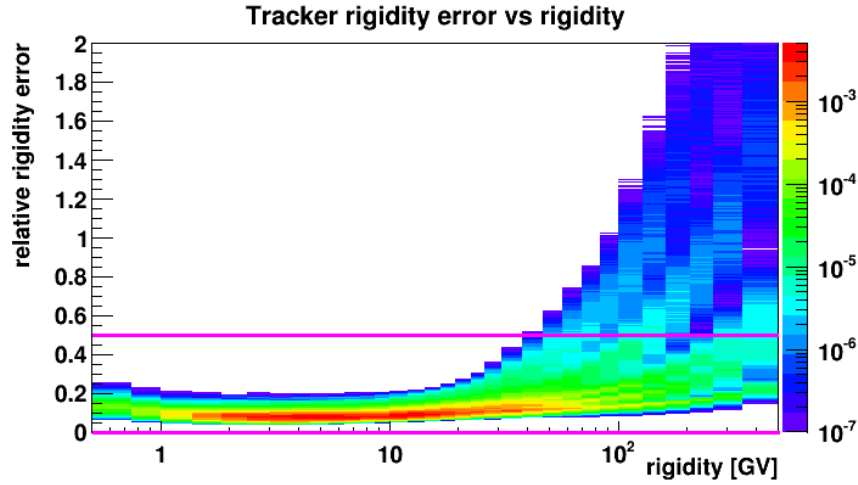
Figure 7.10.: **Relative error of the rigidity measurement.** Starting from about 30 GV the different track spans separate, which can be seen from the dispersion of the distribution. The inner Tracker only span with an MDR of about 80 GV stops fulfilling the maximum 50% error requirement for particles with a rigidity greater than 60 GV, followed by the inner Tracker plus plane 2 span at about 100 GV. However, the full span tracks with an MDR of 2 TV are accepted for all rigidities (for correct reconstructed tracks).

Figure 7.11.: **Number of reconstructed TRD signals used for the TrdM likelihood calculation.** The demand of a minimum number of TRD signals ensures a reasonable TRD proton rejection power and rejects events with bad Tracker track extrapolation due to interactions or misreconstruction. The rigidity dependence shows that high energy particles are not affected by this cut.
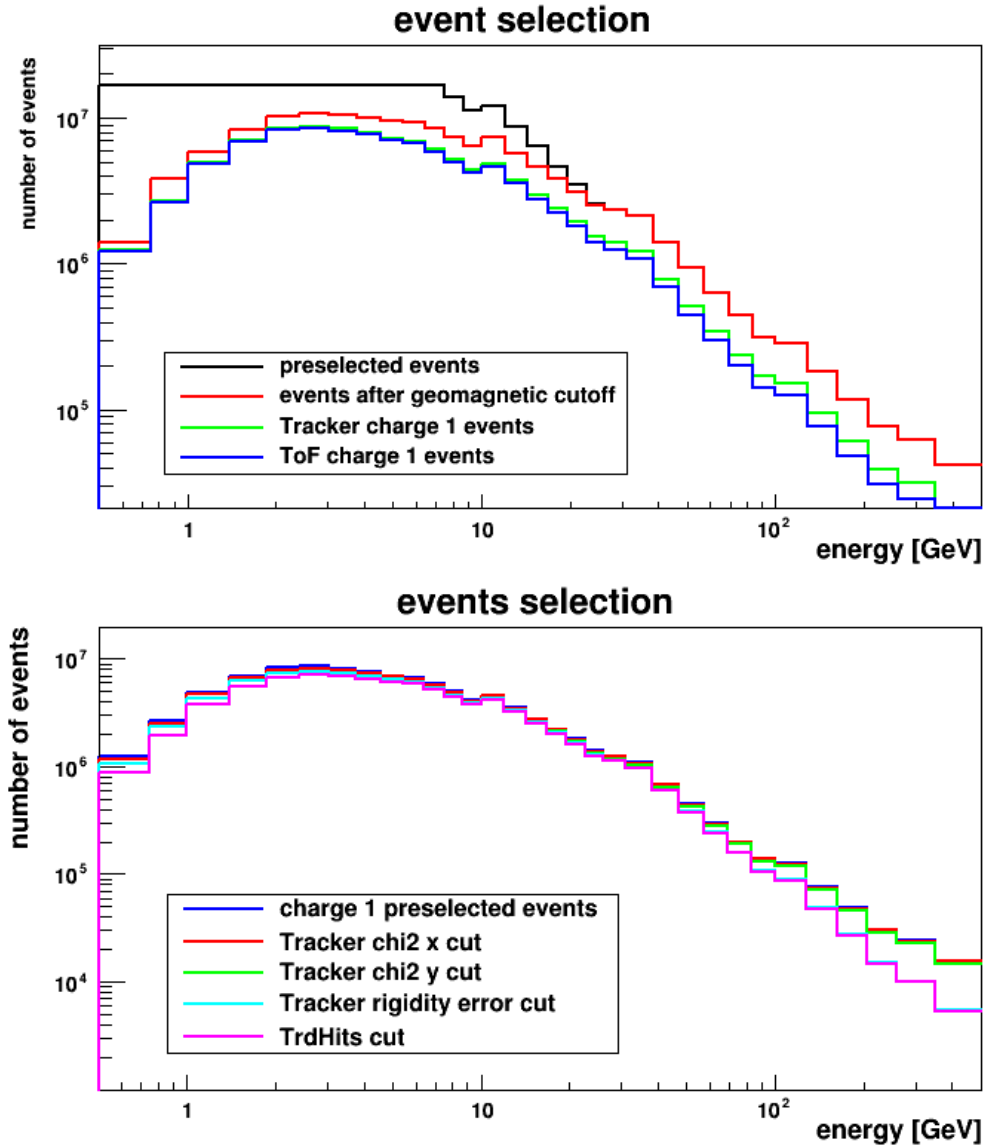
Figure 7.12.: ***Event selection sequential cut effects.*** Top: event selection to identify unity charged CR particles. Only 54 % of the selected events can safely be assumed to be primary cosmic rays. Of those 71 % are identified as unitary charged particles by Tracker and ToF. Bottom: further selection cuts applied on unitary charged particles. These additional quality cuts have an overall efficiency of 85 %.
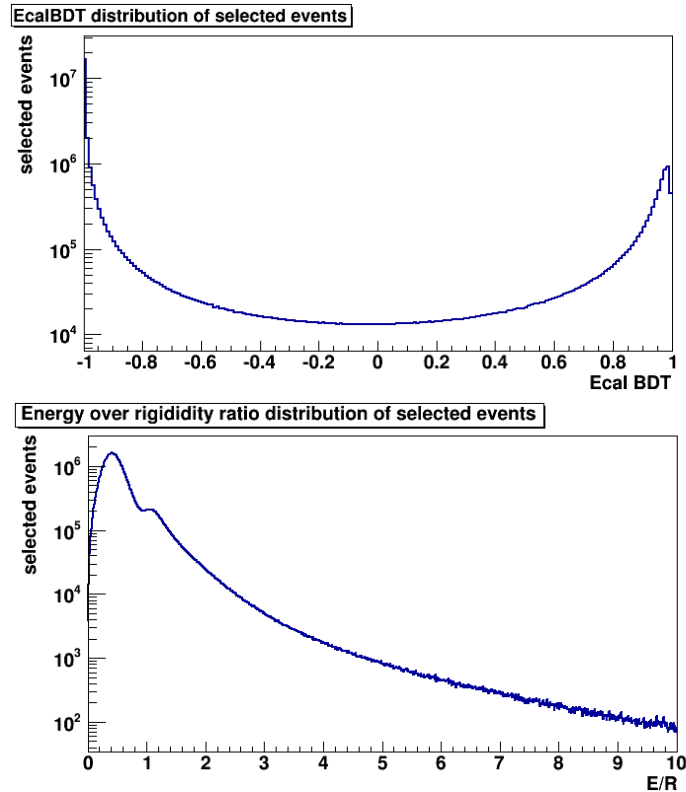
Figure 7.13.: ***Particle identification criteria: EcalBDT and E/R-ratio.*** The distribution is integrated over the analysed energy range. Electrons and positrons are selected by an energy dependent selection cut on the EcalBDT and the E/R distributions.

7.2. Background estimation

There are two independent sources of background for the positron identification. The dominant part of the remaining contamination in the positron sample after the selection described in the previous section is applied, are protons that the calorimeter mistakenly identifies as positrons. The EcalBDT together with a cut on the E/R ratio can provide a proton rejection of around 10^4 depending on energy, which would result in a positron purity of around 90%. Applying a cut on the TRD likelihood would remove nearly all the background from protons, but does not allow to determine the achieved purity. Instead of applying a cut on the TRD to remove the residual proton contamination and assume the sample to be background free, this analysis is using the TRD to determine the residual contamination with a high accuracy. Subsequently, a loose cut on the TRD likelihood with a high lepton efficiency is applied without loosing precision in the knowledge of the background. The TRD method used in this analysis is the TrdM method, which was developed in the course of this thesis and introduced in chapter 6.

A loose selection cut is applied on the ECAL classifier, which invokes a high positron

impurity due to the high abundance of protons in the cosmic rays. After the ECAL and Tracker identification cuts are applied the proton contamination is as high as 50%. The electron sample on the other hand is assumed to be free of contamination. By requiring negatively charged particles only antiprotons could contaminate the electron sample, but since their abundance in the cosmic rays is lower than the abundance of electrons, the rejection power of the calorimeter is sufficient to remove them from the selection.

The second source for contamination of the positron sample is due to charge confusion. Electrons being reconstructed with the wrong sign of the charge are identified as positrons. At the same time, positrons reconstructed with the wrong sign of the charge are identified as electrons and therefore missing in the positron sample. Two reasons for wrong charge sign determination play a role. The first is the finite spatial resolution of the Tracker signals, which can lead to wrong curvature reconstruction for high energetic particles. The second reason for charge confusion is due to wrong hit assignment to the Tracker track. Noise or signals induced by e.g. bremsstrahlung can be assigned to the primary track, which falsifies their reconstructed curvature.

In the following the strategies are presented, which quantify and handle these different backgrounds.

7.2.1. Proton contamination

The high proton abundance in the cosmic rays, which is about three orders of magnitude higher than the positron abundance, makes the discrimination between positrons and protons an important task for a lepton analysis. In the last chapter, three discriminating variables of the AMS-02 detector have been introduced. Applying sequential cuts on the variables a proton rejection of $\sim 10^6$ at 80% electron efficiency for energies up to 100 GeV can be achieved. For higher energies less efficient cuts need to be applied to achieve this rejection power.

In order to evaluate the residual proton contamination of the selected events with data, only two of the three discriminating variables are used for the first particle identification in this analysis. Loose energy dependent selection cuts are applied on the EcalBDT and E/R resulting in a residual proton contamination in the positron sample of 50%. The effect of the selection cuts is shown for the energy bin between 83.2 GeV and 100 GeV in figure 7.14.

Instead of applying an additional cut on the TRD likelihood, the TrdM likelihood distribution of positrons is fitted with templates for signal and background to determine the background contamination, which is then taken into account in the positron fraction calculation.

The templates for this fit are constructed from data. As the TRD is not sensitive to the sign of the charge of particles, the selected electrons can be used to set up the signal template. The electrons are assumed to be background free, since antiprotons are sufficiently suppressed by the ECAL identification cuts[2]. The protons used for the background

---

[2]At higher energies than analysed in this thesis, the charge confused protons, being identified as antipro-
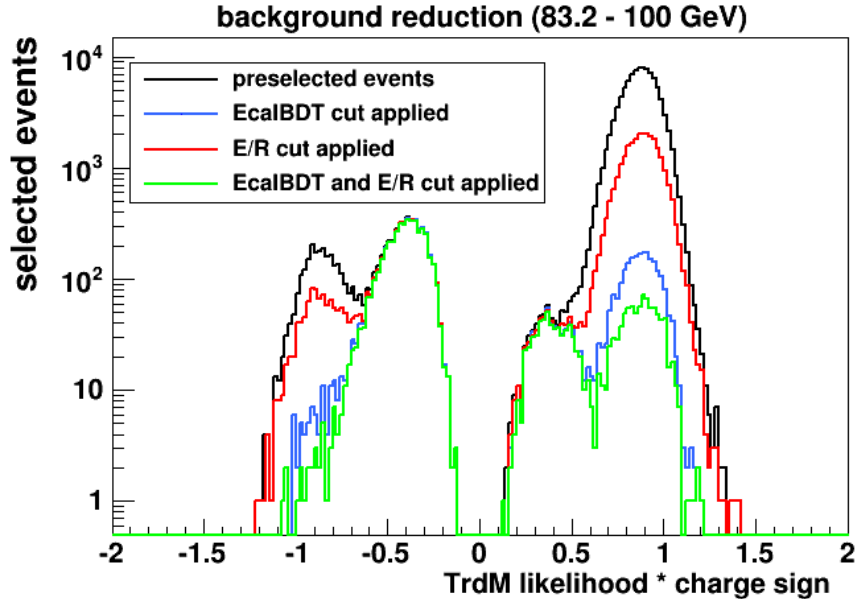
Figure 7.14.: ***Effect of the particle identification cuts on EcalBDT and E/R.*** The TrdM likelihood distribution are shown for positively and negatively charged selected particles. Black points: all preselected events, red: if EcalBDT cut is applied, blue: if E/R cut is applied, red: after applying both EcalBDT and E/R cut. The negative selected particles show no considerable contamination and can be assumed to be purely electrons. The positive side shows about equal amounts of positrons and protons in the selected sample.

template determination are selected by the same cut on the E/R ratio but an inverse cut on the EcalBDT. These protons need to have a similar rigidity distribution to those that actually make up the background in the positron sample. The TRD signals, and as a consequence the TRD likelihood, depend on the rigidity of the traversing particle, as described in chapter 4. If the protons would be selected by an inverse E/R cut, as would be natural to identify them, the protons falling into a certain energy bin would on average have a higher rigidity. A higher rigidity implies a lower and therefore more electron-like TRD likelihood value, which would result in a shift of the background template compared to the background in the positron sample.

The proton contamination is evaluated for each energy bin separately. Therefore also the signal and background templates are set up for each energy bin independently by the individual cuts on EcalBDT and E/R. The signal and background template are fed into a TFractionFitter element, which fits these two contributions to the TrdM likelihood distribution of the selected positrons.

As a result of the fit, which is depicted for the energy bin between 83.2 GeV and

---

tons, contribute in such a way that the background in the electron sample needs to be evaluated too or stronger ECAL cuts need to be applied.
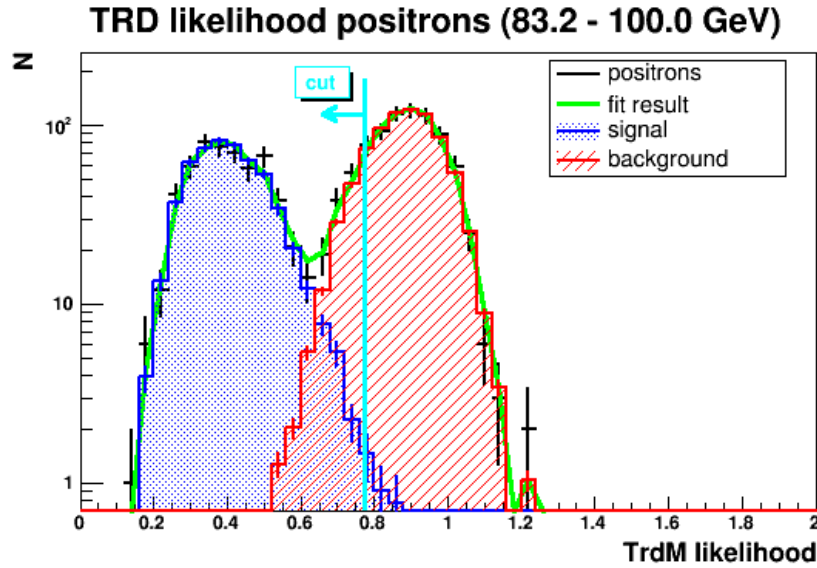
Figure 7.15.: ***Result of the signal and background fit to the positron likelihood distribution.*** Black points: data, green line: combined fit result, blue: signal, red: background. The cyan line demonstrates the cut applied after the fit in order to further reduce the proton background.

100 GeV in figure 7.15, the positron purity and the corresponding uncertainty are retrieved as well as the normalization of signal (positrons) and background (protons).

Signal and background are well separated in the TRD likelihood distribution. Therefore a loose cut can be applied on the likelihood distribution[3] to further reduce the proton background. The signal efficiency of this cut is kept well above 95%. This increases the positron purity but does not affect the background determination accuracy. The purity of the individual energy bins of the positron sample, after applying the additional cut on the TrdM likelihood, can be calculated from the number of surviving events in the signal and background distributions.

The obtained positron purity and its uncertainty together with the number of selected positrons and electrons go into the determination of the positron fraction.

7.2.2. Charge confusion

The effect of charge confusion can be split into two separate effects, called spillover and 'wrong hit assignment'.

The spillover effect is due to the finite spatial resolution of the Tracker signal measurement of $\sim 10\mu m$. Higher energetic particles are less bend by the magnetic field passing through the inner Tracker, which makes it more difficult to determine their curvature. A

---

[3]This cut is applied to both positron and electron distributions in order to keep the same selection efficiency.

small mistake in the measurement of a Tracker signal therefore might invert the direction of the curvature, reconstructing a positive rigidity for a negative charged particle or vice-versa. The magnitude of the reconstructed rigidity for a particle with the wrong sign of the charge reconstructed tends to be higher than the true rigidity of the particle. Hence this kind of contamination is reduced by the cut on the relative rigidity error and the request of E/R to be above a certain energy dependent threshold.

The effect of wrong hit association to the Tracker track is mainly traceable to secondary particles produced along the way of the particle through the detector. These secondary particles produce additional signals in the Tracker, which can falsely be associated to the track belonging to the primary particle. Since the curvature of high energetic particles is small, assigning a wrong signal to the track in the majority of the cases results in a higher curvature measurement and therefore a much smaller reconstructed rigidity compared to the true rigidity of the particle. The same false rigidity measurement occurs for lower energetic particles undergoing multiple scattering in the detector. The background evoked by these effects is strongly reduced by the requirements of the goodness of the track fit in both x- and y-direction ($\chi^2(x/y) < 15$ or 10) as well as an upper limit on the allowed E/R ratio of 10.

Figure 7.16 shows that the mentioned selection criteria suppress the charge confused particles by 80% to 90% depending on the particle energy.
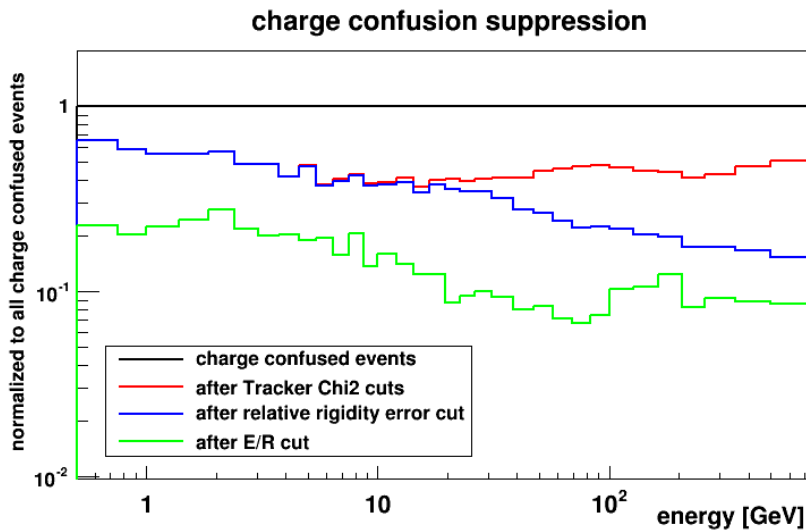
Figure 7.16.: **Suppression of charge confused events determined with electron MC.** The number of charge confused particles is reduced by 80% to 90% by applying the analysis event selection.

Since the TRD is not sensitive to the charge sign of the particles, the residual background due to the two effects of charge confusion cannot be evaluated from data in this approach. Instead the effects have been evaluated from Monte Carlo simulations. The official AMS-02 Monte Carlo is based on the GEANT-4.9.4 package, which simulates electromagnetic and

hadronic interactions of particles with the materials of the detector [156]. The electronics responses and their digitization have been simulated precisely according to their known behaviour. The generated signals then undergo the same reconstruction algorithm as the data recorded in space.

The single point resolution of the Tracker hits is simulated in MC and the production of secondary particles along the track due to electromagnetic interactions is also well reproduced by GEANT. The latter has been checked by looking at electron control events with a signal in the lower ToF counters corresponding to at least two particles [154].

In order to evaluate the effect of charge confusion in the lepton data, the fraction of positrons reconstructed in the electron MC sample has been analysed. Electrons from 0.25 GeV to 600 GeV are generated from the top plane of a cube with an edge length of 3.9 m containing the full detector. The same selection as described above for data[4] is applied to the reconstructed MC events. Electrons and positrons are identified by the cuts on the EcalBDT and E/R with the same cut values as used in the data analysis. The residual contamination, shown in figure 7.17 is then defined as:

$$R_{CC} = \frac{N_{e^- \to e^+}}{N_{e^- \to e^+} + N_{e^- \to e^-}} \; , \tag{7.1}$$

where $N_{e^- \to e^+}$ represents the electrons falsely identified as positrons and $N_{e^- \to e^-}$ represents the correct identified electrons.
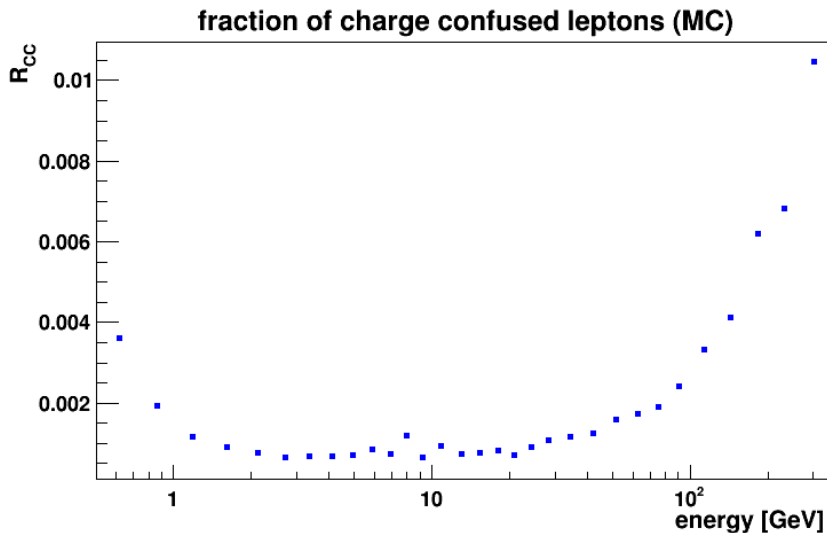
Figure 7.17.: ***Residual fraction of charge confusion for leptons determined with MC.*** The charge confusion is of the order of 1‰ up to 100 GeV. At higher energies the spillover effect begins to contribute stronger, which results in a residual charge confusion fraction of up to 1.5% of the electrons.

---

[4]The geomagnetic cut-off requirement is excluded, as it is not applicable to MC.

The residual number of charge confused particles after applying the analysis event selection is of the order of 1‰ of the analysed electrons up to 100 GeV. At higher energies the spillover effect begins to contribute stronger, which results in a residual charge confusion fraction of up to 1.5% in the highest energy bin from 260 GeV to 350 GeV.

Since the level of charge confusion is evaluated for each energy bin individually, the difference in flux between data and MC is irrelevant. About 5 million selected MC events are used to determine the charge confusion fraction, which is statistically sufficient and therefore does not introduce an additional systematic error.

The determined charge confusion ratio is taken into account in equation 7.8 to correctly evaluate the positron fraction in each energy bin.

7.3. Systematic effects

Systematic errors are biases in the measurement, which impact the result for many separate measurements in the same way and thereby lead to a difference between the mean of the distribution and the actual value of the measured observable [157]. A possible systematic error is for example a wrong gain calibration of the electromagnetic calorimeter that would result in a constant under- or overestimation of the particle energy. We assume that no systematic errors are made during the reconstruction, since the performance of the whole detector was tested among other tests twice in the Super Proton Synchrotron at CERN with different particle species of multiple energies [7, 133].

What is left to be determined are systematic uncertainties. The uncertainty originating from the residual background identification is given by the error of the template fit, which is propagated into the formula for the positron fraction. Another uncertainty comes from the selection of the values of the applied particle identification cuts, which also determine the template shapes. In order to find the optimal working point, a scan of the phase space of EcalBDT versus E/R has been performed and the error of the positron fraction due to statistics and background determination has been evaluated for each point. The result for the energy bin from 83.2 to 100 GeV is given in figure 7.18.

The impact of this working point selection has been evaluated by looking at the change of the positron fraction resulting from a variation of both EcalBDT and E/R cut around the working point. 900 different analysis are taken into account with a difference in the selection efficiencies of up to 10% or 30% depending on the energy bin. The distribution of the results of the different analyses for the energy bin from 83.2 GeV to 100 GeV are plotted in figure 7.19.

The effect of the different statistics in the analyses can be evaluated with a simple Monte Carlo and is shown in the lower plot of figure 7.19. Subtracting the statistical effect from the result, the width of the distribution of the fraction for the different analyses can be considered as the working point systematic uncertainty due to the applied selection cuts and used template shapes.

Other systematic effects have been considered, but found to be negligible. One of these effects is the bin-to-bin migration of events due to the error on the energy measurement.
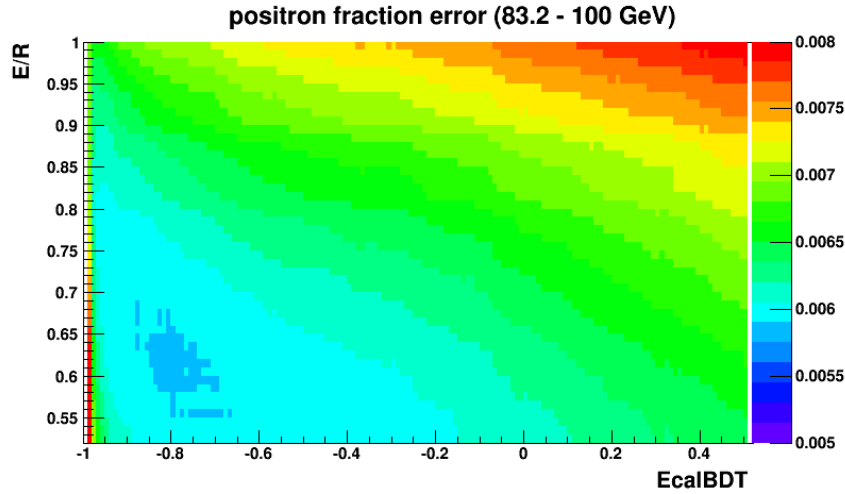
Figure 7.18.: ***Error on the positron fraction depending on the cut on EcalBDT and E/R.*** The result of the scan for the energy bin between 83.2 and 100 GeV is shown. The error increases to stronger cut values as the statistics decrease and also for soft cuts as the background determination becomes worse. The working point has been set to EcalBDT: -0.81 and E/R: 0.64.

The energy bins for this analysis were chosen according to the ECAL energy resolution, with a minimal width of 2.5 σ for the lowest energy bin and increasing to higher energies. As a result the error due to this effect is small in comparison to the systematic uncertainty due to the working point selection. Another effect is the uncertainty in the determination of the charge confusion fraction from MC. For this it has been checked that a $\pm 15\%$ deviation of charge confusion in MC compared to data would have again a negligible contribution to the overall systematic error.

Other effects as contaminations of the templates for the signal and background fit due to the determination from data and the possible difference in acceptance of positrons and electrons, which is known to be minor compared to the systematics due to the selection cuts [154], have not been investigated in detail in this analysis.

7.4. Results

With the optimal working point for the positron fraction analysis defined by the scan of the phase space of the particle identification variables and having determined the residual backgrounds, the positron fraction, can be calculated as

$$R = \frac{N_{e^+}^{true}}{N_{e^+}^{true} + N_{e^-}^{true}}. \tag{7.2}$$
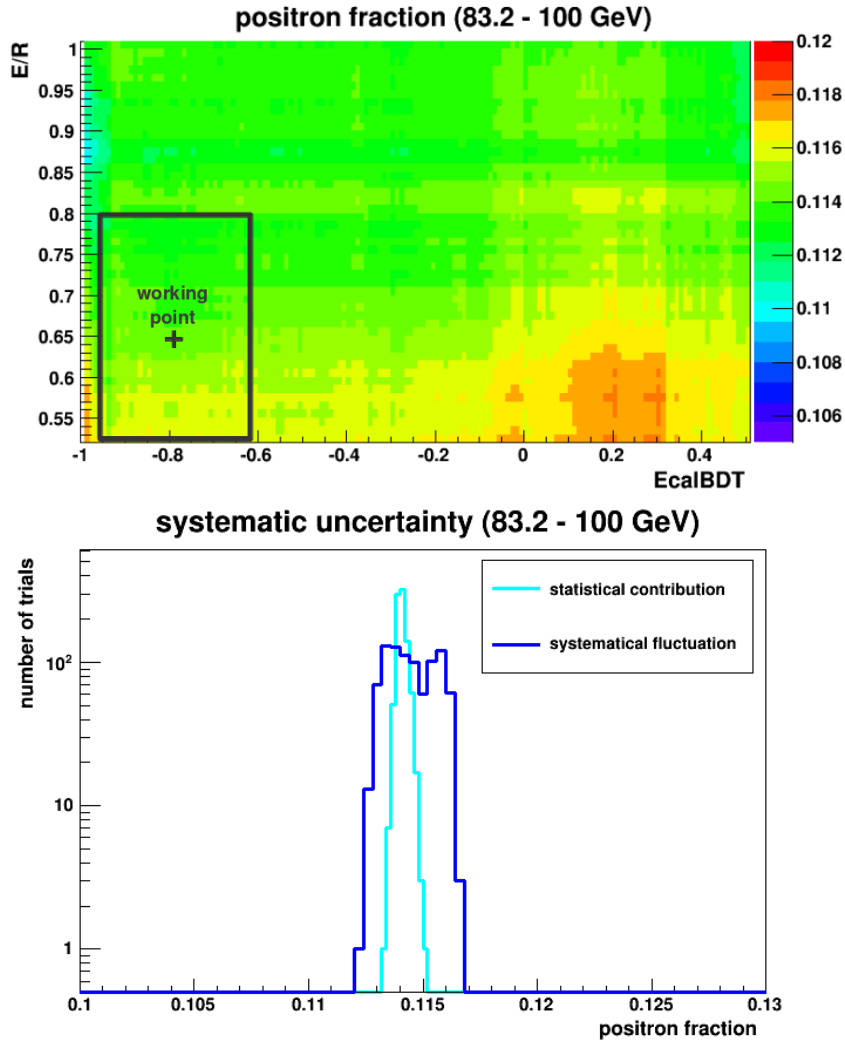
Figure 7.19.: ***Distribution of the positron fraction due to variation of the cut on EcalBDT and E/R.*** Top: results of the positron fraction analysis for different particle identification cuts. Bottom: projection on the z-axis of the selected region in the top plot. Blue: systematic fluctuation, cyan: statistical contribution.

Due to the background in our measurement, we do not measure $N_{e^+}^{true}$ and $N_{e^-}^{true}$ directly. Instead our samples are affected by charge confusion and in the case of the positrons also by proton contamination. The amount of charge confusion for leptons has been determined in section 7.2.2. It applies to positrons and leptons in the same way, since the detector is charge symmetric and the different particle fluxes do not come into play as the charge confusion has been determined for each energy bin separately. The proton background is given by the template fits described in section 7.2.1. Both types of background enlarge the observed positron fraction compared to the true fraction.

7. Positron fraction

Therefore the backgrounds have to be taken correctly into account and the quantities, which we measure are[5]:

$$N_{e^-}^{observed} = N_{e^-}^{true} + N_{e^+ \to e^-} - N_{e^- \to e^+} \qquad (7.3)$$

$$N_{e^+}^{observed} = N_{e^+}^{true} + N_{e^- \to e^+} - N_{e^+ \to e^-} + N_p \qquad (7.4)$$

with

$N_{e^-}^{true}$: true number of CR electrons
$N_{e^+}^{true}$: true number of CR positrons
$N_p = N_{e^+}^{observed}(1 - P)$: number of protons
P : positron purity from template fit.

Due to the compromise between statistics and amount of background in the positron sample, which needs to be subtracted, the positron purity P ranges from 65% to 98% depending on the energy.

The fraction of leptons reconstructed with the wrong charge sign R_{CC} is given by equation 7.1 and transforms equations 7.3 and 7.4 into:

$$N_{e^-}^{observed} = N_{e^-}^{true} + N_{e^+ \to e^-} - N_{e^- \to e^+} = N_{e^-}^{true}(1 - R_{CC}) + N_{e^+}^{true} R_{CC} \qquad (7.5)$$

$$N_{e^+}^{observed} = N_{e^+}^{true} + N_{e^- \to e^+} - N_{e^+ \to e^-} + N_p = N_{e^+}^{true}(1 - R_{CC}) + N_{e^-}^{true} R_{CC} + N_p \ . \qquad (7.6)$$

The observed ratio $R^{observed}$ can then be written as:

$$R^{observed} = \frac{N_{e^+}^{observed}}{N_{e^+}^{observed} + N_{e^-}^{observed}} = \frac{N_{e^+}^{observed}}{N(1 + r_p)} \qquad (7.7)$$

with $N = N_{e^+}^{true} + N_{e^-}^{true}$ being the total number of true leptons and $r_p = \frac{N_p}{N}$ the ratio of the number of protons in the positron sample to the total lepton number. Inserting equation 7.6 and 7.2 in 7.7 and solving for the true positron fraction R yields:

$$R = \frac{R^{observed}(1 + r_p) - r_p - R_{CC}}{1 - 2R_{CC}} \ . \qquad (7.8)$$

The error of the positron fraction consists of the statistical part ϵ_{stat}, the systematic uncertainty due to the proton background evaluation ϵ_{pro} and the systematic uncertainty due to the working point selection ϵ_{cuts} as explained in the last section:

$$\epsilon_{total} = \sqrt{\epsilon_{stat}^2 + \epsilon_{pro}^2 + \epsilon_{cuts}^2}. \qquad (7.9)$$

---

[5]The ansatz to determine the positron fraction has been made based on input from [158].

The statistical error is obtained by propagating the error on the number of observed electrons and positrons into the observed positron fraction. The systematic uncertainty due to the proton background is taken into account as an error on r_p, which is calculated by the propagation of the error of the positron purity ΔP obtained from the template fit.

The results for the positron fraction of this analysis are presented in figure 7.20. In addition to the corrected positron fraction, the observed positron fraction and the two background contributions are shown. The numbers of the result are given in table 7.1.
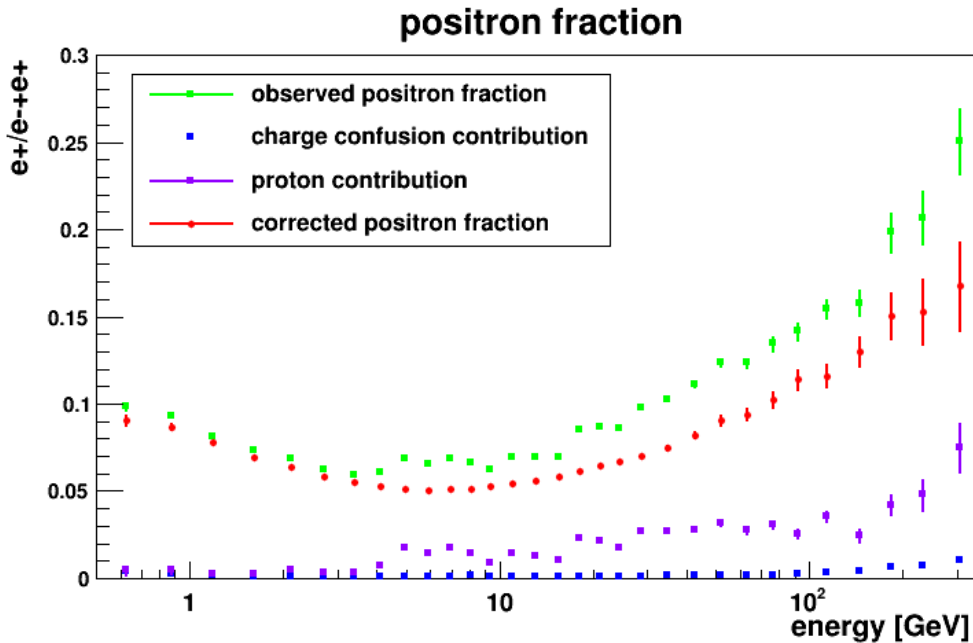
Figure 7.20.: ***Result of the positron fraction analysis.*** The observed positron fraction (green, statistical error only) is corrected for the background from charge confusion (blue) and protons (cyan) and yields the final result (red, total error according to equation 7.9).

The fluctuations in the proton background contribution arise from the ECAL identification cuts, which were tuned for each energy bin independently to obtain a small overall error. The error is sensitive to the goodness of the fit, which depends on the fit templates that are determined by the applied ECAL cuts, and the statistics of selected electrons and positrons. No attention was given to the smoothness of the obtained positron purity for the different energy bins, but rather to a working point selection within a region of constant small error as described in section 7.3. The contribution of charge confusion to the observed positron fraction is minor for most part of the energy range as it was reduced by strong selection cuts as explained in section 7.1. In this way the impact of Monte Carlo is kept at a minimum, as the estimation of the residual charge confusion is the only part of this analysis, where MC simulations were used.

The here presented method could be extended to higher energies with more statistics

min E $[GeV]$	max E $[GeV]$	N_e^-	N_e^+	R	ϵ_{stat}	$\epsilon_{protons}$	ϵ_{cuts}	ϵ_{tot}
0.5	0.8	20683	2149	0.0905	0.0026	0.0020	0.0004	0.0033
0.8	1.0	50182	4888	0.0869	0.0016	0.0012	0.0002	0.0021
1.0	1.4	143166	12226	0.0775	0.0009	0.0007	0.0002	0.0012
1.4	1.9	349780	26517	0.0696	0.0005	0.0004	0.0002	0.0007
1.9	2.4	530801	36404	0.0634	0.0004	0.0003	0.0002	0.0006
2.4	3.0	645686	40588	0.0585	0.0004	0.0003	0.0003	0.0006
3.0	3.8	671589	39666	0.0551	0.0004	0.0003	0.0002	0.0005
3.8	4.6	642758	36433	0.0530	0.0004	0.0003	0.0002	0.0005
4.6	5.4	600247	32676	0.0510	0.0003	0.0003	0.0002	0.0005
5.4	6.4	556976	29915	0.0501	0.0003	0.0003	0.0001	0.0005
6.4	7.5	465248	25273	0.0508	0.0003	0.0004	0.0001	0.0005
7.5	8.7	381197	21014	0.0511	0.0004	0.0004	0.0001	0.0005
8.7	10.0	297075	16696	0.0526	0.0005	0.0004	0.0001	0.0006
10.0	12.0	313172	18284	0.0543	0.0004	0.0004	0.0001	0.0006
12.0	14.3	220387	13312	0.0562	0.0005	0.0005	0.0000	0.0008
14.3	16.8	161726	10077	0.0579	0.0006	0.0006	0.0001	0.0009
16.8	19.6	123385	8203	0.0615	0.0007	0.0008	0.0001	0.0011
19.6	22.7	92380	6464	0.0647	0.0008	0.0009	0.0002	0.0012
22.7	26.2	68594	5016	0.0673	0.0009	0.0010	0.0001	0.0014
26.2	31.0	57500	4401	0.0700	0.0010	0.0012	0.0004	0.0016
31.0	38.4	46286	3807	0.0749	0.0012	0.0014	0.0001	0.0018
38.4	47.0	27267	2483	0.0822	0.0014	0.0019	0.0001	0.0023
47.0	57.2	16263	1646	0.0903	0.0017	0.0025	0.0002	0.0031
57.2	69.2	10003	1059	0.0940	0.0021	0.0032	0.0003	0.0039
69.2	83.2	6272	729	0.1023	0.0022	0.0042	0.0005	0.0048
83.2	100.0	4177	551	0.1141	0.0028	0.0052	0.0008	0.0059
100.0	127.9	3486	473	0.1161	0.0033	0.0059	0.0009	0.0068
127.9	162.6	1846	286	0.1299	0.0040	0.0081	0.0010	0.0091
162.6	206.0	1020	190	0.1507	0.0061	0.0120	0.0007	0.0134
206.0	260.0	561	107	0.1530	0.0093	0.0164	0.0034	0.0192
260.0	350.0	395	86	0.1676	0.0140	0.0214	0.0035	0.0258

Table 7.1.: **Results of the positron fraction measurement between 0.5 GeV and 350 GeV**

available. This can be seen from the fit result of the last analysed energy bin from 260 GeV to 350 GeV, shown in figure 7.21. The signal and background distributions are still well separated and the fit uncertainty is in the order of 5 %.
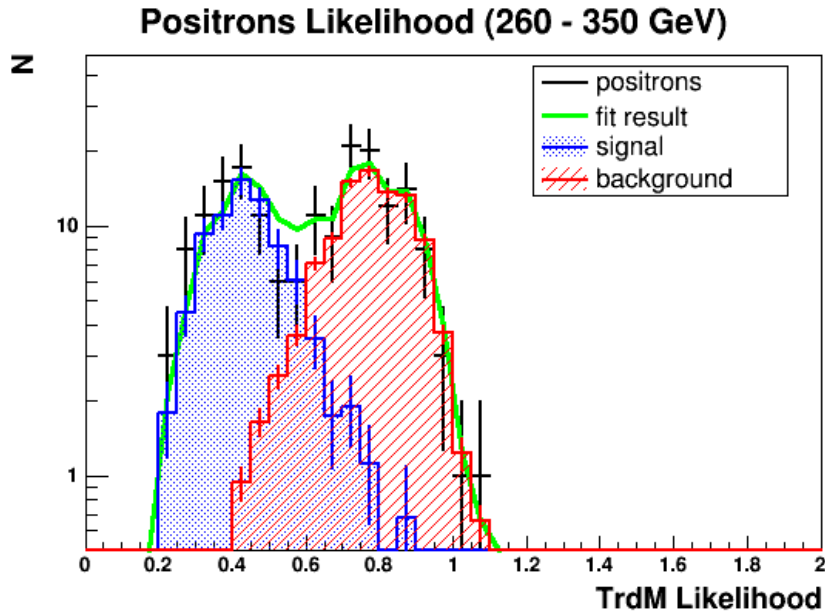
Figure 7.21.: ***Fit result for the energy bin from 260 GeV to 350 GeV.*** The signal and background distribution are still well separated and the error of the retrieved purity is in the order of 5%.

The comparison of the result of this work to the official result of the AMS collaboration [154] is shown in figures 7.22 and 7.23. Both analyses agree within their uncertainty. The TRD likelihood used in the official analysis is the TrdK likelihood, which was also introduced in chapter 6. Although both analyses use different methods and follow different approaches, they agree well within their uncertainty, which emphasizes the feasibility of the result.

The positron fraction steadily rises between 10 GeV and 350 GeV. Displaying the fraction in linear scale, as can be seen in figure 7.23, emphasizes the change in slope of the rise above 50 GeV.

As stated in [154], the rise of the positron fraction can be fitted nicely with an additional source of positrons and electrons with a single power law spectrum.

The flux of electrons Φ_{e^-} and positrons Φ_{e^+} in the cosmic rays can be parametrized by an individual diffuse power law and a common additional source, also modelled by a power law:

$$\Phi_{e^+} = C_{e^+} E^{-\gamma_{e^+}} + C_s E^{-\gamma_s} e^{-E/E_s} \tag{7.10}$$

$$\Phi_{e^-} = C_{e^-} E^{-\gamma_{e^-}} + C_s E^{-\gamma_s} e^{-E/E_s} \; . \tag{7.11}$$
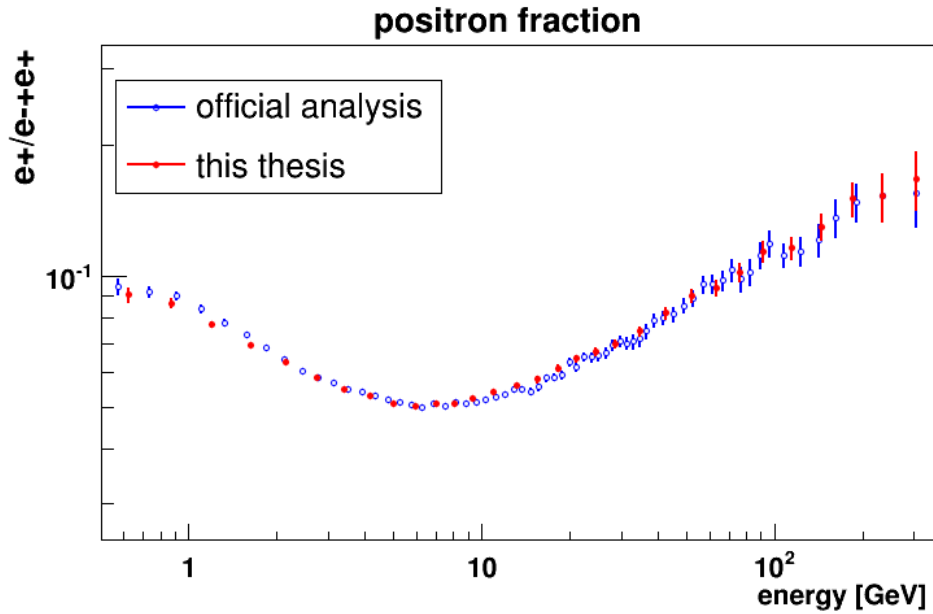
Figure 7.22.: ***Result of the positron fraction analysis from 0.5 GeV to 350 GeV.*** For both analyses the total errors (statistical + systematic) are displayed. The analyses agree within $1\,\sigma$ of their errors. For the official analysis see [154].
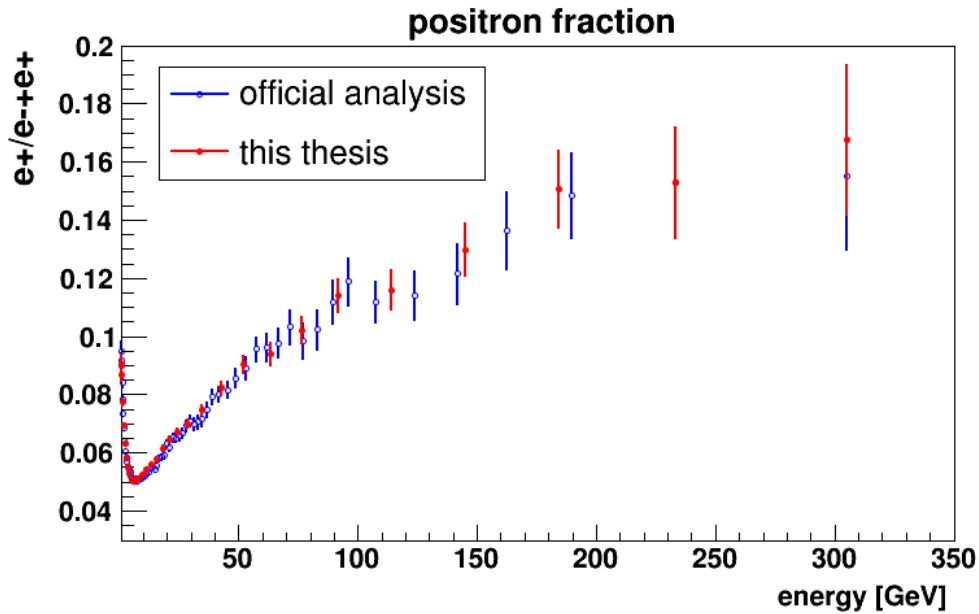
Figure 7.23.: ***Result of the positron fraction analysis from 0.5 GeV to 350 GeV on linear scale.*** The slope of the rise changes by an order of magnitude from 20 GeV to 250 GeV. For the official analysis see [154].

In order to estimate the parameters of the additional source a fit to the data of this analysis has been performed. The standard CR flux parameters of electrons has been taken from a fit to the PAMELA data [159], which leaves the standard CR positron parameters C_{e+}, $E^{-\gamma_{e+}}$ and the three source parameters C_s, $E^{-\gamma_s}$ and E_s as free parameters for the fit. The absolute value of the spectral index and coefficient for the electron power law have no impact on the result of the fit, since only the difference between the spectral indices and the ratio of the coefficients comes into play in the positron fraction. Fitting the data in the energy range above 1 GeV yields a $\chi^2/ndf = 18.23/29$. The result of the fit as well as the background model contribution are shown in figure 7.24, the input and output parameters are given in table 7.2.
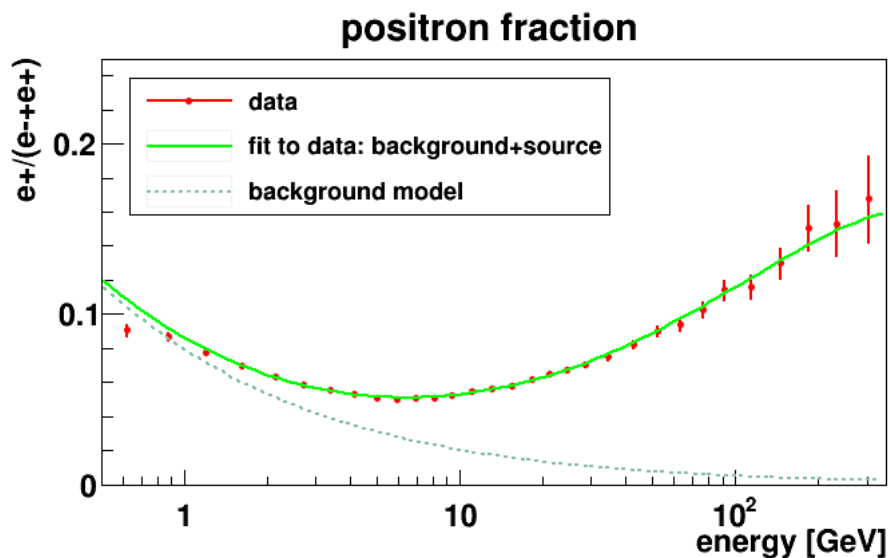
Figure 7.24.: ***Fit of a model to the positron fraction.*** The regular cosmic rays fluxes are treated as a background, modelled with individual power laws for electrons and positrons. The spectral index of electrons has been determined form PAMELA data to be $\gamma_{e-} = 3.54$, while the fit gives $\gamma_{e+} = 4.16$. The fit to the positron fraction data above 1 GeV with an additional common source to e^+, e^-, yields $\gamma_s = 2.90$ and $E_s = 750^{+1024}_{-280}$ with a $\chi^2/ndf = 18.23/29$ for the fit.

The power law models of the background CR electron and positron spectra as well as the source model can be seen in figure 7.25.

The additional source of positions and electrons could be of astrophysical origin; multiple pulsars with a suitable age and distance are known that could explain this behaviour of the positron fraction [11]. But the excess of high energetic positrons could also be due to Dark Matter particle annihilation [12].

To disentangle these two possible origins of the additional positrons, the anisotropy of the positron fraction needs to be studied. Dark Matter is supposed to be distributed homogeneously in our galaxy, as a consequence the fraction should show no anisotropy if Dark

Fit result		
input parameters	C_{e^-}	1040.76
	γ_{e^-}	3.54
output parameters	C_{e^+}	90.02
	γ_{e^+}	4.16
	C_s	8.95
	γ_s	2.90
	E_s	750^{+1024}_{-280} GeV

Table 7.2.: **Parameters of the fit to the positron fraction data above 1 GeV.** The input values of the electron spectral index and coefficient have no impact on the fit result, since the fraction only depends on the differences between the indices and ratio of the coefficients.
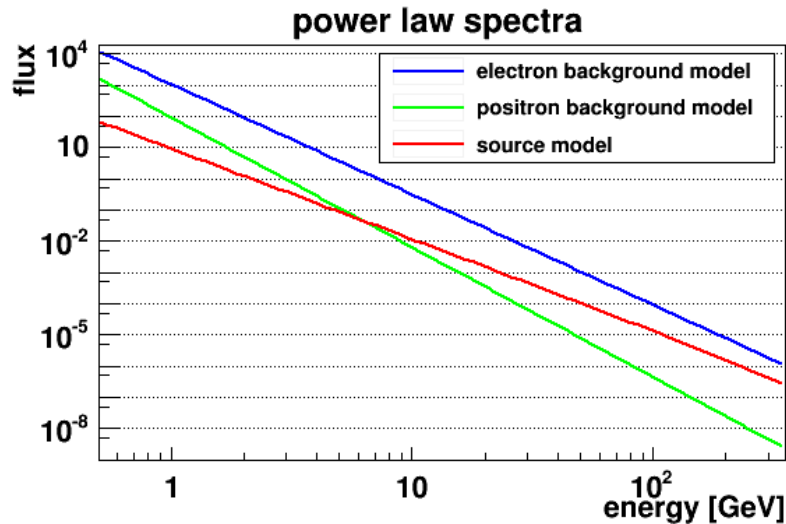
Figure 7.25.: **Power law models of standard CR electrons, positrons and additional source.** The regular cosmic rays fluxes are modelled with individual power laws for electrons and positrons. The spectral index of electrons has been determined form PAMELA data, while the parameters of the positron and source model are determined by the fit to the positron fraction data.

Matter annihilation is the source of the high energetic positrons. Pulsars on the contrary are point like sources. Due to the deflection of charged particles propagating through the galactic magnetic fields, though, the anisotropy of the pulsar hypothesis is washed out. If multiple pulsars contribute to the positron excess at the same time, the expected measured anisotropy would be reduced even further. The sensitivity to the anisotropy of the analysed data sample is too small to exclude either of the possible sources.

In order to come to any conclusion about the nature of the source of the additional

positrons, more data is needed. So far only 8% of the total expected dataset[6] of AMS-02 has been analysed. Having the full statistics available will reduce the statistical error by about 70%. The dominant error in this analysis, as can be seen in table 7.1, is due to the proton background determination. This uncertainty will also reduce with more data available as the fit will improve with more statistics to set up the templates. Therefore future analyses with smaller errors and up to higher energies might reveal the true source.

---

[6]This assumes the ISS to be operated until 2028.

8. Conclusions

On the 19th of May 2011 AMS-02 started taking data on the International Space Station after a 16 year long construction and testing phase. It has recorded more than 30 billion cosmic ray events so far, which only corresponds to 8 % of its expected total data volume[1].

One of the main physics goals of AMS-02 is the search for Dark Matter. Weak interacting massive particles (WIMPs), being the most promising Dark Matter candidates, can annihilate in our galaxy and thereby produce an additional signal in the spectra of the annihilation products on top of the ordinary cosmic ray flux. As the effect will be most prominent for annihilation products with a low cosmic ray flux, the study of positrons in the cosmic rays is of high interest.

Due to the high abundance of protons, a good discrimination of positrons and protons is important for a positron analysis. The two main detectors of AMS-02 to distinguish between positrons and protons are the Transition Radiation Detector and the Electromagnetic Calorimeter. In order to perform a high precision analysis of the positron fraction, the ratio of positrons to the sum of positrons and electrons in the CRs, the performance of both detectors need to be optimal. In the framework of this thesis, given our involvement in the hardware construction of the TRD, the TRD performance has been studied in detail.

Conducting a complex experiment such as AMS-02 in the varying space environment needs continuous monitoring and changes of operational parameters. For the Transition Radiation Detector this implies daily HV adjustments, monthly gas refills and continuous caution to stay in the operable temperature range of the detector. The vacuum of space leads to a diffusion of gas molecules out of the TRD straw tubes. The gas pressure and composition as well as the applied high voltage have a strong impact on the gas gain of the TRD signal. The continuous temperature changes and the daily HV adjustments require an offline calibration of the TRD to achieve a constant detector response. The temperature changes also induce relative movements of TRD and Tracker, which call for a time dependent alignment to correct for this effect. An alignment for the Transition Radiation Detector has been presented, which calculates four correction parameters for each of the 328 TRD modules every ten minutes. In order to calculate these corrections not only signals in the detector have been used, but also the high accuracy points reconstructed from missing hits. Missing hits uniquely occur when particles pass between two gas proportional tubes. The small spacing between the tubes leads makes them high resolution points of passage of the particle. The residual resolution of 45 μm in the horizontal direction per module is sufficiently small to give a good path length estimation of the particle through the straw tubes.

---

[1]This assumes an operation of the space station until 2028.

8. Conclusions

The performance of the TRD has been further improved by using missing hits for the tracking in the TRD. Including the missing signals in the track fit aims at correcting for multiple scattering and minor interactions in the detector. These result in an extrapolation of the Tracker track into the TRD volume that does not represent the particle path. Due to the high geometrical efficiency of the TRD modules, the occurrence rate of missing signals is low, and as a consequence only for every second event a missing signal is found in one of the projections (x-z or y-z). Still including them in the track reconstruction improves the TRD likelihood determination and consequently the proton rejection for certain event topologies by about 40 % compared to other TRD likelihood methods available in the AMS software, as it was shown in chapter 6.

With 18 month of analysed AMS-02 data, the positron fraction has been determined with unprecedented precision and extending the energy range measured by a spectrometer by more than a factor of two up to 350 GeV. The analysis performed in the course of this thesis validates the official AMS analysis [154] by using a more data driven approach and using different reconstructed variables.

The common event preselection, which was largely developed in the framework of this thesis, was presented. The background in the positron sample caused by wrong charge assignment to electrons is strongly suppressed in this analysis by the applied selection. The residual contamination of charge confusion has been determined by looking at the Tracker performance in MC simulations and has been taken into account in the positron fraction determination.

Loose selection cuts on ECALs positron−proton separating variables have been used in combination with a template fit to the likelihood method of the TRD in this analysis. This approach allows to determine the background induced by protons from data with a high accuracy, which leads to a clean positron sample after background subtraction, while keeping a high signal efficiency.

The result of the analysis shows that the positron fraction steadily decreases up to energies of 7 GeV, as expected from the secondary production of positrons by interaction of primary CR with the interstellar medium. Above 10 GeV it continually rises, whereas the slope of the rise changes by an order of magnitude from 20 GeV to the highest analysed energies. The rise of the positron fraction implies an additional source of high energetic positrons. This additional source can be modelled by a single power law. The data above 1 GeV can be fitted by a source with an energy cut-off of $E_s = 750^{+1024}_{-270}$ GeV yielding a $\chi^2/ndf = 18.23/29$ of the fit.

The official analysis is performing a two dimensional template fit in the TRD likelihood - E/R plane in order to determine the charge confusion and proton backgrounds simultaneously. As a consequence MC is needed to determine the signal, charge confusion and proton templates, which requires fine-tuning of the TRD MC. This has been avoided in the here presented analysis as it follows a robust data driven approach and uses MC only minimally. The method has the potential to be used for analysis to even higher energies, however, more data needs to be accumulated to make a statistically meaningful statement above 350 GeV.

The current knowledge of the positron fraction is not sufficient to ultimately answer the

question of the origin of the positron excess. Both pulsar and Dark Matter models can fit the data [11, 12], as they have many free parameters. The change in slope towards high energies of the positron fraction suggests that the maximum and consequently the drop, will appear within the measurable energy range of AMS-02. Future analyses of the proton, electron and positron fluxes as well as the measurement of B/C and Helium, which are soon to be published, will help to improve the determination of the cosmic propagation models. This will lead to a better understanding of the background in the positron fraction. Together with further measurements of the positron fraction this will help to reduce the variety of allowed models to explain the observed additional high energetic positrons.

Bibliography

[1] The CMS collaboration, "Observation of a new boson with mass near 125 GeV in pp collisions at $\sqrt{s} = 7$ and 8 TeV", *submitted to JHEP* (2013). arXiv:1303.4571.

[2] The ATLAS collaboration, "Observation of a new particle in the search for the Standard Model Higgs boson with the ATLAS detector at the LHC", *Physics Letters B* **716** (2012) 1–29. arXiv:1207.7214.

[3] C.D. Anderson, "The Positive Electron", *Phys. Rev.* **43** (1933) 491–494.

[4] S.H. Neddermeyer and C.D. Anderson, "Note on the Nature of Cosmic-Ray Particles", *Physical Review* **51** (1937), no. 10, 884–886.

[5] Lattes, Occhialini, and Powell, "Observation of the Tracks of Slow Mesons in Photographic Emulsions", *Nature* **160** (1947) 453–456.

[6] The Pierre Auger Collaboration, "Correlation of the Highest-Energy Cosmic Rays with Nearby-Extragalatic Objects", *Science* **318** (2007) 938–943.

[7] A. Kounine, "Status of the AMS experiment", *arXiv:1010.2836* (2010). invited talk at ISVHECRI 2010.

[8] J. Ellis, R.A. Flores, K. Freese, S. Ritz, D. Seckel, and J. Silk, "Cosmic ray constrains on the annihilations of relic particles in the galactic halo", *Physics Letters B* **214** (1988) 403–412.

[9] O. Adriani et al., "An anomalous positron abundance in cosmic rays with energies 1.5-100 GeV", *Nature* **458** (2011) 607–609.

[10] M. Ackermann et al., "Measurement of Separate Cosmic-Ray Electron and Positron Spectra with the Fermi Large Area Telescope", *Physics Review Letters* **108** (2012) 011103.

[11] T. Linden and S. Profumo, "Probing the Pulsar Origin of the Anomalous Positron Fraction with AMS-02 and Atmospheric Cherenkov Telescopes". arXiv:1304.1791, 2013.

[12] J. Kopp, "Constraints on dark matter annihilation from AMS-02 results". arXiv:1304.1184, 2013.

Bibliography

[13] C.J. Copi, D.N. Schramm, and M.S. Turner, "Big-Bang Nucleosynthesis and the Baryon Density of the Universe", *Science* **267** (1994), no. 5195, 192–199.

[14] S. Perlmutter, "Supernovae, Dark Energy, and the Accelerating Universe", *Physics today* **53** (2003) 53.

[15] Planck Collaboration, "Planck 2013 results. I. Overview of products and scientific results", *submitted to Astronomy and Astrophysics* (2013). arXiv:1303.5062.

[16] S. Perlmutter et al., "Measurements of Omega and Lambda from 42 High-Redshift Supernovae", *Astrophysics Journal* **517** (1998), no. 565,.

[17] A.G. Riess et al., "Observational Evidence from Supernovae for an Accelerating Universe and a Cosmological Constant", *Astron. Journal* **116** (1998), no. 1009,.

[18] N.A. Bahcall, J.P. Ostriker, S. Perlmutter, and P.J. Steinhardt, "The Cosmic Triangle: revealing the State of the Universe", *Science* **284** (1999) 1481–1488.

[19] F. Zwicky, "On the Masses of Nebulae and of Clusters of Nebulae", *Astrophysical Journal* **86** (1937) 217.

[20] AMS Collaboration, "AMS on ISS: Construction of a particle physics detector on the International Space Station". AMS internal note, 2010.

[21] Th. Wulff, "About the radiation of high penetration capacity contained in the atmosphere", *Physikalische Zeitschrift* **10** (1909) 152–157.

[22] V.F. Hess, "Über Beobachtungen der durchdringenden Strahlung bei sieben Ballonfahrten", *Physikalische Zeitschrift* **13** (1912) 1084–1091.

[23] R.A. Millikan et al., "High Frequency Rays of Cosmic Origin I-III", *Phys. Rev.* **27,28** (1926), no. 27:353, 27:645, 28:851,.

[24] J. Clay and H.P. Berlage, "Variation der Ultrastrahlung mit der geographischen Breite und dem Erdmagnetismus", *Naturwissenschaften* **20** (1932) 687–688.

[25] B. Rossi, "On the Magnetic Deflection of Cosmic Rays", *Phys. Review* **36** (1930) 606.

[26] P. Freier, E.J. Lofgren, E.P. Ney, F. Oppenheimer, H.L. Bradt, and B. Peters, "Evidence for Heavy Nuclei in the Primary Cosmic Radiation", *Phys. Review* **74** (1948) 213–217.

[27] B. Rossi, "Directional Measurements on the Cosmic Rays Near the Geomagnetic Equator", *Phys. Review* **45** (1934) 212–214.

[28] P. Auger et al., "Extensive Cosmic-Ray Showers", *Rev. Mod. Phys.* **11** (1939) 288–291.

[29] R. Davis, "A review of the homestake solar neutrino experiment", *Progress in Particle and Nuclear Physics* **32** (1994) 13–32.

[30] V. Gribov and B. Pontecorvo, "Neutrino astronomy and lepton charge", *Physics Letters B* **28** (1969) 493–496.

[31] B. Jegerlehner, F. Neubig, and G. Raffelt, "Neutrino Oscillations and the Supernova 1987A Signal", *Physical Review D* **54** (1996) 1194–1203.

[32] SNO collaboration, "Measurement of the Rate of ve+d->p+p+e- Interactions Produced by ^8B Solar Neutrinos at the Sudbury Neutrino Observatory", *Physical Review Letters* **87** (2001) 071301.

[33] A.A. Penzias and R.W. Wilson, "A Measurement of Excess Antenna Temperature at 4080 MC/s", *Astrophysical Journal* **142** (1965) 419–421.

[34] R.A Alpher and R. Herman, "Evolution of the universe", *Nature* **162** (1948) 774–775.

[35] G.F. Smoot et al., "First results of the COBE satellite measurement of the anisotropy of the cosmic microwave background radiation", *Advance sin Space Research* **1** (1991) 193–205.

[36] C.L. Bennett et al., "Nine-Year Wilkinson Microwave Anisotropy Probe (WMAP) Observations: Final Maps and Results", *submitted to ApJS* (2012). arXiv:1212.5225.

[37] Wayne Hu and Martin White, "Acoustic Signatures in the Cosmic Microwave Background", *The Astrophysical Journal* **471** (1996), no. 1, 30.

[38] L. Bergström and A. Goobar, "Cosmology and Particle Astrophysics". Springer-Verlag, 2004.

[39] V.S. Berezinskii, S.V. Bulanov, V.A. Dogiel, V.L. Ginzburg, and V.S. Ptuskin, "Astrophysics of Cosmic Rays". Elsevier Science Publishers B.V., 1990.

[40] V.S. Ptuskin, V.N. Zirakashvili, and E.S. Seo, "Spectra of Cosmic Ray Protons and Helium Produced in Supernova Remnants", *The Astrophysical Journal* **763** (2012), no. 47,.

[41] D. H. Perkins, "Particle Astrophysics". Oxford University Press, 2003.

[42] V.L. Ginzburg and S.I. Syrovatskii, "The Origin of Cosmic Rays". Macmillan, 1964.

[43] A. Hewish, S.J. Bell, J.D.H. Pilkington, P.F. Scott, and R.A. Collins, "Observation of a Rapidly Pulsating Radio Source", *Nature* **217** (1968) 709–713.

[44] The Fermi LAT Collaboration, "Fermi's Gamma-ray sky", 2009.

Bibliography

[45] E. Fermi, "On the Origin of the Cosmic Radiation", *Physical Review* **75** (1949) 1169–1174.

[46] V. Ptuskin, "Origin and Propagation of Cosmic Rays", *American Institute of Physics* **AIP Conf. Proc. 1381** (2011) 150–158. proceedings of the 25th Texas Symposium on Relativistic Astrophysics.

[47] M. Ackermann et al., "Detection of the Characteristic Pion-Decay Signature in Supernova Remnants", *Science* **339** (2013), no. 6121, 807–811.

[48] I.V. Moskalenko and A.W. Strong, "Propagation of cosmic-ray nucleons in the Galaxy", *Astrophysics Journal* **508** (1998) 212–228.

[49] C. Evoli, D. Gaggero, D. Grasso, and L.Maccione, "Cosmic-Ray Nuclei, Antiprotons and Gamma-rays in the Galaxy: a New Diffusion Model", *Journal of Cosmology and Astroparticle Physics* **2008** (2008), no. 018,.

[50] I.V. Moskalenko and A.W. Strong, "Propagation of Cosmic-Ray Positrons and Electrons", *Astrophysics Journal* **493** (1998) 694–707.

[51] O. Adriani et al., "PAMELA Measurements of Cosmic-Ray Protons and Helium Spectra", *Science* **332** (2011) 69–72.

[52] Particle Data Group Collaboration, "Review of Particle Physics", *Phys. Rev. D* **86** (2012).

[53] A. Morselli and I.V. Moskalenko, " Status of indirect searches in the PAMELA and Fermi era", in *Identification of Dark Matter 2008*. 2008. arXiv:0811.3526.

[54] T. K. Gaisser, "The Cosmic-ray Spectrum: from the knee to the ankle", *Journal of Physics: Conference Series* **47** (2006), no. 1, 15.

[55] H.S. Ahn et al., "The Cosmic Ray Energetics and Mass (CREAM) instrument", *Nucl. Instrum. and Methods A* **579** (2007) 1034–1053.

[56] P.J. Boyle et al., "The Elemental Composition of high-energy Cosmic Rays: Measurement with TRACER", *Modern Physics Letters A* **23** (2008) 2031.

[57] W.B. Atwood et al. (Fermi/LAT Collaboration), "The Large Area Telescope on the Fermi Gamma-ray Space Telescope Mission", *Astrophys. Journal* **697** (2009) 1071–1102.

[58] A. Morselli and P. Picozza for the PAMELA Collaboration, "The PAMELA apparatus for the search of antimatter in cosmic rays", *Topics in Cosmic-Ray Physics* **230** (1999) 37–47.

[59] Andreas Haungs, "From the Knee to the Ankle:From Galactic to Extragalactic Origin of Cosmic Rays?". World Scientific Publishing Co., 2011.

[60] J. Abraham et al., "Properties and Performances of the prototype instrument for the Pierre Auger Observatory", *Nuclear Instruments and Methods in Physics Research A* **523** (2004) 50–95.

[61] W.D. Apel et al., "The KASKADE-Grande experiment", *Nucl. Instrum. and Methods in Physics Research A* **620** (2010) 201–216.

[62] J.H. Oort, "The force exerted by the stellar system in the direction perpendicular to the galactic plane and some related problems", *Bulletin of the Astronomical Institutes of the Netherlands* **6** (1932) 249.

[63] V. Trimble, "Existence and nature of Dark Matter in the universe", *Annual Review of Astronomy and Astrophysics* **25** (1987) 425–472.

[64] H.W. Babcock, "The Rotation of the Andromenda Nebula", *Lick observatory bulletin* **498** (1939).

[65] A. Vikhlinin et al., "Chandra sample of nearby relaxed galaxy clusters: mass, gas fraction, and temperature-mass relation", *Astrophysics Journal* **640** (2005), no. 2, 691.

[66] G.G. Byrd, M. Valtonen, A.D. Chernin, and V.P. Teerikorpi, "Paths to Dark Energy". de Gruyter, 2012.

[67] V.C. Rubin, W.K. Ford Jr., and N. Thonnard, "Rotational properties of 21 SC galaxies with a large range of luminosities and radii, from NGC 4605 /R = 4kpc/ to UGC 2885 /R = 122 kpc", *Astrophysical Journal* **238** (1980) 471 – 487. Part 1.

[68] J.S. Mulchaey, "X-Ray Properties of Groups of Ç´alaxies", *Annual Review of Astronomy and Astrophysics* **38** (2000) 289–335.

[69] W. Hu and S. Dodelson, "Cosmic Microwave Background Anisotropies", *Annu. Rev. Astron. Astrophys.* **40** (2002) 171–216.

[70] W. Hu, "The Cosmic Microwave Background: From Quantum Fluctuations to the Present Universe", ch. Lecture Notes on CMB Theory: From Nucleosynthesis to Recombination. Cambridge University Press, 2009. arXiv:0802.3688.

[71] G.R. Blumenthal, S.M. Faber, J.R. Primack, and M.J. Rees, "Formation of galaxies and large-scale structure with cold dark matter", *Nature* **311** (1984) 517–525.

[72] Planck Collaboration, "Planck 2013 results. XVI. Cosmological parameters", *submitted to Astronomy and Astrophysics* (2013). arXiv:1303.5076.

[73] Matts Roos, "Introduction to cosmology". John Wiley and Sons, 2003. ISBN 0470849096.

Bibliography

[74] F.W. Dyson, A.S. Eddington, and C Davidson, "A Determination of the Deflection of Light by the Sun's Gravitational Field, from Observations Made at the Total Eclipse of May 29, 1919 ", *Philosophical Transactions of the Royal Society A* **220 A** (1920) 291–333.

[75] A. Refregier, "Weak Gravitational Lensing by Large-Scale Structure", *Annu. Rev. Astron. Astrophys.* **41** (2003) 645–668.

[76] P. Tisserand et al., "Limits on the Macho Content of the Galactic Halo from EROS-2 Survey of the Magellanic Clouds", *Astron. Astrophys.* **469** (2006), no. 2, 387–404.

[77] K. Freese, B.D. Field, and D.S. Graff, "Sources and Detection of Dark Matter and Dark Energy in the Universe", ch. Death of Stellar Baryonic Dark Matter, pp. 159–167. Springer Berlin Heidelberg, 2001.

[78] F. Aharonian et al., "The TeV Eenrgy Spectrum of Markarian 501 Measured with the Stereoscopic Telescope System of HEGRA during 1998 and 1999", *Astrophys. Journal* **546** (2001) 898–902.

[79] T.A. Smecker and R.F.G. Wyse, "Type IA supernovae - Constrains on baryonic dark matter", *Astrophys. Journal* **372** (1991) 448–454.

[80] R. Davis, "Nobel Prize Lecture", *Rev. Mod. Phys* **75** (2003) 985–994.

[81] S. Weinberg, "Gravitation and cosmology". Wiley, 1972.

[82] J.R. Primack and A.K. Gross, "Hot Dark Matter in Cosmology". Springer, 2000.

[83] R.D Peccei and H.R. Quinn, "CP Conservation in the Presence of Pseudoparticles", *Phys Rev. Lett.* **38** (1977) 1440–1443.

[84] C.A. Baker et al., "Improved Experimental Limit on the Electric Dipole Moment of the Neutron", *Physical Review Letters* **97** (2006) 131801.

[85] P. Sikivie, "Experimental Tests of the "Invisible" Axion", *Phys Rev. Lett.* **51** (1983) 1415–1417.

[86] M. Kamionkowski, "WIMP and Axion Dark Matter", *Physics Reports* (1997) 394–411. Published in "Trieste 1997, High Energy physics and cosmology".

[87] G. Jungman, M. Kamionkowski, and K. Griest, "Supersymmetric Dark Matter", *Physics Reports* **267** (1995) 195–373.

[88] E. Witten, "Mass hierarchies in supersymmetric theories", *Physics Letters B* **105** (1981), no. 4, 267–271.

[89] U. Amaldi, W. de Boer, and H. Fürstenau, "Comparison of grand unified theories with electroweak and strong coupling constants measured at LEP", *Physics Letters B* **260** (1991), no. 3,4, 447–455.

[90] D.I. Kazakov, "Supersymmetry in particle physics: the renormalization group viewpoint ", *Physics Reports* **344** (2001) 309–353.

[91] H. Nishino et al. (Super-Kamiokande Collaboration), "Search for Proton Decay via p->$e^+ + \pi^0$ and p->$\mu^+ + \pi^0$ in a Large Water Cherenkov Detector", *Physical Review Letters* **102** (2009) 141801.

[92] G. Bertone, D. Hooper, and S.Silk, "Dark Matter: Evidence, Candidates and Constrains", *Phys. Rept.* **405** (2004) 279–390.

[93] R.J. Gaitskell, "Direct Detection of Dark Matter", *Annu. Rev. Nucl. Part. Sci.* **54** (2004) 315–359.

[94] G. Bertone and D. Merritt, "Dark Matter Dynamics and Indirect Detection", *Modern Physics Letters A* **20** (2005) 1021–1036.

[95] A. Broniatowski et al., "A new high-background-rejection dark matter Ge cryogenic detector", *Physics Letters B* **681** (2009) 305–309.

[96] Xenon collaboration, "The XENON100 Dark Matter Experiment", *Astroparticle Physics* **35** (2012) 573–590.

[97] "The CRESST dark matter search", *Astroparticle Physics* **12** (1999), no. 1-2, 107 – 114.

[98] CDMS and EDELWEISS collaborations, "Combined Limits on WIMPs from the CDMS and EDELWEISS Experiments", *Physical Review D* **84** (2011) 011102.

[99] "The Large Hadron Collider Conceptual Design", (1995).

[100] G. Kane and S. Watson, "Dark Matter and LHC: What is the Connection?", *Modern Physics Letters A* **23** (2008) 2103.

[101] C. Beskidt, W. de Boer, D.I. Kazakov, and F. Ratnikov, "Constrains on Supersymmetry from LHC data on SUSY searches and Higgs bosons combined with cosmology and direct dark matter searches", *The European Physical Journal C* **72** (2012), no. 2166,.

[102] J. Silk, K. A. Olive, and M. Srednicki, "The Photino, the Sun and High Energy Neutrinos", *Physics Review Letters* **55** (1985) 257–259.

[103] IceCube collaboration, "Search for Dark Matter Annihilations in the Sun with the 79-string IceCube Detector", *Physical Review Letters* **110** (2013) 131302.

Bibliography

[104] J.A. Aguilar et al., "ANTARES: the first undersea neutrino telescope", *Nuclear Inst. and Methods in Physics Research A* **656** (2011) 11–38.

[105] S.P. Martin, "A Supersymmetry Primer". arXiv:hep-ph/9709356v6, 2011.

[106] A. Geringer-Sameth and S.M. Koushiappas, "Dark Matter line search using a joint analysis of dwarf galaxies with the Fermi Gamma-ray Space Telescope", *Physical Review D* **82** (2012) 021302.

[107] D. Hooper, P. Blasi, and P.D. Serpico, "Pulsars as the source of high energy cosmic ray positrons", *Journal of Cosmology and Astrophysical Physics* **2009** (2009). January.

[108] S. Profumo, "Fundamental Physics from the Sky: Cosmic Rays, Gamma Rays and the Hunt for Dark Matter", *arXiv:1209.5702* (2012). proceedings of the 18th International Symposium on Particles, Strings ans Cosmology.

[109] I. Cernuda, "Cosmic-ray electron anisotropies as a tool to discriminate between exotic and astrophysical sources", *Astroparticle Physics* **34** (2010) 59–69.

[110] A.D. Sakharov, "Violation of CP variance, C asymmetry, and baryon asymmetry of the universe", *Soviet Physics Uspekhi* **34** (1991) 392.

[111] C.S. Wu et al., "Experimental Test of Parity Conservation in Beta Decay", *Physical Review* **105** (1957) 1413–1415.

[112] J.H. Christenson, J.W. Cronin, V.L. Fitch, and R. Turlay, "Evidence for the 2π Decay of the K_2^0 Meson", *Physical Review Letters* **13** (1964) 138–140.

[113] BaBar Collaboration, "Observation of CP violation in the B^0 meson system ", *Physical Review Letters* **87** (2001) 091801.

[114] A. Abashian et al., "Measurement of the CP Violation Parameter $\sin^2\phi$ in B_d^0 Meson Decays", *Physical Review Letters* **86** (2001) 2509–2514.

[115] M. Kobayashi and T. Maskawa, "CP-Violation in the Renormalizable Theory of Weak interaction", *Progress of Theoretical Physics* **49** (1973) 652–657.

[116] C. Jarlskog, "Commutator of the Quark Mass Matrices in the Standard Electroweak Model and a Measure of Maximal CP Nonconservation", *Physical Review Letters* **55** (1985) 1039–1042.

[117] M.E. Shaposhnikov, "Possible appearance of the asymmetry of the universe in an electroweak theory ", *Journal of Exp. and Theo. Physics Letters* **44** (1986) 465.

[118] H. Georgi and S. L. Glashow, "Unity of All Elementary-Particle Forces", *Physical Review Letters* **32** (1974), no. 8, 438–441.

[119] J.C. Pati and A. Salam, "Lepton number as the fourth "color"", *Physical Review D* **10** (1974), no. 1, 275–289.

[120] G. t'Hooft, "Symmetry breaking through Bell-Jackiw Anomalies", *Physical Review Letters* **37** (1976) 8–11.

[121] R. Battiston and A. Oliva, "AMS-02 webpage".

[122] Th. Siedenburg et al., "Performance of the AMS-02 Transition Radiation Detector", *arXiv:astro-ph/0608641* **558** (2006).

[123] A. Sabellek, "The Space Qualified Data Acquisition for the Transition Radiation Detector of the AMS-02 Experiment on the International Space Station". PhD thesis, Universität Karlsruhe, TH, 2009. IEKP-KA/2008-26.

[124] K. Gassmann, "Entwicklung und Test der raumfahrtqualifizierten Datenakquisition für den Übergangsstrahlungsdetektor des AMS-02 Experiments auf der Internationalen Raumstation (german)", 2007. Diploma thesis.

[125] M. Scheulen, "DSP Software Development for TRD electronics of the AMS-02 Detector", 2007. Diploma thesis.

[126] M. Heil, "Tests mit dem Übergangsstrahlungsdetektor des AMS-02 Projekts". 2010.

[127] V. Bindi et al., "The time of flight detector of the AMS-02 experiment on the international space station", *Nuclear Instruments and Methods in Physics Research Section A: Accelerators, Spectrometers, Detectors and Associated Equipment* (2012).

[128] Ph. von Doetinchem et al., "The Anticoincidence Counter System of AMS-02", (2009).

[129] D. D'Urso for the AMS Collaboration, "The AMS-02 Silicon Tracker: Status and Performances", *World Scientific* (2012). proceedings of the 13th ICATPP conference.

[130] Z. Zhang et al., "Development of a Thermal Control System with Mechanically Pumped CO_2 Two-Phase Loops for the AMS-02 Tracker on the ISS", *arXiv:1302.4294* (2013).

[131] R. Pereira et al., "The RICH detector of the AMS-02 experiment: status and physics prospects", *arXiv:0801.3250* (2008). contribution to the ICATPP 2007.

[132] C. Grupen and B. Shwartz, "Particle Detectors". Cambridge University Press, 2008.

[133] M. Incagli et al., "The AMS-02 lead-scintillating fibres Electromagnetic Calorimeter", *Nucl. Inst. and Methods in Physics Research, A* **714** (2013) 147–154.

Bibliography

[134] J.A. Van Allen and L.A. Frank, "The geomagnetically trapped corpuscular radiation", *Journal of Geophysical Research* **64** (1959) 1683–1689.

[135] T. Kirn, B. Beischer, C. Chung, T. Siedenburg, M. Heil, K. Andeen, and F. Spada, "TRD / ACC / TAS Slow Control and Data Monitoring". 2013.

[136] A.A Komar, "Classical and Quantum Effects in Electro-dynamics". Nova Publisher, 1988.

[137] J.D. Jackson, "Klassische Elektrodynamik". de Gruyter, 2002.

[138] T. Kirn for the AMS-02 TRD collaboration, "The AMS-02 TRD on the international space station", *Nucl. Instr. Meth. Phys. Research* **706** (2013) 43–47. Section A: Accelerators, Spectrometers, Detectors ans Associated Equipment.

[139] Ulrik Egede, "The search for a standard model Higgs at the LHC and electron identification using transition radiation in the ATLAS tracker". PhD thesis, Lund University, 1998.

[140] Dan Green, "At the Leading Edge: The Atlas and CMS LHC Experiments". World Scientific, 2010.

[141] David Griffith, "Introduction to Elementary Particles". Wiley-VCH, 2008. ISBN 3527406018.

[142] publisher = Springer-Verlag Berlin Heidelberg Léna, P. and Rouan, D. and Mugnier, L. and Lebrun, F., year = 2012, "Observational astrophysics".

[143] A. Sabellek, "Data Processing in UDR2". AMS internal note, 2008.

[144] A. Kounine and V. Koutsenko, "Flight Software for XDR and JINx nodes in AMS-02". AMS internal note, 2009.

[145] C. Chung and Z. Weng, "AMS-02 TWiki".

[146] L. Landau, "On the Energy Loss of Fast Particles by Ionisation", *Journal of Physics (USSR)* **8** (1944) 201–205.

[147] T. Siedenburg, "ISS Orbit Parameters". AMS Meeting presentation, 2002.

[148] AMS-02 Project Office Timothy J. Urban, Jacobs Technology Inc., 2013. private communication.

[149] V. Blobel, "Statistical Problems in Particle Physics, Astrophysics ans Cosmology". Imperial College Press, 2006.

[150] S. Zeissler, "Positronen Identifizierung mit dem AMS-02 Detektor auf der Internationalen Raumstation". 2013.

[151] W.T.Eadie, D. Drijard, F.E. James, M. Roos, and B. Sadoulet, "Statistical methods in experimental physics". North-Holland, 1971.

[152] Thomas Ferbel, "Experimental Techniques in High Energy Physics". Addison-Wesley Publishing Company, 1987.

[153] A. Hoecker, P. Speckmayer, J. Stelzer, J. Therhaag, E. von Toerne, and H. Voss, "TMVA 4: Toolkit for Multivariate Data Analysis with ROOT". arXiv:physics/0703039, 2009.

[154] AMS Collaboration, "First Result from the Alpha Magnetic Spectrometer on the International Space Station: Precision Measurement of the Positron Fraction in Primary Cosmic Rays of 0.5 - 350 GeV", *Phys. Rev. Lett.* **110** (2013).

[155] D.F. Smart and M.A. Shea, "A review of geomagnetic cutoff rigidities for earth-orbiting spacecraft", *Advances in Space Research* **36** (2005) 2012–2020.

[156] S. Agostinelli et al., "Geant4 - A Simulation Toolkit", *Nuclear Instruments and Methods A* **506** (2003) 250–303.

[157] R. Barlow, "Systematic Errors: facts and fictions", *arXiv:hep-ex/0207026* (2002).

[158] M. Incagli, "Effects of Dilution in the determination of the positron fraction". AMS internal note, 2012.

[159] S. Kunz and I. Gebauer, 2013. private communication.

List of Figures

List of Tables

Appendix

A. Appendix

A.1. List of abbreviations

CR	cosmic rays
AMS(-02)	Alpha Magnetic Sprectrometer
ISS	International Space Station
TRD	Transition Radiation Detector
ECAL	Electromagnetic Calorimeter
MC	Monte Carlo
CMB	cosmic microwave background
SN	supernova
DM	Dark Matter
MACHO	massive astrophysical compact halo object
QCD	quantum chromodynamics
WIMP	weak interacting massive particle
SUSY	Supersymmetry
GUT	grand unified theory
LHC	Large Hadron Collider
STS	Space Transportation System
CERN	European Organization for Nuclear Research
ESTEC	european space research and technology center
NASA	National Aeronautics and Space Administration
SPS	Super-Proton-Synchrotron
KSC	Kennedy Space Center
ToF	Time-of-Flight detector
ACC	Anti Coincidence Counter
RICH	Ring Imaging Cherenkov detector
TDC	time to digital converter
TTCS	Tracker Thermal Control System
MDR	maximum detectable rigidity
xDR	data reduction board
JINF-x	interface board of subdetector electronics
JINJ	interface board of higher level electronics
JMDC	main data computer
POCC	Payload Operation Control Center
DSP	digital signal proccessor

UPD	power distribution box of the TRD
UDR2	data reduction board of the TRD
UHVG	high voltage generator board of the TRD
UPSFE	power supply for front end electronics board of the TRD
JINF-U	interface board between TRD and higher level electronics
UTE	tube end board of the TRD
UFE	front end board of the TRD
ADC	analog to digital converter (counts)
MPV	most probabale value
BDT	boosted decision tree
PDF	probability density function
E/R	energy to rigidity ratio

A.2. TRD module numbering scheme

The numbering of the TRD modules used in chapter 5 is presented in figure A.1. For simplification all modules are displayed in the projection of their measurering direction. The lower and upper four layers are oriented parallel to the x-axis of the AMS coordinate system. Therefore they measure the particle passage in the y-direction. The twelve middle layers are oriented with the y-axis, hence they measure the x-coordinate of the particle track.
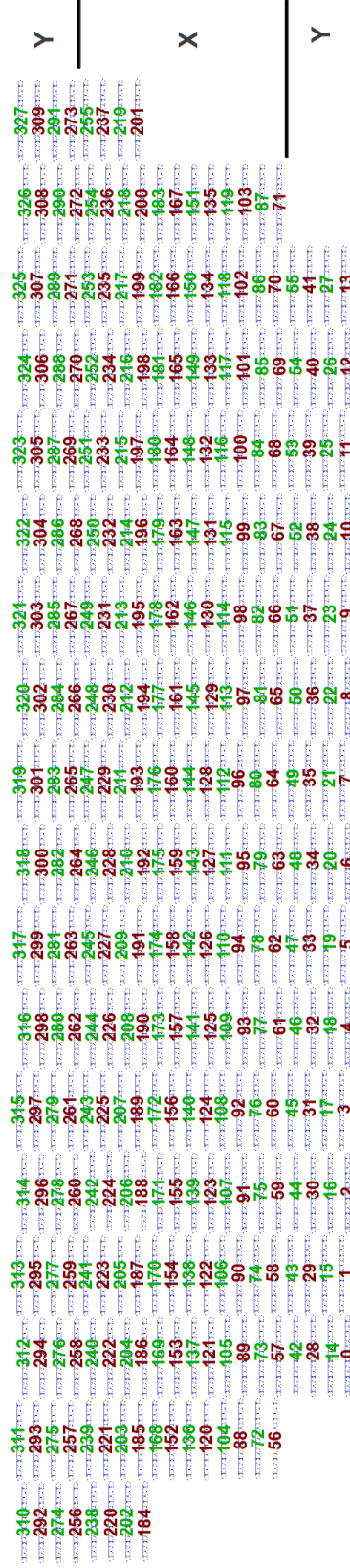
Figure A.1.: **TRD module numbering scheme** All modules are depicted orthogonally with their measuring direction. The four top and four bottom layers, which measure the y-direction, are therefore illustrated rotated by 90° to show the module profile.

Acknowledgements

Hereby I declare, that the presented PhD thesis:

**Measurement of the positron fraction in cosmic
rays from 0.5 -350 GeV with the AMS-02 detector
on the International Space Station**

has been produced independently under the solely use of the denoted auxiliaries.

Melanie Heil